Using CFD to design riprap bed protections downstream of underflow weirs

Weir design of the future

Master Thesis

L.P. van Koelen

Delft University of Technology

TU Delft

Royal HaskoningDHV
Enhancing Society Together

Deltares
Enabling Delta Life

Using CFD to design riprap bed protections downstream of underflow weirs

Weir design of the future

by

L.P. van Koelen

in partial fulfilment of the requirements for the degree of

Master of Science
in Civil Engineering

at the Delft University of Technology,
to be defended publicly on Friday June 10, 2022 at 15:00h.

Student number:	4459350	
Chair of committee:	dr. ir. D. Wüthrich	TU Delft, Hydraulic Structures
Second committee member:	dr. ir. O.J. Colomés Gené	TU Delft, Offshore Engineering
Company & daily supervisor:	ir. drs. S.J.M. Boersen	Royal HaskoningDHV
Company supervisor:	dr. ir. T. O'Mahoney	Deltares
Institution:	Delft University of Technology	
Place:	Faculty of Civil Engineering	
Specialisation:	Hydraulic Engineering	
Project Duration:	9, 2021 - 6, 2022	

Cover Image: Rijkswaterstaat, 100 jaar 7 zussen op de Maas

TU Delft

Royal HaskoningDHV
Enhancing Society Together

Deltares
Enabling Delta Life

Preface

Before you lies my thesis report, which marks the completion of my master's degree in Hydraulic Engineering at the faculty of Civil Engineering and Geosciences at the Delft University of Technology. Throughout my bachelor I gained interest in hydraulic engineering and this interest is further developed during my master and while working on this thesis. On beforehand, numerical modelling was not my main interest but after this thesis, this has changed. For me, numerical modelling of hydraulics is the future of hydraulic engineering and I am glad that I could make a contribution to this.

I would like to express my gratitude for the contributions of my committee to my thesis. Thank you Stef Boersen, for always being present at the office of Royal HaskoningDHV and your knowledge on OpenFOAM and efficiency. It was beneficial to be in close contact throughout the thesis. Thank you Tom O'Mahoney for the in depth knowledge on CFD modelling of flow and the provided dataset. Thank you Davide Wüthrich and Oriol Colomés Gené for the sharp remarks and guidance with the TU Delft perspective.

I am glad that I got the opportunity to work with OpenFOAM whilst being at the office of Royal HaskoningDHV. Their expertise in OpenFOAM is very high and the tools they provided gave me a rapid start. This allowed me to further develop my experience in numerical modelling.

A final word of appreciation goes to my (TU Delft) friends, family and girlfriend. Koen, thank you for providing me feedback on CFD modelling. I am glad that finally our interests in engineering could meet. Soesja, thank you for being there every time I needed you and having the patience to listen and think along. And lastly, thank you Pa en Ma for providing me the opportunity to obtain both the bachelor's and master's degree and supporting me all the way.

L.P. van Koelen
Delft, June 2022

Abstract

Weirs are constructed inside rivers to manage the water level. On the one hand they need to be designed sufficiently strong to prevent failure or destruction, while on the other hand they need to be economically feasible. If a structure is designed too strong, unnecessary costs are made and the structure becomes too expensive.

One of the potential failure mechanisms for weirs is erosion of the soil downstream of the weir. Bed protections consisting of rock and concrete are placed to prevent this erosion. Numerical modelling can give additional insight in the design of such a bed protection. This thesis aims to improve the design of bed protections downstream of underflow weirs through numerical modelling. This is done through two research objectives, being 1) proposing a numerical modelling strategy to create a design method for riprap bed protections downstream of underflow weirs, and 2) preserving a small computation time compared to full scale 3D models, as this is ideal for a future application in engineering.

A new approach is formulated by using the stability parameter of Steenstra (2014), ψ_{RS}, as basis. This parameter is based on multiple flow situations, except the underflow gate. For this reason the underflow gate is investigated in the current research. The output of the created OpenFOAM models can be applied to this parameter, leading to ψ-curves that can be compared with measured damage.

The first research objective is obtained by the application of three different turbulence mixing length approaches, of which two approaches created interesting results. The first approach is the Bakhmetev approach, leading to a conservative design outcome with a gradual decreasing stability pattern. The second is the Shear Stress Relation (SSR), leading to a promising result with better defined instability regions that compare with measured bed damage. From the desire to work conservatively, the results reveal that in the design phase of a bed protection downstream of a weir, the application of the Bakhmetev approach for the mixing length is recommended over the SSR approach.

Extended physical testing containing three aspects is needed to strengthen the promising findings of the SSR. These aspects are 1) a damage stone count including a sieve distribution, 2) a setup with varying gate heights and stone dimensions, and 3) varying water levels and discharges per different gate height and stone size. In addition a preliminary 2D numerical model study is advised, which allows to investigate the areas of interest for PIV flow measurements.

The second research objective is achieved by the application of a 2D RANS model and the simplification of the water level through a rigid lid. This simplification still leads to workable results, with computation time that are in the range of two to eight hours, operating on ten cores in one computer. This makes the approach attractive for engineering applications and for future applications in renovation tasks for weirs in the Meuse.

Contents

Nomenclature

Abbreviations

Abbreviation	Definition
CFD	Computational Fluid Dynamics
CMA	Closure model approach
DNS	Direct Numerical Simulation
IDDES	Improved Delayed Detached Eddy Simulation
LES	Large Eddy Simulation
OpenFOAM	Open Source Field Operation and Manipulation
RANS	Reynolds Averaged Navier Stokes
RSM	Reynolds Stress Model
SSR	Shear stress relation
SST	Shear stress transport
TKE	Turbulent Kinetic Energy
URANS	Unsteady-RANS
VoF	Volume of Fluid

Symbols

Symbol	Definition	Unit
B	Integration constant	[-]
b_0	Gate opening	$[m]$
C_b	Bulk coefficient	[-]
$CD_{k\omega}$	Closure coefficient	[-]
C_m	mass coefficient	[-]
C_μ	Turbulence model constant	[-]
d	Reference height	$[m]$
D	Head difference	$[m]$
d_{n50}	Nominal stone diameter	$[m]$
d_{design}	Design stone diameter	$[m]$
d_p	Prototype stone diameter	$[m]$
d_x	Cell width	$[m]$
F_1	Closure coefficient	[-]
g	Gravitational acceleration	$[m/s^2]$
G	Closure coefficient	[-]
h	Water depth	$[m]$
H	Location in the water column	$[m]$
h_a	Location of acceleration term	$[m]$
I	Turbulence intensity	[-]
k	Turbulent kinetic energy	$[m^2/s^2]$
k_s	Nikuradse roughness	$[m]$
k_s^+	Dimensionless equivalent roughness	[-]
l	Mixing length reference scale	$[m]$
l_{CMA}	Mixing length computed with the CMA	$[m]$
L_ϵ	Dissipation length	$[m]$
L_H	Horizontal eddy length scale	$[m]$
L_m	Bakhmetev mixing length	$[m]$

Symbol	Definition	Unit
L_{mixing}	Non-specified mixing length	$[m]$
l_{SSR}	Mixing length computed with the SSR	$[m]$
N_x	Number of cells in the horizontal direction	[-]
N_z	Number of cells in the vertical direction	[-]
p	Pressure	$[kg/ms^2]$
Q	Discharge	$[m^3/s]$
R	Reynolds stress	$[m^2/s^2]$
R_c	Correlation factor	[-]
S	Stress tensor	$[m^2/s^2]$
$\boldsymbol{u}$	velocity vector consisting of (u, v, w)	$[m/s]$
u	Streamwise velocity	$[m/s]$
$\overline{u}$	Time-averaged streamwise velocity	$[m/s]$
u^+	Dimensionless streamwise velocity	[-]
$\boldsymbol{u'}$	Velocity fluctuation vector of (u',v',w')	$[m/s]$
u'	Fluctuating streamwise velocity vector	$[m/s]$
$\boldsymbol{u'}_{RMS}$	Root mean square of (u',v',w')	$[m/s]$
u_τ	shear velocity	$[m/s]$
v	Transverse velocity	$[m/s]$
v'	Fluctuating transverse velocity	$[m/s]$
w	Vertical velocity	$[m/s]$
w'	Fluctuating vertical velocity	$[m/s]$
x	Streamwise location	$[m]$
y	Transverse location	$[m]$
z	Vertical location	$[m]$
z_c	Height of first cell center	$[m]$
z_{max}	Location in water column with largest drag force	$[m]$
z^+	Dimensionless vertical location	[-]
z_0^+	Equivalent roughness height	[-]
α	Amplification factor	[-]
β	Angle of river bed	$[^o]$
$\beta_{k\omega}$	Model coefficient	[-]
β^*	Model coefficient	[-]
γ	Ratio of z and h	[-]
$\gamma_{k\omega}$	Model coefficient	[-]
γ_s	Safety factor	[-]
Δ	Relative density	[-]
κ	von Karmann constant	[-]
μ	Dynamic viscosity	$[m^2/s]$
ν	Kinematic viscosity	$[m^2/s]$
ν_t	Turbulent viscosity	$[m^2/s]$
ρ	Density	$[kg/m^3]$
σ	Standard deviation	[-]
τ_b	Wall shear stress	$[N/m^2]$
τ_v	Viscous shear stress	$[N/m^2]$
ψ_{cr}	Critical stability threshold	[-]
ψ_{Lm}	Hofland stability parameter	[-]
ψ_{RS}	Steenstra stability parameter	[-]
$\psi_{RS,c}$	Critical Steenstra stability parameter	[-]
$\psi_{RS,p}$	Prototype Steenstra stability parameter	[-]
$\psi_{u-k-crit}$	Jongeling stability parameter	[-]
$\psi_{u-\sigma[u]}$	Hoan stability parameter	[-]
ϕ_E	Entrainment rate	[-]
ω	Specific dissipation rate	$[1/s]$

1 Introduction

Chapter 1 covers the general description of the research. With an introduction to the topic, the relevance and observed problem are provided. The research question is formulated and supported by the research approach. In the end the structure of the report itself is provided.

1.1. Introduction to research

A weir is a river structure that is used for maintaining water levels in a river and regulating the flood safety. An example of a weir is provided in Figure 1.1, in which flow is from northeast to southwest. Through this structure, the flow velocity increases temporarily. A turbulent motion downstream of the weir leads to energy loss, thus a velocity decrease, leading to a velocity which returns to the normal river velocity. This increased velocity and turbulent motion close to the weir leads to erosion of soil particles downstream of the structure, as seen in the scale model of weir Hagestein (Figure 1.2). This eventually leads to structure failure.

A prevention for erosion is a riprap bed protection downstream of the weir. A main design parameter for riprap bed protections is stone stability. If a threshold of motion is exceeded, a stone starts to move and the bed protection erodes. A good design contains limited to no stone movement. Stone movement should be prevented by designing the bed protection correctly.

Figure 1.1: Top view of weir Hagestein (Rijkswaterstaat, 2020)

Figure 1.2: Bed damage of scale model of weir Hagestein (Waterloopkunding Laboratorium, 1955)

A common approach in the design phase of hydraulic structures is physical model tests. In these tests, the soon to be build structure is scaled to model size and corresponding flow situations are created in a basin or flume. This will reveal if the design can withstand the design conditions. The advantage of these tests is that tangible output is created and full 3D flow effects can be taken into account. A disadvantage is that geometry and setup are not easily modified and local output at all locations in a domain is not easily measured.

An upcoming competitor for physical testing is numerical modelling. Through computational fluid dynamics (CFD) a numerical model of the future structure can be made. Accuracy and needed computation time of a CFD model can vary for different application and the output can be measured throughout the whole domain. Next to this, model variations are easily applied. For this thesis the CFD software OpenFOAM is used, as this is commonly used and transparent. An additional benefit is that the software is open-source and for that reason free of charge. This makes the software package attractive for companies.

The conversion of this detailed numerical output to design parameters in river flow situations has a research interest that started multiple years ago. Several researches on this topic are introduced in Chapter 2, including their developed stability parameters ψ.

This thesis focuses on the conversion of CFD output of flow through an underflow weir. Flow through this structure, as well as damage, has been measured in previous research. Despite that, it was not included in the created stability parameters. This thesis contributes to the further application of CFD modelling in the design phase of river structures.

1.2. Problem definition

Over the years, extensive research has been conducted on the stability of bed protections and the application of numerical output in the assessment of the stability. Jongeling et al. (2003) started the series of research by performing physical tests in a flume with multiple flow situations. Examples are flow over a flat bed, over a sill and past an underflow gate. These tests formed the basis for additional research.

Hofland (2005) used the measurements to incorporate a turbulence mixing length, Hoan (2008) contributed with additional measurements for gradually expanding open-channel flow and a new stability parameter. Steenstra (2014) combined four data sets, including Jongeling et al. (2003) and Hoan (2008) into a new stability relation, while adding the acceleration term as well. The new parameter of Steenstra (2014) was tested by Stevens (2018) with a 3D eddy resolving simulation technique. Lastly, Nikolaidou (2019) applied an IDDES approach for a detailed analysis for the long sill, by focusing on the development of a hydrodynamic numerical tool. A note is that a computation time of 30 days for three minutes of output time was required. Further elaboration on this is found in Chapter 2.

After Steenstra (2014) the focus shifted more on precise modelling, making Steenstra (2014) the last research that introduced a well calibrated stability formula, while as well verifying it with a 2D RANS model. Despite being tested on many flow situations, the underflow gate has been omitted. The reason is due to its relatively large complexity of the flow and the problem that it is hard to perform stable, accurate calculations. This was the case for Jongeling et al. (2003) too and shows the challenges of stability computations downstream of underflow weirs, which is being coped in this thesis.

As there will be a replacement of the weirs in the Meuse (Appendix A), gaining additional information on the application of numerical output downstream of weirs is essential. Multiple weir shapes can be made and for this thesis the focus lies on underflow weirs with a submerged hydraulic jump downstream of the gate. For this structure both Jongeling et al. (2003) and Deltares (2020) worked with underflow gates, providing reference cases for the created CFD models.

The reference cases of Jongeling et al. (2003) are case 6 and 7. Especially the stone damage curves provide reference for stability calculations with numerical output. Deltares (2020) provides detailed PIV measurements of the underflow gate for three gate heights. These measurements are made with a smooth bed and no bed damage was measured. The combination of both measurements contributes in solving the underflow gate problem.

In order to have an application that will be of use for future design purposes, a practical approach is developed. Computations with relatively short calculation times contribute to this. A short calculation

time can only be obtained by simplification of the actual situation. This research approach differs from the latest researches on stone stability.

1.3. Objective and research questions

The objective for this thesis consists of two main items:

1. Proposing a numerical modelling strategy to create a design method for riprap bed protections downstream of underflow weirs.
2. Preserving a small computation time compared to full scale 3D models.

The objective contributes to the further understanding of practical numerical modelling and the application of numerical output in the design process. Based on the future design task for the renovation of the weirs and the goal of practically applying numerical output, the objective can be translated into the following research question:

How can CFD modelling in OpenFOAM be applied to determine stone stability for a riprap bed protection downstream of submerged underflow weirs?

The following sub-research questions support the main question and will be answered throughout the report as well:

1. What are the current methods and insights on the assessment of bed protection through numerical modelling?
2. What is the effect of different mixing length approaches on the stability calculations outcome?
3. What is the influence of the drag term and advective acceleration term in the stability parameter of Steenstra (2014) on the computed stability?

1.4. Approach and methods

For this thesis the Steenstra (2014) equation is used to compute a stability number. The equation is investigated and multiple approaches for the mixing length are tested, based on the original approach with the Bakhmetev distribution, the shear stress relation (SSR) and closure model approach (CMA).

The numerical model applies the RANS method with $k-\omega$ SST turbulence closure. The water surface is modelled as a rigid lid and the model is created in a 2D environment, which significantly reduces the computation time but also implies simplifications.

Validation of the numerical models is done against data of Deltares (2020), as well as Jongeling et al. (2003). Stability computations are done with the OpenFOAM output for five cases. Case 1 to 3 are based on the physical tests of Deltares (2020) and case 4 and 5 on the ones from Jongeling et al. (2003).

The latter provides stone damage curves, containing information regarding actual occurring damage, while the former provides detailed PIV measurements of smooth bed cases. The combination of both leads to an approach for the application of numerical output for the design phase of bed protections downstream of underflow weirs. A comparison between stone damage curves and stability curves, called ψ-curves, relates the damage to the computed damage.

Figure 1.3 provides a simplified overview of the thesis approach, where the link between the stability parameter of Steenstra (2014), ψ_{RS}, and the damage curves of Jongeling et al. (2003) can be seen. In Chapter 5, Figure 5.1 the detailed workflow can be found, which is advised to read after Chapter 2 to Chapter 4.

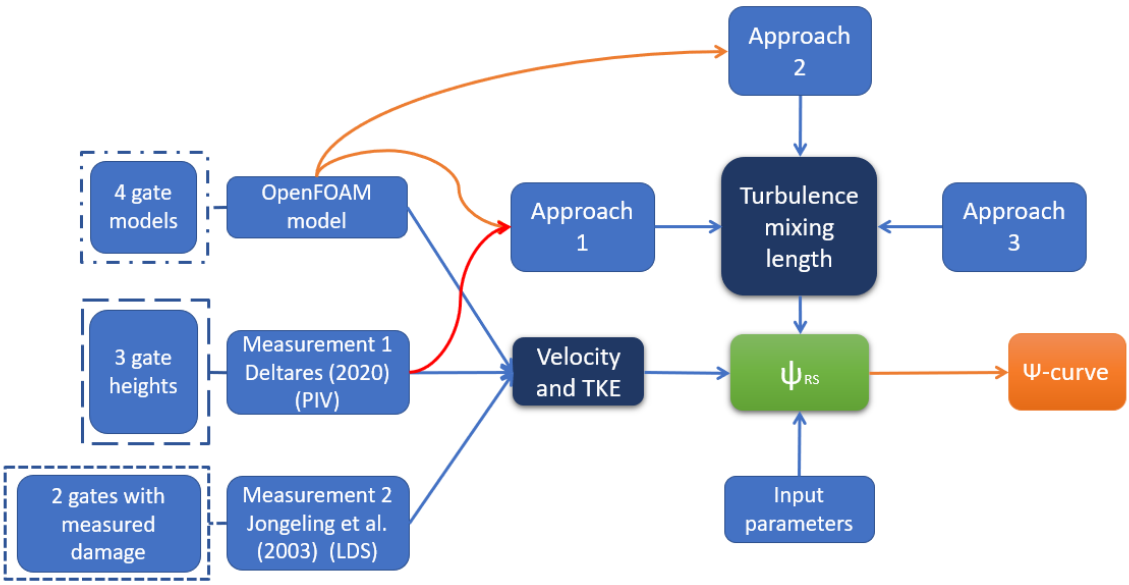

Figure 1.3: Overview of the simplified approach for this thesis

The applied coordinate system for this thesis is visualised below.

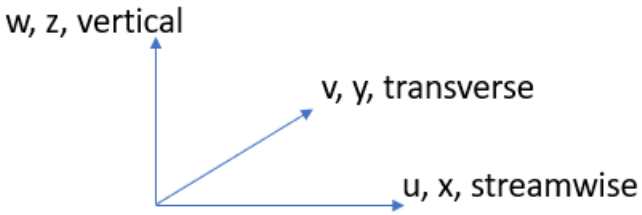

Figure 1.4: The coordinate system applied in this thesis

1.5. Thesis outline

The structure of this report is as follows:

Chapter 1 provides the introduction to the thesis, providing the relevance and problem of this thesis. Additionally it introduces the research objective and questions, as well as the methodology.

Chapter 2 gives background information on the topic, numerical modelling, stone stability and the turbulence length scale.

Chapter 3 provides the introduction to the underflow gate and model. The validation against the model of Deltares (2020) follows, as well as validation of a rough bed model, based on Jongeling et al. (2003).

Chapter 4 introduces the three mixing length approaches and compares the approaches through a stability parameter ψ_{RS} computation.

Chapter 5 works out the main result of this thesis, in which rough wall OpenFOAM models are transformed towards ψ-curves. In this chapter the link between numerically determined instability and physically measured damage is made.

Chapter 6 discusses the findings through two main discussion points. Next to this it provides additional discussion and the relevance of the results.

Chapter 7 provides the overall conclusion and answer to the main and sub research questions.

2

Literature review

In Chapter 2 a theoretical clarification will be given on important aspects of this thesis. First, Section 2.1 provides background on numerical modelling in hydraulics. Next the concept of stone stability is elaborated in Section 2.2, including the introduction the stability parameter of Steenstra (2014). At last the turbulence length scale is explained in Section 2.3.

2.1. Numerical modelling

An introduction towards numerical modelling of flow is provided. First computational fluid dynamics is elaborated, including the Reynolds Averaged Navier Stokes (RANS) modelling and closure problem. Next, modelling of the free surface as well as near wall modelling is introduced. This leads to a modelling advice for a bed protection.

2.1.1. Computational modelling in hydraulics

Computational modelling is based on numerical calculations, which is a method of approximating mathematical equations with computational processes. These computations are repetitive, which makes computers ideal for the calculations. It allows to solve partial differential equations in time and space. Zijlema (2015) provides a thorough elaboration on numerical schemes and methods and is advised to read for additional information on CFD modelling.

The Navier-Stokes equations are the governing equations for CFD. The basic Navier-Stokes equations are based on the continuity of mass and momentum. This thesis assumes that the flow is incompressible, meaning that the density is constant (Zijlema, 2015). For the equation for the conservation of mass this leads to the continuity equation for incompressible flow, Equation 2.1. The second part of the Navier Stokes equations consist of the conservation of momentum, of which the incompressible version can be found in Equation 2.2.

$$\frac{\partial u}{\partial x} + \frac{\partial v}{\partial y} + \frac{\partial w}{\partial z} = \nabla \cdot \boldsymbol{u} = 0 \tag{2.1}$$

$$\frac{\partial \boldsymbol{u}}{\partial t} + \underbrace{\nabla \cdot (\boldsymbol{u}\boldsymbol{u})}_{\text{convective}} = \underbrace{-\frac{1}{\rho}\nabla p + \nabla \tau_v}_{\text{diffusive}} + \underbrace{g}_{\text{source}} \tag{2.2}$$

In which:

- $\boldsymbol{u}$ is the velocity vector consisting of the velocity in direction (u, v, w), which corresponds to the (x, y, z)-component $[m/s]$
- ρ is the density $[kg/m^3]$
- p is the pressure $[kg/ms^2]$
- τ_v is the viscous shear stress $[m/s^2]$

Equation 2.2 consists of four parts, being:

1. the local acceleration term $\frac{\partial \boldsymbol{u}}{\partial t}$
2. the convective term $\nabla \cdot (\boldsymbol{uu})$
3. the diffusive term, which contains pressure related normal stresses $-\frac{1}{\rho}\nabla p$ and viscous shear stresses $\nabla \tau_v$. The latter can be expressed as $\nu \nabla^2 \boldsymbol{u}$ (Battjes, 2002). Here ν is the kinematic viscosity $[m^2/s^2]$
4. the source term, being external forcing. In this case this is the gravity term g $[m/s^2]$

The Navier-Stokes equations cannot be solved analytically, as the equations consists of non-linear, second-order partial differential equations. Next to this, the Navier-Stokes equations have more unknowns than equations, leading to extra assumptions. This is called the closure problem, which is treated in Section 2.1.2. Computational modelling allows an approximation of the Navier-Stokes equations and helps solving flow problems.

Turbulence models can be used to include the effect of turbulent flow in fluids. Turbulence occurs in almost all flows in nature, as well as in engineering applications. Correctly modelling of turbulence is essential in obtaining correct CFD results. Examples are Reynolds Averaged Navier Stokes (RANS), Large Eddy Simulation (LES) and Direct Numerical Simulation (DNS).

For engineering approaches, the interest lays in mean quantities, forces and flow. For these approaches it is advised to use turbulence models, as it is reliable and cost efficient. The computational costs of a RANS model are much lower in comparrison with LES and DNS. Therefore, RANS is more attractive for this study, in which efficiency and practicality of numerical modelling is a central aspect.

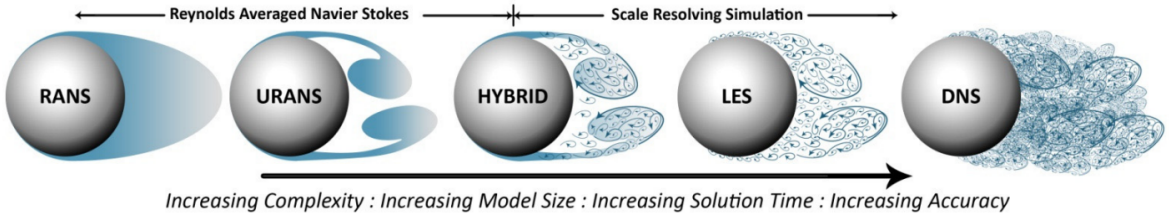

Figure 2.1: Example of turbulence spatial scales resolved by modeling approach (Hart, 2016)

Figure 2.1 shows the difference spatial scales resolved with different methods, varying in complexity, solution time and accuracy.

2.1.2. Reynolds Averaged Navier Stokes equations

Averaged equations of the Navier-Stokes equations can be obtained by an averaging operation. Through this averaging the Reynolds Averaged Navier-Stokes equations are obtained. The equations are comparable to the original Navier-Stokes equations, but in the momentum term (Equation 2.2), an additional term called the Reynolds stress is present. This is an unknown, nonlinear term and needs to be modelled.

Time averaging is used to reduce complex systems of differential equations into simpler forms by eliminating the time variable. For this reason, the flow quantities are split in a time-averaged ($\overline{u}$) and fluctuating ($\boldsymbol{u'}$) component, as described in Equation 2.3. This is called the Reynolds decomposition.

$$\boldsymbol{u} = \overline{\boldsymbol{u}} + \boldsymbol{u'} \tag{2.3}$$

Averaging the governing equations results in the Reynolds Averaged Navier Stokes equation (for incompressible flow):

$$\frac{\partial \overline{\boldsymbol{u}}}{\partial x} + \underbrace{\nabla \cdot (\overline{\boldsymbol{u}}\overline{\boldsymbol{u}})}_{\text{convective}} + \underbrace{\nabla \cdot (\overline{\boldsymbol{u'}\boldsymbol{u'}})}_{\text{Reynolds stresses}} = \underbrace{-\frac{1}{\rho}\nabla \overline{p} + \nu \nabla^2 \overline{\boldsymbol{u}}}_{\text{diffusive}} + \underbrace{\overline{g}}_{\text{source}} \tag{2.4}$$

The fluctuating part is used to describe the Reynolds stress tensor, $\overline{\boldsymbol{u'u'}}$, as in Equation 2.5.

$$\overline{\boldsymbol{u'u'}} = \overline{\begin{bmatrix} u'u' & u'v' & u'w' \\ v'u' & v'v' & v'w' \\ w'u' & w'v' & w'w' \end{bmatrix}} \tag{2.5}$$

The problem with the Reynolds stress addition is that the equations contain fluctuations of velocity. As the RANS model describes the mean fluid behaviour and not the fluctuating, a closure problem is created for the Reynolds stresses. To solve this problem, the Reynolds stresses must be related to the mean flow variables.

The RANS model finds closure to the turbulence problem by averaging the Reynolds stresses and adding supplementary variables related to the turbulent viscosity and their respective transport equations (Macián-Pérez et al., 2020). A turbulence model can be applied to solve the closure problem. This can be a one-equation model, but more frequently applied are two equation models.

Two-equation models are able to provide a full description of turbulence in terms of time and length scales and hence reproducing a wide range of flow. Examples of two-equation models are the normal $k-\epsilon$ (Jones and Launder, 1972), RNG $k-\epsilon$ (Yakhot et al., 1992), $k-\omega$ (Wilcox, 1988) and $k-\omega$ SST (Menter, 1994). In this research, the $k-\omega$ SST closure model is applied.

2.1.3. Closure model

In the flow situation of interest for this research, the $k-\omega$ SST is applied. SST stands for Shear Stress Transport and the model is a two equation model for the turbulence kinetic energy, k, and turbulence specific dissipation rate, ω. It is proven to be a good turbulence closure model for separating flows (El-Behery and Hamed, 2011). Separating flows occur at the submerged underflow gate and that is the reason for the application of this closure model.

The $k-\omega$ SST closure model has been introduced by Menter (1994). It is a hybrid model that combines the $k-\epsilon$ model with the Wilcox $k-\omega$ model. Through a blending function, the $k-\omega$ model is applied near the wall and the $k-\epsilon$ model in the free stream. This is ideal as the $k-\omega$ model works well in modelling the viscous sub-layer, while the $k-\epsilon$ model works well in the prediction of flow in the region away from the wall.

For the $k-\omega$ SST model as applied in OpenFOAM (OpenCFD, 2019), the equations for turbulent kinetic energy k and the turbulence specific dissipation rate ω ((Equation 2.6 and Equation 2.7) can be found below, just as the initial conditions (Equation 2.8 to Equation 2.12).

$$\frac{D}{Dt}(\rho k) = \nabla \cdot (\rho D_k \nabla k) + \rho G - \frac{2}{3}\rho k(\nabla \cdot \boldsymbol{u}) - \rho\beta^*\omega k + S_k \tag{2.6}$$

$$\frac{D}{Dt}(\rho\omega) = \nabla \cdot (\rho D_\omega \nabla \omega) + \frac{\rho\gamma G}{\nu_t} - \frac{2}{3}\rho\gamma\omega(\nabla \cdot \boldsymbol{u}) - \rho\beta\omega^2 - \rho(F_1 - 1)CD_{k\omega} + S_\omega \tag{2.7}$$

In these equations, β, β^* and γ are default model coefficients. G, F_1 and $CD_{k\omega}$ are closure coefficients. Furthermore, D/Dt is the material derivative, ρ is the density [kg/m^3], ν_t is the turbulent viscosity [m^2/s] and S is the stress tensor.

$$k = \frac{3}{2}(\boldsymbol{u}I)^2 \tag{2.8}$$

$$\boldsymbol{u} = \sqrt{u^2 + v^2 + w^2} \tag{2.9}$$

$$I = \frac{\boldsymbol{u'}_{RMS}}{\boldsymbol{u}} \tag{2.10}$$

$$\boldsymbol{u'}_{RMS} = \sqrt{\frac{1}{3}((u')^2 + (v')^2 + (w')^2)} \tag{2.11}$$

$$\omega = C_\mu^{\frac{3}{4}} \frac{k^{\frac{1}{2}}}{l} \tag{2.12}$$

In which $\boldsymbol{u}$ is the mean flow velocity vector and I is the turbulence intensity. $\boldsymbol{u'}_{RMS}$ is the root-mean-square of the turbulent velocity fluctuations , C_μ is a turbulence model constant and l is a reference length scale.

Steenstra (2014) applies the k-ω SST closure model as well and in his report additional information on the model can be found.

2.1.4. Modelling of the free surface

In CFD the modelling approach of fluids can be based on a single fluid, or multiple fluids. In case of a single fluid, a closed system can be designed, while for multiple fluids, the interaction between the fluids has to be modelled. In this research, a one-phase modelling approach is applied. This is done with the help of a rigid lid.

The rigid lid is the application of a closed system, where the water level is modelled as a boundary. A rigid lid avoids the requirements on temporal and spatial discretization for the VoF method and it significantly reduces computation time. Deltares (2020) provides two requirements for the application of a rigid lid.

The first requirement for the rigid lid is that the ratio between measured magnitude of the free surface fluctuations and local mean water depth should be below 10%. This is an indication on how steady the free surface position is and with this limit it is expected that the error in the continuity equation is acceptable small. The second requirement is that the Froude number should be below 0.3-0.4. This estimation can be done preliminary and without any knowledge on the free surface deviations. The Froude number is defined as:

$$Fr = \frac{\overline{u}}{\sqrt{gh}} \tag{2.13}$$

In which $\overline{u}$ is the depth averaged streamwise flow velocity, g is the gravitational acceleration and h is the water depth.

2.1.5. Near-wall modelling

Near a wall, a turbulent boundary layer exists. The boundary layer has been introduced by Ludwig Prandtl in 1904 and is thoroughly described by Tulapurkara (2005). Four different turbulence regions can be defined, being the viscous sublayer, buffer layer, log-law layer and outer layer (Figure 2.2). The viscous sublayer is very close to the wall, where viscous effects dominate the flow. The buffer layer is in-between the sublayer en log-law layer, and in this region viscous and turbulent effects are of equal importance. In the log-law layer, inertial effects are dominant over viscous effects. The outer layer is the main flow region.

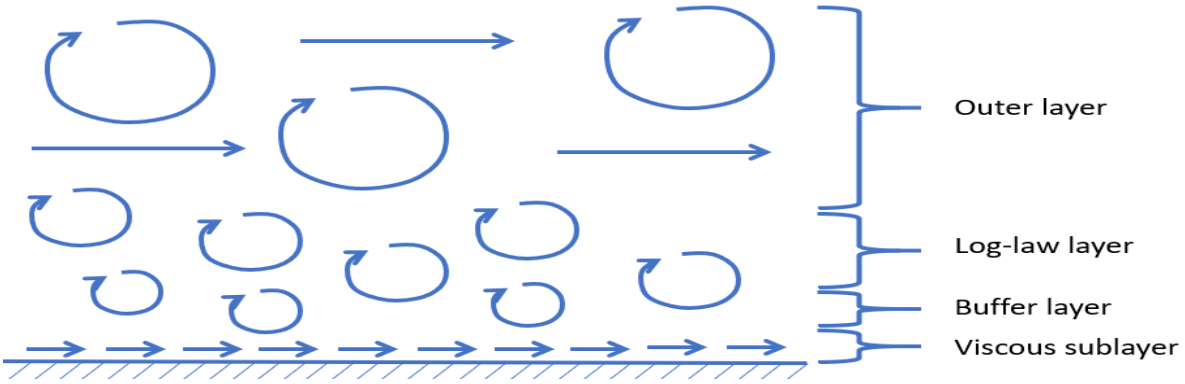

Figure 2.2: Turbulent layers near a wall

These layers can be identified with dimensionless variables, being z^+ (Equation 2.14) and u^+ (Equa-

tion 2.16), as presented in Table 2.1. Here ρ is the density, u_τ equals the shear/friction velocity, μ the dynamic viscosity and z the distance from the wall. τ_b is the wall shear stress and u is the fluid speed in horizontal (streamwise) direction.

$$z^+ = \frac{\rho u_\tau z}{\mu} \tag{2.14}$$

$$u_\tau = \sqrt{\frac{\tau_b}{\rho}} \tag{2.15}$$

$$u^+ = \frac{u}{u_\tau} \tag{2.16}$$

Table 2.1: Wall layers and regions in open channel flow

Layer	Criteria	Velocity
Viscous sublayer	0>z^+<5	u^+=z^+
Buffer layer	5>z^+<30	-
Log-law layer	30>z^+<300	$u^+ = \frac{1}{\kappa} \ln(z^+) + B$

With these dimensionless parameters defined, it is possible to look at the universal law of the wall. The law of the wall is a semi-empirical expression relating velocity to distance from the wall in a turbulent wall-bounded flow, introduced first by von Kármán (1931) and described by Uijtewaal (2003) as well. Figure 2.3 shows this law, where B is a log layer constant depending on the wall roughness. Note that there a logarithmic scale is present on the horizontal axis, indicating a logarithmic profile past z^+ equals 30.

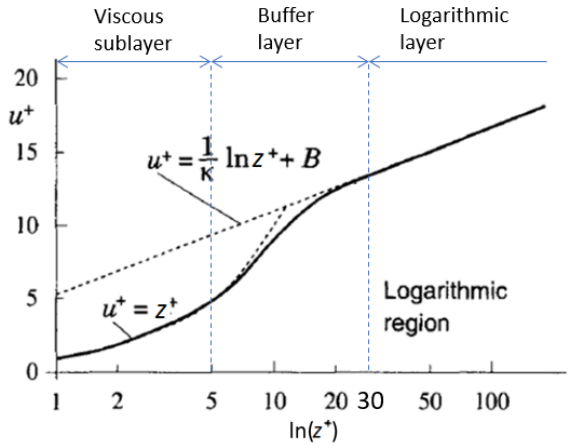

Figure 2.3: Visualisation of the law of the wall, adapted from Ferziger and Perić (2002)

The flow near a wall is an interesting part in numerical modelling. The most common option is the application of a wall function, which bridges the viscous sublayer. Wall functions reduce the computation time by allowing a coarse near-wall mesh. A disadvantage is that the influence of the viscous sublayer is ignored. Luckily, this is not important for bed protections (Steenstra, 2014). A rough wall regime is present due to the stones, making the effect of the viscous sublayer negligible.

Modelling options

As mentioned previously, the near-wall region can be modelled in two methods. One option is the application of a wall function, the other it the application of Low-Reynolds number modelling.

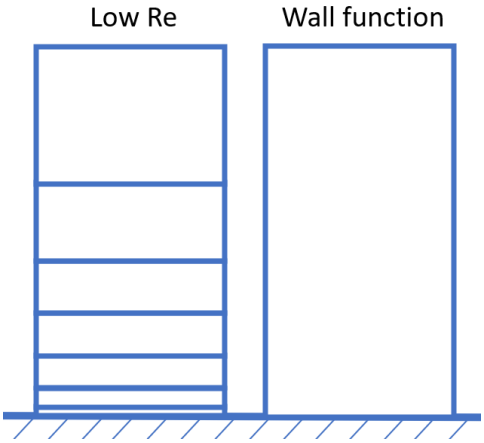

Figure 2.4: Difference between Low-Reynolds number modelling and wall functions

The main difference is that the low Reynolds number approach resolves the full wall region, while in wall function an empirical relation is applied for the region. The wall function allows a much larger cell size, reducing computation time.

Next to this, wall functions are an approximation, while low-Reynolds modelling is more accurate. The biggest advantage of wall functions is that you can add roughness into the model, while with low Reynolds modelling, one should model the rough bed exactly, stone by stone.

For the correct application of the wall functions, z_c, the height of the center of the first cell, should be situated in the log-law layer.

The presented log-law is derived for smooth walls. However, the walls of interest are rough, thus roughness should be included. The integration constant (B) in the log-law can be rewritten into the form of the equivalent roughness height (z_0^+). Now the flow near the wall can be divided into three flow regimes, namely smooth, intermediate and rough.

$$u^+ = \frac{1}{\kappa} \ln \frac{z^+}{z_0^+} \tag{2.17}$$

The bed is considered smooth when the roughness elements are submerged in the viscous sublayer. The wall is considered rough when the elements penetrate into the buffer layer or even further in the log-law layer. This can all be connected with the equivalent sand roughness of Nikuradse, k_s (Nikuradse, 1933). Nikuradse studied the uniform sand-grain roughness in pipe flow, using an average diameter to characterize the roughness height of the surface. Nowadays this roughness length, k_s, has become a widely used parameter of expressing the roughness of a wall (see Figure 2.5).

In OpenFOAM the *nutKRoughWallFunction* can be applied to take into account the Nikuradse roughness. When a wall function is used for a rough wall, the *nutkRoughWallFunction* boundary condition provides a wall constraint on the turbulent viscosity, ν_t, based on the turbulent kinetic energy, k. The wall roughness parameter B (see Table 2.1) is manipulated to account for roughness effects (OpenCFD, 2019).

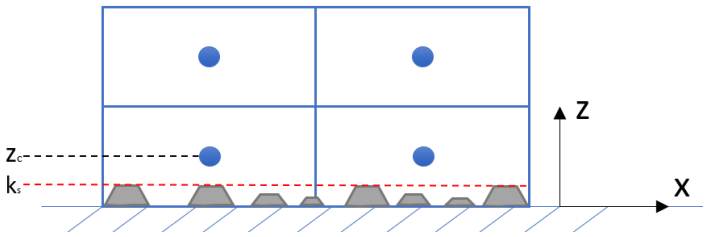

Figure 2.5: Visualisation of k_s

A summary is made in Table 2.2, where k_s^+ is the dimensionless equivalent roughness, equal to $k_s u_\tau / \nu$.

Table 2.2: Wall regions based on equivalent roughness

Regime	Criteria	z_0^+
Smooth	$k_s^+ < 5$	$0.11\nu/\lvert u_\tau \rvert$
Intermidate	$5 < k_s^+ < 70$	$0.11\nu/\lvert u_\tau \rvert + k_s/30$
Rough	$k_s^+ > 70$	$k_s/30$

The value of k_s is found as 1 to 3 times the nominal stone diameter d_{n50} (Schiereck, 2017). Martinez (2011) mentions that for the correct application of a rough boundary wall function, the position of the first cell center (z_c) has to be chosen to be larger than $0.2k_s$, while the dimensionless height of the first cell (z^+) should be between 30 and 300.

In Table 2.3 a summary is presented of the correct application of modelling a rough wall, which is essential for modelling of a bed protection and eventually designing a bed protection from model output.

Table 2.3: Requirements for rough wall modelling for incorporating a bed protection

Nikuradse roughness	k_s	1 to 3 d_{n50}
Cell center of first cell	$z_{c,0}$	$z_c > 0.2k_s$
Height of first cell	z^+	$30 < z^+ < 300$

2.2. Stone Stability

An important design criteria for bed protection is stone stability. When a stability criterion is exceeded, a stone will move and erosion will follow. A good design contains limited to no stone movement.

In this thesis the stability parameter of Steenstra (2014), ψ_{RS}, is applied. An introduction to research before Steenstra (2014) is provided in Section 2.2.1, whereas in Section 2.2.2 the applied ψ_{RS} is introduced. Section 2.2 is concluded with a flow analysis of the underflow gate and the introduction of stone damage curves of Jongeling et al. (2003).

2.2.1. Stability parameters

Approximately 100 years back the first stability relations have been determined. Isbash in 1932 and Shields in 1936 both assessed the stability of bed material for uniform flow. Isbash used the mean velocity for this, while Shields applied the shear velocity. In recent years many have proposed adapted stability formulas, mostly based on the Shields equations. These adapted formulas also tried to take into account non-uniform flows.

A first try on improving the design of granular bed protections was done by Jongeling et al. (2003). Between 2001 and 2003 they performed physical tests for multiple flow situations as flow over a flat bed, sill, underflow gate and others. Measurements were compared with a numerical model developed in CFX, which is a CFD tool of Ansys. These CFX computation results were post-processed into current load quantities.

A stability parameter was formed and with this parameter it was found that with their model output it was possible to design stable revetments. This stability parameter, and others that follow, is based on the concept of forcing and loading, as shown below in Equation 2.18.

$$\psi = \frac{\textit{loads}}{\textit{resistance}} \tag{2.18}$$

The new stability parameter ($\Psi_{u-k-crit}$) was created to a design criterion for a stable bed protection. When the computed value is larger than a threshold value, the stone will move. It should be noted that the underflow gate has not been analysed sufficiently in Jongeling et al. (2003). Therefore, the new equation mainly holds for the other flow situations. The stability parameter is given by:

$$\Psi_{u-k-crit} = \frac{(\overline{u} + \alpha\sqrt{k})^2_d}{\Delta g d_{n50}} \tag{2.19}$$

In this equation, $\overline{u}$ represents the time averaged streamwise velocity, α is an amplification factor, k is the turbulent kinetic energy, Δ is the relative density, g is the gravitational acceleration and d_{n50} the nominal stone diameter. The subscript d represents the height at which $\overline{u} + \alpha\sqrt{k}$ must be taken. Here $\overline{u}+\alpha\sqrt{k}$ represent the loads and $\Delta g d_{n50}$ represents the resistance through the weight of the stone.

Hofland (2005) continued the research by adding the entrainment rate, ϕ_E into the design process, where the entrainment rate is used as a measure of damage. This research looked better into the movement of a single stone, stating that the damage is difficult to quantify because of the random character of the flow and stone. Hofland (2005) supported his research by a 3D-RANS model with k-ϵ closure model, but stated that care must be taken when using CFD models, especially for the grid setup and boundary conditions. It is shown that the application of non-local parameters are plausible.

A scaling with the mixing length of turbulence L_{mixing} is introduced by Hofland (2005), in which the Bakhmetev distribution was applied to find a value for L_{mixing}. This Bakhmetev mixing length is denoted as L_m and is extensively discussed in Section 2.3 and Chapter 4. For now, the Bakhmetev distribution is a distribution based on the geometry of the flow.

The assumption was made that turbulent sources near the bed have a larger influence than sources higher up in the water column. For that reason a scaling function L_m/z is used. The turbulent wall pressures, which are pressure fluctuations due to turbulent eddies and not due to the bed roughness, contribute much to the loading on the bed. This effect is taken into account by an increased α value.

The adapted stability parameter by Hofland (2005), ψ_{Lm}, is presented in Equation 2.20 below.

$$\Psi_{Lm} = \frac{\max\left[\left\langle \overline{u} + \alpha\sqrt{k} \right\rangle_{Lm}^{\frac{L_m}{z}}\right]^2}{\Delta g d} \tag{2.20}$$

Equation 2.20 shows similarities with Equation 2.19. The difference mainly lies in the use of the mixing length of turbulence L_m, which is scaled with its location in the water column z. This allows to take the flow phenomena in the whole water column into account. For L_m, Hofland (2005) applies the Bakhmetev distribution, which is an estimation of the largest possible eddy due to geometrical constraints and free surface. The notation *max[..]* indicates that the maximum value throughout the whole water column must be taken.

The first research that focuses on non-uniform flow explicitly was that of Hoan (2008). In this research the equations of Shields, Jongeling et al. (2003) (from now on: Jongeling parameter) and Hofland (2005) (from now on: Hofland parameter) were examined. Hoan (2008) proves that different α values give a better correlation between the stability parameter and dimensionless entrainment rate for non-uniform flow for both the Jongeling and Hofland parameter. Next to this it is also proved that Shields is not sufficient for non-uniform flow. The newly determined stability equation is checked with numerical calculations as well and it is concluded that the equation can be used together with numerical flow

modelling output.

The stability parameter of Hoan (2008), $\psi_{u-\sigma[u]}$, is found in Equation 2.21.

$$\psi_{u-\sigma[u]} = \frac{\left\langle [u + \alpha\sigma(u)]^2 \times (1 - z/H)^{\beta} \right\rangle_H}{\Delta g d} \tag{2.21}$$

In this stability parameter, $\sigma(u) = \sqrt{\overline{u'^2}}$, z is a vertical coordinate, H is the height of the water column taken into account. Just as in ψ_{Lm}, a scaling with the location in the water column is performed with z/H. The notation $\langle ... \rangle_H$ indicates that an average over the height H above the bed must be taken, where H is smaller than the water depth. Hoan (2008) advised to apply $H = 0.7h$.

As the stability parameter of Hoan (2008), $\psi_{u-\sigma[u]}$, is dependent on the deviation of the velocity, the relation can not be estimated with the output of a RANS model. Only the output of LES models can be applied. This makes the stability parameter not of use for the goal of this thesis.

2.2.2. Stability parameter of Steenstra (2014)

After the research by Jongeling et al. (2003), Hofland (2005) and Hoan (2008), another research on stability equations has been done. In the research of Steenstra (2014) the effects of accelerating flow have been incorporated. This research combines four data sets into one stability relation. It is the last research that introduced a well calibrated stability formula and can be seen as the most extensive to date regarding granular bed protections and numerical output.

The Steenstra (2014) stability parameter, ψ_{RS}, is used in this research. A full elaboration is made in this subsection. Steenstra expected that the approach is applicable on multiple situations, as the stability parameter is based on many flow situation.

Steenstra's research approach

The research objective of Steenstra (2014) was to incorporate the acceleration or deceleration of flow, as well as the turbulence, into one stability equation. The local flow characteristics are used, instead of the depth-averaged. The main goal was to make a stability parameter which is applicable for a wide range of non-uniform flows. The thesis only deals with the acceleration in space (advective acceleration), leaving a knowledge gap in acceleration in time.

The objective of Steenstra (2014) can be subdivided in two parts. The first part is to design a stability parameter, incorporating turbulence and advective acceleration. For this the parameter must be able to be used with local flow characteristics and be applied with CFD model output. The second part is to establish a relation between the proposed stability parameter and the bed response. The experiments were based on four data sets, including Jongeling et al. (2003) and Hoan (2008). The proposed stability formula was based on three flat bed cases, a short and long sill, a flow expansion and a contraction, but the underflow gate was omitted.

New stability parameter

The newly developed stability parameter is presented in Equation 2.22, containing a drag term and an advective acceleration term.

$$\Psi_{RS} = \frac{\overbrace{\left(\max\left[\left\langle \bar{u} + \alpha\sqrt{k} \right\rangle_{Lm} \frac{L_m}{z}\right]^2\right)}^{\text{drag}} + \overbrace{C_{m:b}\left(\bar{u}\frac{\partial \bar{u}}{\partial x}\right)_{h_a} d_{n50}}^{\text{advective acceleration}}}{K(\beta)\Delta g d_{n50}} \tag{2.22}$$

with:

- $\bar{u}$ mean part of the horizontal velocity
- α empirical factor
- k turbulent kinetic energy
- L_m Bakhmetev mixing length
- z vertical direction
- C_b bulk coefficient
- C_m added mass coefficient
- $C_{m:b}$ = C_m/C_b
- d stone diameter
- K correction factor
- h_a measurement height acceleration
- β angle of the bed

This stability equation includes the quasi-steady forces (i.e. the mean velocity $\overline{u}$ and the velocities that reach the bed $\alpha\sqrt{k}$), the forces due to the advective acceleration ($\overline{u}\frac{\partial \overline{u}}{\partial x}$), a resisting force due to the weight of the stone ($\Delta g d$) and a correction for sloped beds ($K(\beta)$), which can be neglected for the underflow weir investigated in this thesis. An advantage of this formulation is that the stability parameter uses flow properties from the complete water column and can be applied to non-uniform flow.

The origin of the Bakhmetev mixing length L_m comes from the work of Hofland (2005) and a description on how to determine this length is provided in Section 2.3, while variations on the different applications can be found in Chapter 4. In the original application of Steenstra, the mixing length is approximated through the Bakhmetev distribution, also elaborated further in Chapter 4.

Steenstra (2014) applied a statistical method to determine the constants. These constants are expressed in α, C_m, C_b and h_a/d_{n50}. In ψ_{RS}, $C_{m:b}$ is a ratio between C_m and C_b and this ratio is used as input. For explanation, the parameters are elaborated below, just as the other constants. The values that must be applied in the equation can be found in Table 2.4.

- C_b The relative importance of the force caused by velocity and turbulent velocity fluctuations, determined by the method as applied in Hofland (2005).
- α The importance of the turbulent velocity fluctuations represented by $\sqrt{k}$ relative to the mean velocity.
- h_a/d_{n50} A ratio of the height above the bed h_a and stone size d_{n50}, indicating at which location the advective acceleration, that is used to calculate the acceleration force on a stone, is determined.
- C_m The relative importance of the force caused by acceleration.

Table 2.4: The values for the constants in the Steenstra stability formula, based on largest correlation (R^2) (Steenstra, 2014)

Constant	Value
α	3.75
$C_{m:b}$	23.0
h_a/d_{n50}	9.0

The relation between the Steenstra stability parameter and the entrainment rate is as follows:

$$\phi_E \equiv 3.95 \cdot 10^{-9} \psi_{RS}^{5.89} \qquad \text{for} \quad 0.9 < \psi_{RS} < 4.3 \tag{2.23}$$

As a value for the entrainment rate that indicates *start of stone movement*, the value of 10^{-8} can be used (Stevens, 2018). This can be converted to a requirement for the stability parameter, in which stones do not move (Equation 2.24 and Equation 2.25). This is supported with Figure 2.6.

$$2.124 \cdot 10^{-9} < \phi_E < 10^{-8} \tag{2.24}$$

$$0.9 < \psi_{RS} < 1.2 \tag{2.25}$$

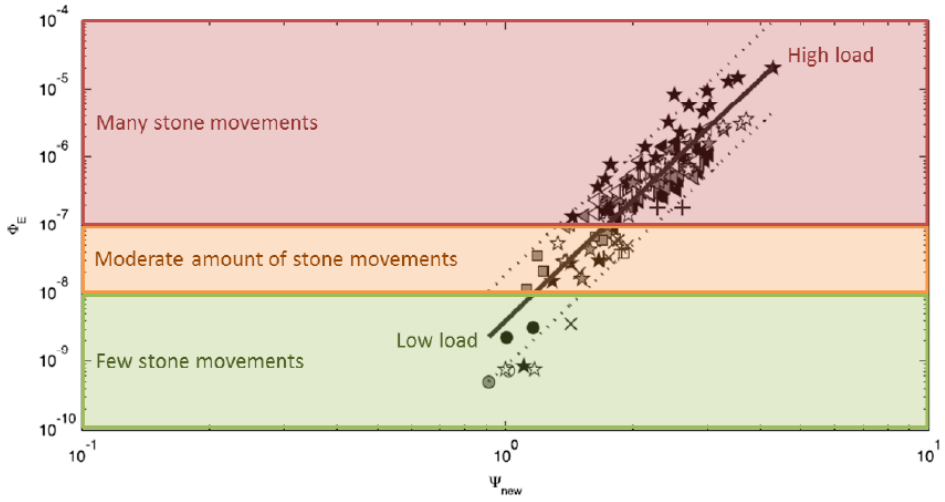

Figure 2.6: Indication on the different values for the entrainment rate, ϕ_E (Stevens, 2018)

Numerical validation of Steenstra (2014)

Steenstra found a good comparison on the modelled velocity profiles, while the turbulent kinetic energy k showed differences up to 50%. Despite that, the conclusion was drawn that the model could be applied, as the velocity output was the essential output. Figure 2.7 and Figure 2.8 provide an example of the validation of Steenstra (2014) for the long sill, showing the agreement in velocity and the difference in turbulent kinetic energy. In Chapter 3 the validation of the created model for this thesis is provided. The validation of the rough bed models is based on the same approach as Steenstra (2014).

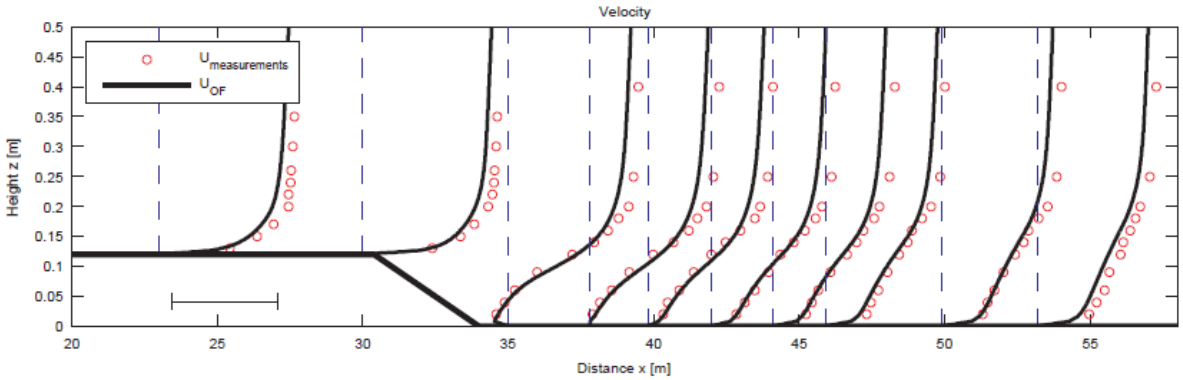

Figure 2.7: Comparison of the velocity [m/s] of the OpenFOAM output of Steenstra (2014) and measurements of Jongeling et al. (2003)

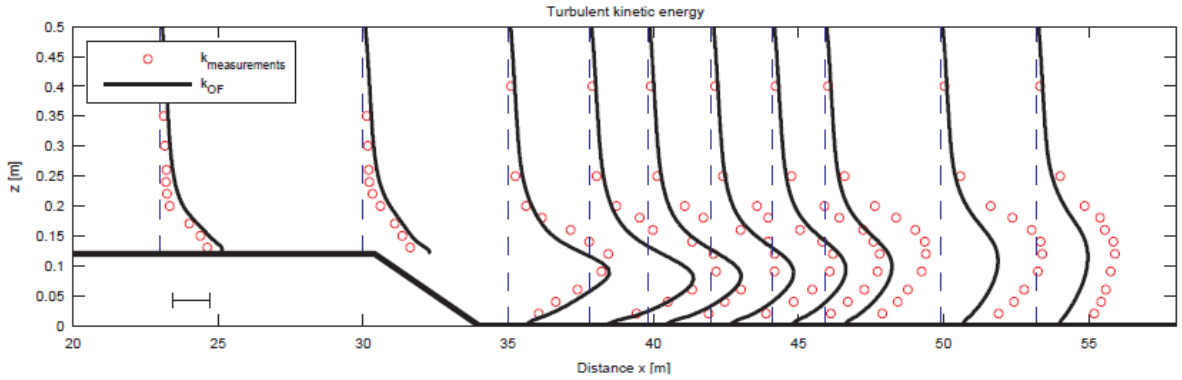

Figure 2.8: Comparison of the turbulent kinetic energy [m^2/s^2] of the OpenFOAM output of Steenstra (2014) and measurements of Jongeling et al. (2003)

Application of Steenstra

Eight steps are provided on the application of the Steenstra equation. The determination of the required stone size is an iterative process, as the changed stone diameter also changes the flow. As this implies multiple models, practicality is desirable. Jongeling et al. (2003) found that one iteration step is sufficient. The design steps are provided below:

1. Determine the critical entrainment rate $\phi_{E,c}$, indicating the threshold of motion. Stevens (2018) concluded that a value of 10^{-8} is the valid approximation for $\phi_{E,c}$.
2. Compute the critical stability parameter $\psi_{RS,c}$ according to Equation 2.23.
3. Estimate a first design stone size and apply this stone size in the numerical model with a wall function.
4. Use the model output and Equation 2.22 at the locations of interest and compute the prototype stability parameter, $\psi_{RS,p}$.
5. Compare $\psi_{RS,p}$ with the critical value $\psi_{RS,c}$.
6. Find the weak spots and increase the stone size with Equation 2.26. Here γ is a safety factor, d_{design} is the design stone size for stability and d_p is the prototype stone size, or model stone size..
7. Repeat the steps until values are found where $\psi_{RS,p}$ is lower than $\psi_{RS,c}$.

$$d_{\text{design}} = \gamma \frac{\Psi_{RS,p}}{\Psi_{RS,c}} d_p \tag{2.26}$$

The Steenstra equation in relation to the entrainment rate is only valid within a certain range, see Equation 2.23. Linked to the entrainment rate for initiation of motion this leads to a critical stability parameter ψ_{cr} = 1.2 (shown in Equation 2.25). This is the value that is used as reference for the stone stability computations.

2.2.3. Flow phenomena

The focus of this research is to develop a numerical modelling design methodology for rip rap bed protections downstream of an underflow weir. Before the numerical model is introduced, first an overview of the flow phenomena is given. This is done trough a generalized gate (Figure 2.9).

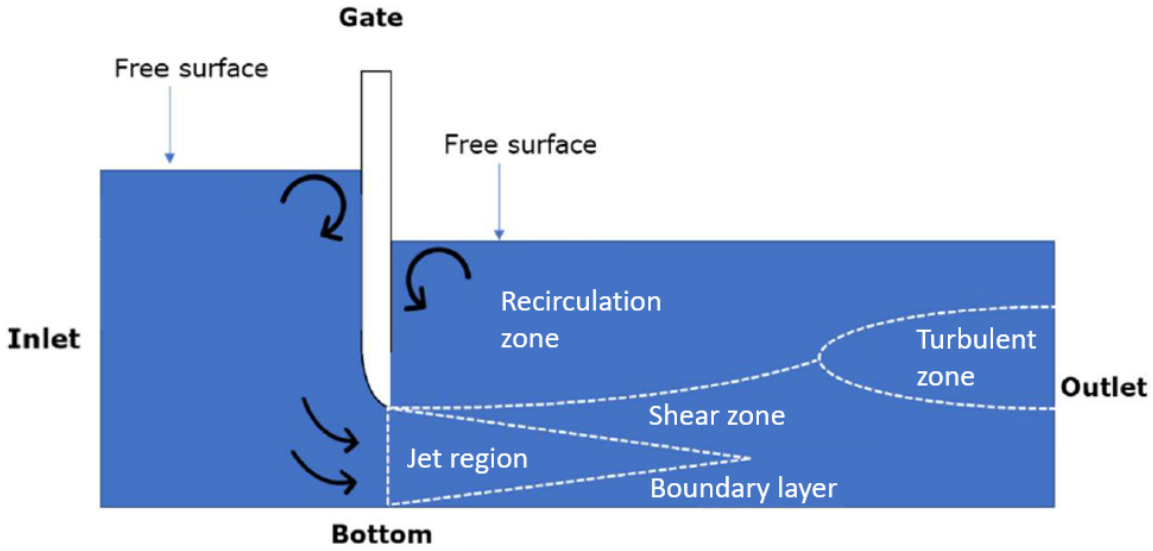

Figure 2.9: Flow phenomena indication for a generalized underflow gate, based on Deltares (2020)

The flow can be characterised by three properties. The first is the jet region. In this region the flow velocities are the largest. In this area the flow velocity fluctuations are low to almost zero, meaning that almost no turbulence is produced here.

The second is defined by the shear zone and boundary layer. Above the jet region, flow separation occurs and a shear layer develops. Near the bottom a boundary layer develops because of the low flow velocities very close to the bed and larger velocities just above the bed. When the jet region ends, the shear layer and boundary layer meet. At this region the turbulence increases and turbulent mixing occurs, i.e. turbulent zone.

The third property is found above the shear zone, where the flow reverses direction and a recirculation zone is created. In this recirculation zone a hydraulic jump takes place at the transition from supercritical to sub-critical flow. This jump can either be submerged or non-submerged. Hydraulic jumps downstream underflow gates in rivers are known to be submerged due to the large water level downstream of the gate.

2.2.4. Varying location of acceleration term

The underflow gate differs from the flow situations taken by Steenstra (2014). At the gate, an increased flow velocity is near the bottom, while for a flow situation as a flat bed, this is higher up in the water column. This raises the idea of not taking the original approach with $h_a = 9d_{n50}$, but shifting the location towards the center of the jet. The center of the jet is the location in the jet with the largest velocities (see Figure 2.10).

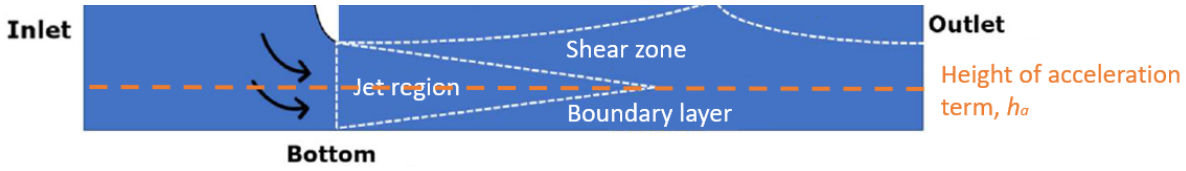

Figure 2.10: Indication of the height of the adapted acceleration term h_a

Steenstra (2014) provides a correlation table (Table 2.5) for different heights for the acceleration term in the stability parameter. With this table it is possible to scale the height, but a large remark must be made as it was not designed for an underflow gate.

An advantage of this approach is that for larger stone sizes, the ratio between h_a and d_{n50} can be

scaled to the jet region. Otherwise inconvenient situations can exist where the location of the acceleration term, and the location with maximum drag force on the bed do not match well.

As an example, for the roughness value of $k_s = 0.023$m, taking $k_s = 2d_{n50}$, and gate height of 0.06m, the location where the acceleration term is computed is $h_a = 9d_{n50} \approx 0.1$m. The largest velocities occur at approximately 0.03 meter. This results in a mismatch as the location of h_a is far above the location where the largest velocities are measured and thus where the largest velocities in the jet region, leading to stone instability at the bed, is expected. For this reason it is chosen to scale the location of measuring the advective acceleration towards the center of the jet and perform the stability computations with these values.

Table 2.5: Constants α and $C_{m;b}$ for different values of h_a, leading to the largest correlation R^2 (Steenstra, 2014)

h_a/d_{n50}	α	$C_{m;b}$	R^2
1.0	0.5	24.0	0.6856
2.0	1.0	14.0	0.7093
3.0	1.5	12.0	0.7274
4.0	2.0	14.0	0.7537
5.0	3.75	18.0	0.7739
6.0	3.00	19.0	0.7886
7.0	3.50	22.0	0.7967
8.0	3.75	23.0	0.7998
9.0	3.75	23.0	0.8003
10.0	3.75	23.0	0.7969
20.0	3.75	22.0	0.7905

2.2.5. Stone damage curves

The underflow gate has been tested by Jongeling et al. (2003) in a physical flume. As a results of these tests stone damage curves were created. These curves are helpful for comparison between numerical computations and physical tests and show the number of stones moved per stripe of 10 centimeter downstream of the gate. The stone damage curves were created for two underflow gate cases and are provided below.

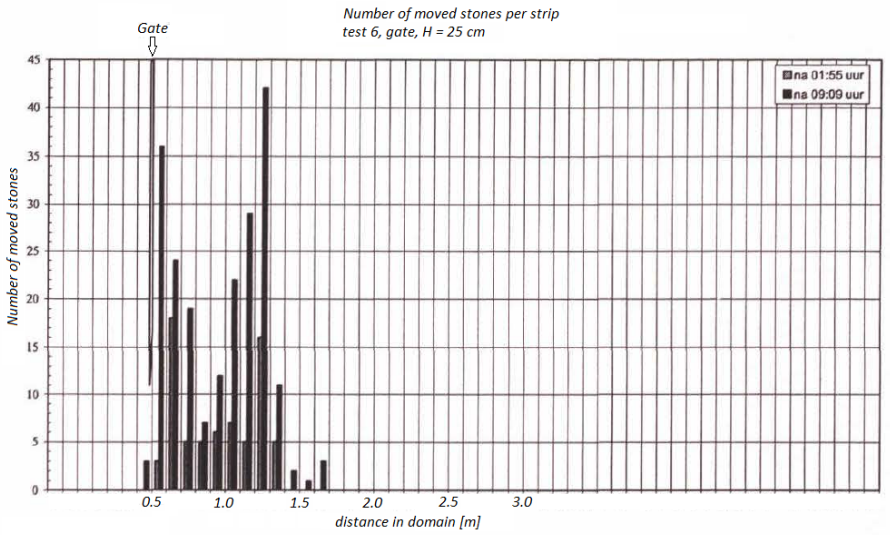

Figure 2.11: Stone damage curve of test 6 from Jongeling et al. (2003).

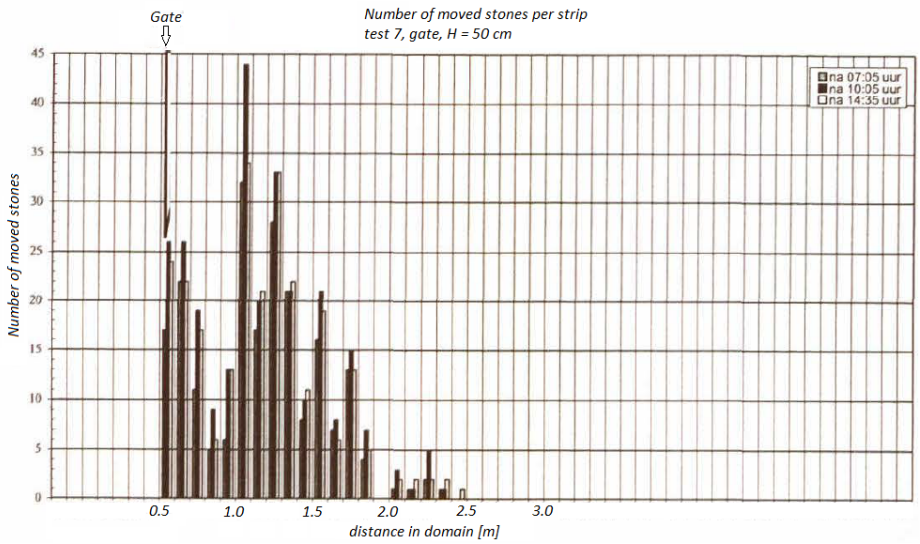

Figure 2.12: Stone damage curve of test 7 from Jongeling et al. (2003).

The damage patterns show two distinctive areas. The first peak between approximately 0.5 and 0.8 meter is created by increased velocity in that region. Due to the flow contraction underneath the gate, the velocity rises and the threshold of motion is exceeded.

The second peak is due to the increased turbulence. This turbulence creates large eddies that induce the motion of stones. These figures show the importance of including the turbulence into the stability computations.

2.3. Turbulence length scale

The flow situation in the different cases is highly turbulent. A turbulent flow field can be considered to consist of whirling motions (structures or eddies) of different sizes or scales, of which the turbulence length scale is a measure for the eddy scale sizes in turbulent flows. The size of these eddies is important for the application of the stability parameter of Steenstra (2014).

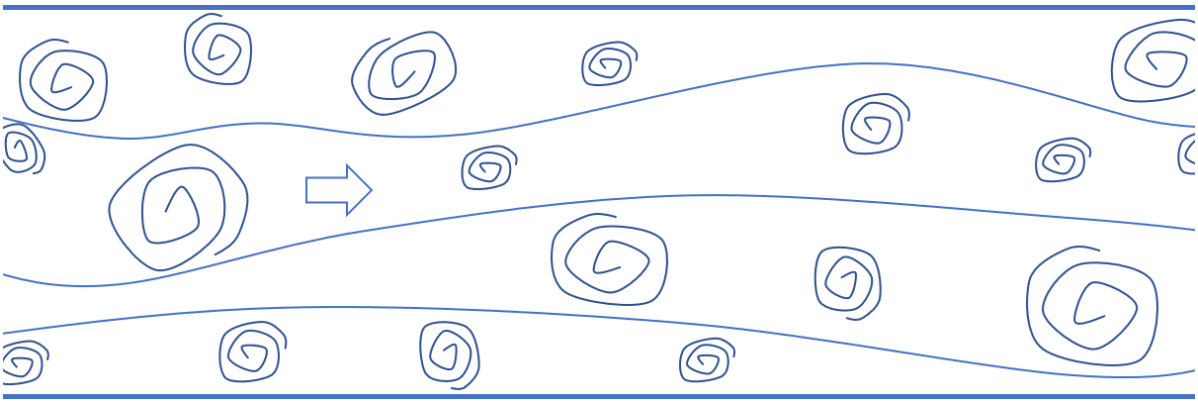

Figure 2.13: Schematisation of flow and eddies in a turbulent flow

Turbulent flows are dissipative and large eddies dissipate into smaller eddies. The energy cascade describes the transition from large eddies, to smaller eddies, to the smallest eddies possible in the flow region. The energy transfer continues until the eddy motion is stable and is then converted into heat.

Turbulence will give rise to velocity fluctuations in the horizontal (velocity u) and transverse (velocity v) and vertical (velocity w) directions characterized by u', v' and w'. A visualisation of the coordinate

system is found in Figure 1.4. The associated momentum fluctuation is called the turbulent shear stress or Reynolds stress and for a 2D situation, this value is presented below.

$$\tau_{turbulence} = -\rho\overline{u'w'} \tag{2.27}$$

Eddy viscosity is a coefficient relating the average turbulent shear stress within a turbulent flow of water to the vertical gradient of velocity, thus the eddy viscosity can be seen as the product of a velocity and a length scale. The concept of the eddy viscosity is fundamental for the description of the velocity profile in turbulent flow and allows the determination of the bed shear stress exerted by rivers on particles on the river bed.

The first approach on defining this bed shear stress is from Prandtl, who suggested in 1925 to apply the turbulence length scale to describe the distribution of the turbulent eddy viscosity (Uijtewaal, 2003). In short, the Prandtl mixing length theory can be defined as the average distance that a small mass of fluid will travel before it exchanges its momentum with another mass of fluid.

Following the Prandtl mixing length hypothesis, the velocity that characterizes the turbulent fluctuations is proportional to the velocity difference in the mean flow over a distance l over which the mixing or transport of momentum takes place, and is given by:

$$|u'| \sim |w'| \sim l\frac{d\bar{u}}{dz} \tag{2.28}$$

Combining Equation 2.27 and Equation 2.28 and using l again as the governing length scale, the eddy viscosity can be written as the product of this length scale squared and the local velocity gradient, thus:

$$\tau_{turbulence} = -\rho l^2 \left(\frac{d\bar{u}}{dz}\right)^2 \tag{2.29}$$

With the method of Prandtl the problem of determining the eddy viscosity reduced to determining the mixing length l.

After Prandtl, von Karman hypothesized that the mixing length should be proportional to the distance from the boundary: $l = \kappa z$, in which κ is the von Karmann's constant, the turbulent momentum exchange coefficient, equal to 0.41.

The mixing length in open channel flows can be described with the Bakhmetev distribution (Uijtewaal, 2003). This mixing length is denoted as L_m (Equation 2.30) and is based on a relation between the shear stress τ_b, shear velocity u_τ and turbulent viscosity ν_t. The research on this mixing length is based on the assumption of a straight, wide river, channel or flume with a two-dimensional approach. In this situation, the logarithmic velocity profile holds.

$$L_m = \kappa h\gamma(1-\gamma)^{\frac{1}{2}} \tag{2.30}$$

In which κ is the von Karmann's constant, h is the water depth, γ is a ratio between a location in the water column z and the water depth h, being $\gamma = z/h$.

This mixing length approach leads to a mixing length of zero at the free surface and bottom, thus to a turbulent viscosity equal to zero. More on the application of the Bakhmetev mixing length is found in Section 2.3.1 and Chapter 4.

Concluding, the turbulence length scale is an indication for eddy scale sizes in a water column. As this length scale is determined, it is possible to take the turbulent shear stress into account. This turbulent shear stress is essential for determining the shear stress, or drag force, exerted by the river on the bed. The mixing length is needed for the application of the equation of Steenstra (2014), first implemented by Hofland (2005).

2.3.1. Application of the mixing length in Hofland (2005)

Through the mixing length and the relative importance of the velocity sources above the bed, Hofland (2005) proposes a method for the estimation of a representative 'maximum velocity' near the bed. This maximum velocity is an indication for the 'maximum' quasi-steady force on the bed.

Steenstra (2014) used the same methodology as described by Hofland (2005), while adding a term for advective acceleration. For a complete understanding of the mixing length, it is important to dive into the Hofland parameter and its application first.

Incorporation of the length-scale

Hofland (2005) had shown that in uniform flows and backward-facing-step flows, large-scale structures with increased velocity exist. This led to the reasoning of the application of velocity sources of the whole water column above a stone, in order to estimate the quasi-steady forces. These turbulent structures are in the order of the water depth and occur during the entrainment of the stone ϕ_E, where entrainment is the previously described indication of damage to the bed. These structures are the basis for the applied relation in the Hofland equation, as described in Section 2.2. A model of such an eddy is schematised in Figure 2.14.

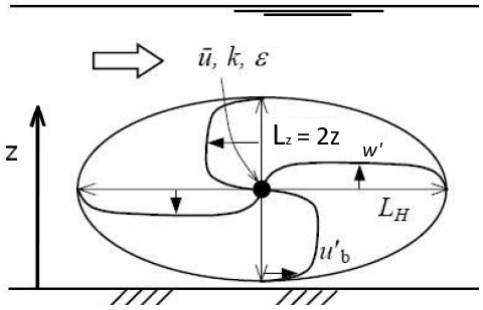

Figure 2.14: Stigmatization of a large eddy that influences bed stability (Hofland, 2005).

It is posed that the structure consists of a large rolling structure with a horizontal length-scale L_H and vertical length-scale of $2z$, in which z is the height of the center of the structure above the bed. Next to this it is assumed that the large-scale vertical velocity fluctuations are proportional to $\sqrt{k}$. Based on the conservation of mass and the transport of mean momentum towards the bed, the following velocity estimate near the bed is obtained:

$$u_b \propto \frac{L_H}{z}(\bar{u} + \alpha\sqrt{k}) \tag{2.31}$$

Where $\bar{u} + \alpha\sqrt{k}$ is the estimate for the temporal 'maximum' of the local velocity, containing the mean velocity $\bar{u}$ with its fluctuations $\alpha\sqrt{k}$. The computed value is scaled with its location in the water column through L_H/z, where z is a value between the bed and water surface.

As an estimate for the large-scale turbulence intensity at height z, the mean value of turbulence intensities over a height between $z \pm L_H/2$ is taken. This value is multiplied with L_H/z in order to obtain the influence of the turbulence at height z on the bed. This process is repeated for multiple values of z between $0 < z < h$. The maximum obtained value in this process is taken as input in the stability parameter of Hofland (2005), see Equation 2.20. This maximum value serves as a representative value for the extreme (drag) velocity near the bed, taking the full water column into account.

Mixing length approach

A value for the mixing length L_{mixing} had to be found by Hofland (2005) in order to apply the proposed method for the incorporation of the mixing length. Two length-scales have been investigated by Hofland (2005), namely the dissipation length L_ϵ and the Bakhmetev mixing length L_m. It was concluded by Hofland that the dissipation length cannot be applied, while the Bakhmetev mixing length performs well. For that reason, the Bakhmetev distribution is tested in this study.

The Bakmetev mixing length consists of a determination of the mixing length, based on the Bakhmetev

distribution. This distribution is derived for a uniform open-channel flow. The distribution can be found in Equation 2.32, where $\gamma = z/h$.

$$L_m = \kappa h \gamma \sqrt{1-\gamma} \tag{2.32}$$

In Hofland (2005) the Bakhmetev mixing length L_m is used, despite the fact that it is derived for uniform open-channel flow. It is stated that when applying this distribution for non-uniform flows, as is the case for the investigated underflow gate in this thesis, the Bakhmetev distribution is more an estimate for the largest possible structure due to the geometrical constraints of the bed and water surface.

This distribution has a maximum near the bed, inducing that the forces near the bed have larger influence than forces higher up in the water column. Hofland (2005) concludes that this seems an acceptable weighting function for the velocity sources. Plots of this distribution and application of it on the underflow gate case is provided in Section 4.1.

3

Underflow gate

In Chapter 3 the data sets that are used for validation of the numerical models is provided. Next, the model setup is given after which the validation of the numerical model with smooth and rough bed is given. An introduction into the flow phenomena of an underflow gate can be found in Section 2.2.3.

3.1. Validation data

Two data sets are used for validation. One is the data set of Deltares (2020), containing PIV measurements of several gate openings with a smooth bed. The second is the reference measurements of Jongeling et al. (2003), containing stone damage curves. Jongeling et al. (2003) had an introduction in Chapter 2 and the data used for validation will be elaborated here.

3.1.1. Validation data of Deltares (2020)

Deltares provided a data set of a research on CFD validation for an underflow gate, which has been performed in 2020 (Deltares (2020)). In this research the underflow gate with three different gate heights of 0.02m, 0.06m and 0.15m have been physically modelled and afterwards numerically modelled. In this section the data set and research is elaborated, as well as the possibilities on the validation of the numerical model created in this research.

With the help of particle image velocimetry (PIV) measurements, time-averaged flow fields are characterized, making it possible to assess flow velocity and turbulence near the bed downstream of the gate, as well as in the water column. Numerical modelling of the gate has been performed with the commercial CFD software package STAR-CCM+ v14.04.

Experimental setup

The experimental setup, used for the research of Deltares (2020), is presented in Figure 3.1. With the help of the flow straightening device (a), the right inflow conditions are created. A gate is placed over the full width of the setup. The gate has a thickness of 25 mm and the bottom part is rounded, such that the upstream side of the gate intersects the downstream side at an angle of 70 degrees. The water level is set using a point gauge measuring the water level (e) and measured 4.6 m downstream of the gate with a point gauge (g) as well. A flow meter takes care of measuring the flow discharge in the setup. The upstream water level is set to 400 mm above the floor underneath the gate and three different gate opening heights were tested: 20 mm, 60 mm and 150 mm. Output of the experiments is PIV data containing detailed velocity measurements.

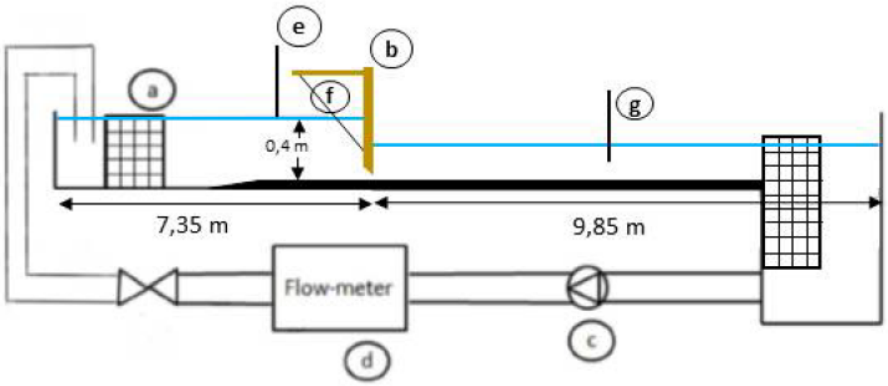

Figure 3.1: Schematic layout of the flume. a: flow straightening device. b: underflow gate. c: pump. d: flow meter. e: level staff. f: wires. g: wave gauge. (Deltares, 2020)

Two results of the PIV measures are presented below, which are the velocity and turbulent kinetic energy downstream of the gate with gate opening of 0.06 meter. The measurements reach until a distance of 1.2 meter from the gate and are divided in three equal parts of 0.4 meter.

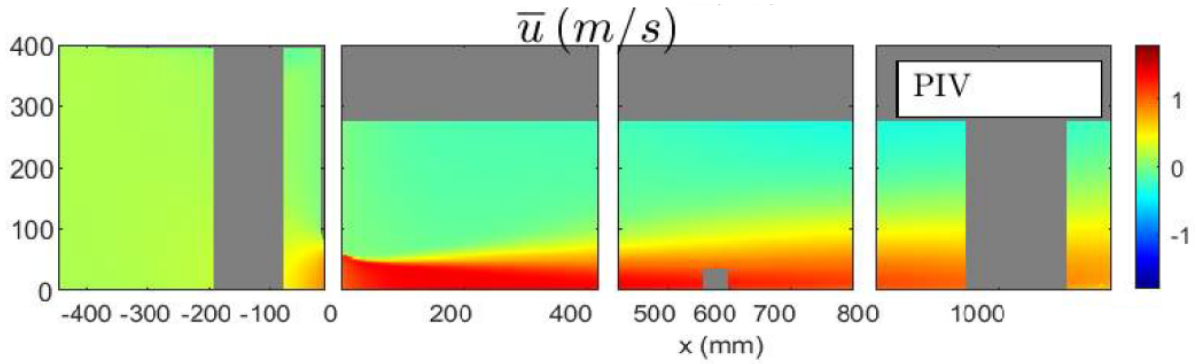

Figure 3.2: Velocity profile downstream of the gate with opening b_0 of 0.06m (Deltares, 2020)

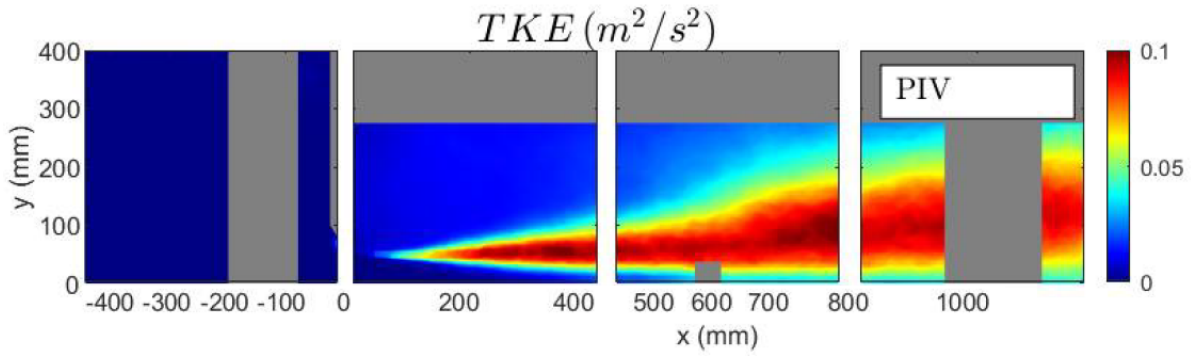

Figure 3.3: Turbulent kinetic energy profile downstream of the gate with opening b_0 of 0.06m (Deltares, 2020)

CFD model input and boundary conditions

Figure 3.4 provides the schematic representation of the domain and boundary conditions. The model applied is a 3D-URANS, which is the transient form of the Reynolds-Averaged Navier Stokes equations. The turbulence closure models applied are the Realizable k-epsilon two-equation model, Reynolds Stress Model (RSM), and Detached Eddy Simulation (in IDDES variation).

The model consist of two phases, air and water, and is modelled through the VoF method. In Deltares

(2020) it is shown that the depth averaged Froude numbers are below the threshold of 0.3-0.4, which is suggested as the upper limit for the rigid-lid applicability. The rigid-lid reduces computation times significantly, while here it was chosen to apply the VoF method, as it allows to investigate mesh sensitivity and solver requirements for the time step.

A wall function is applied in the model, as it is known to give a good approximation for flows with high pressure gradients. It allows the use of a relatively coarse computational mesh in the near wall region.

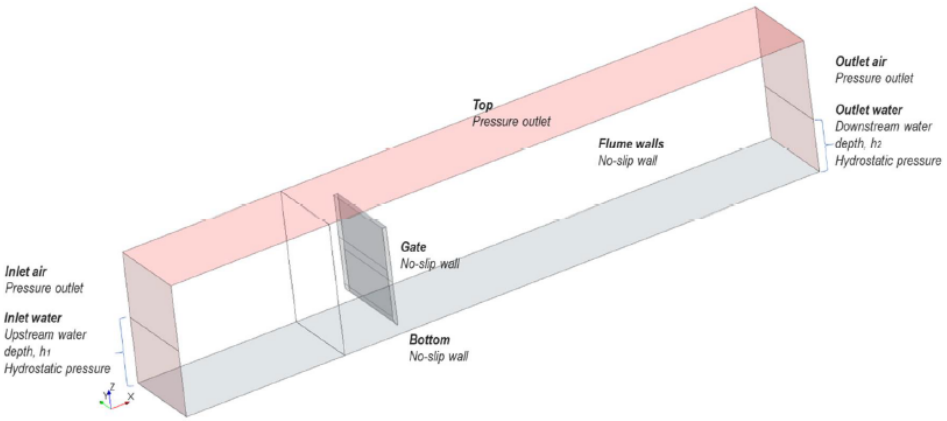

Figure 3.4: Schematic representation of domain and boundary conditions (Deltares, 2020)

The setup for the different validation cases is presented in Table 3.1. The mesh was divided in a coarse and fine part.

Table 3.1: Summary of validation setup (Deltares, 2020)

		Case 1	Case 2	Case 3
Gate opening, b_0	m	0.02	0.06	0.15
Upstream water depth, h_1	m	0.40	0.40	0.40
Downstream water depth, h_2	m	0.25	0.32	0.37
Head difference, D	m	0.15	0.08	0.03
Target discharge, Q	m^3/s	0.014	0.032	0.037
Discharge coefficient, μ	-	0.816	0.851	0.643
Jet Reynolds numbers, Re_h	-	9400	44000	105000
Fine mesh	cells	23.1E6	25.9E6	32.9E6
Coarse mesh	cells	4.8E6	6.7E6	8.7E6

Modelling results & research observations

Comparison has been made between the PIV results and CFD Reynolds Stress Model by Deltares (2020). This comparison is done by Deltares (2020). The comparison with the OpenFOAM model created for this thesis is done in Section 3.2. Figure 3.5 presents the mean velocity profiles for ten different distances downstream of the gate. Their modelled velocity profiles show good comparison. The Reynolds stresses are compared as well and are presented in Figure 3.6. The peaks are in comparison but have a smaller width compared to the PIV measurements.

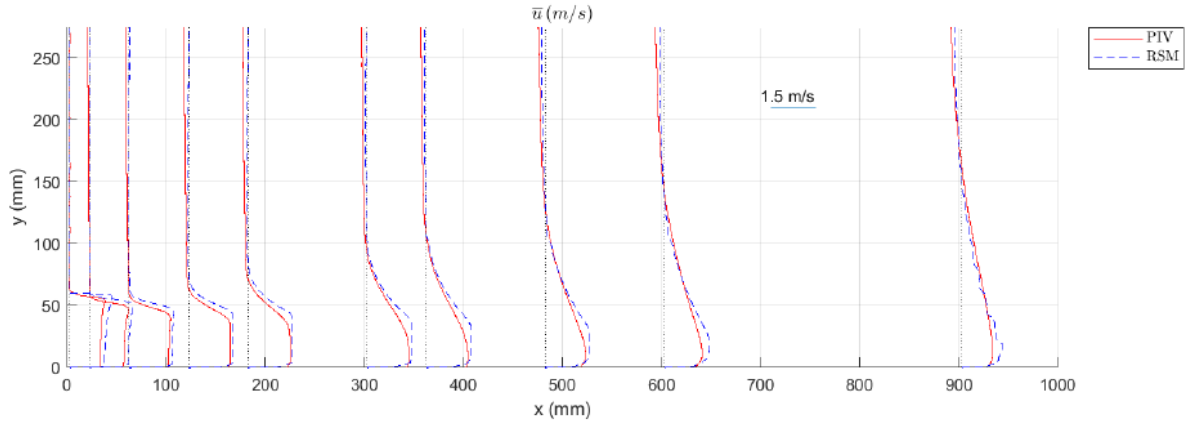

Figure 3.5: Modelled velocity profile downstream of the gate with opening b_0 of 0.06m compared to measured PIV data (Deltares, 2020)

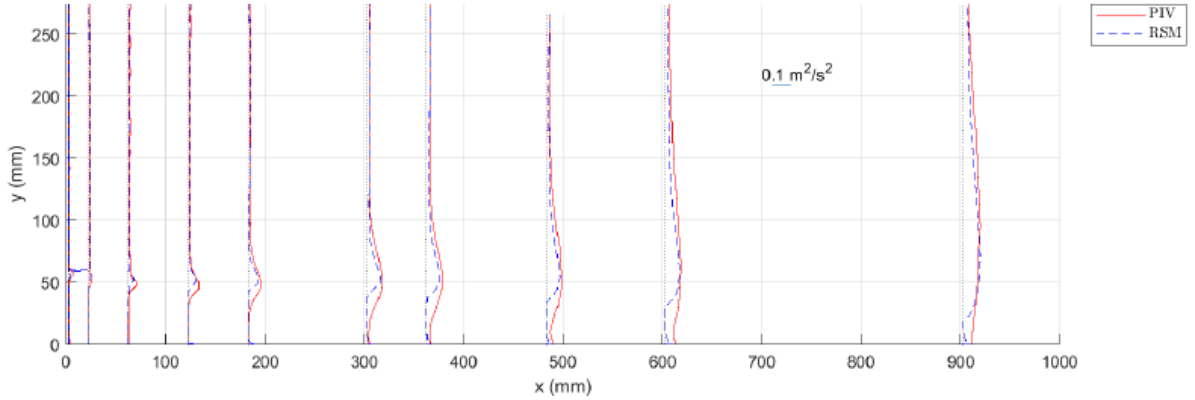

Figure 3.6: Modelled Reynolds stress profile downstream of the gate with opening b_0 of 0.06m compared to measured PIV data (Deltares, 2020)

Overall it can be said that the velocities show agreement between the CFD predictions and PIV measurements. For all simulations, the maximum difference in velocity profiles is 6%. When converting the Reynolds stress to turbulent kinetic energy, it can be seen that the numerical model underestimates the size and magnitude of the measured turbulent kinetic energy downstream of the gate. This must be taken into account in the modelling process and the further computation of a stone size.

3.1.2. Validation data of Jongeling et al. (2003)

The research of Jongeling et al. (2003) contains two setups that are of interest for this research. The setups both contain a gate opening of 0.15m, while the water depth and velocity variate. An overview of both setups can be found in Table 3.2. Measurement profiles are provided, as well as stone damage curves. These damage curves have been introduced in Section 2.2.3 and in the research of Jongeling et al. (2003) these tests are referred to as test 6 and test 7.

Table 3.2: Overview of case setup (Jongeling et al., 2003)

		Test 6	**Test 7**
Gate opening, b_0	m	0.15	0.15
Upstream water depth, h_1	m	0.25	0.5
Downstream water depth, h_2	m	0.23	0.475
Head difference, D	m	0.02	0.025
Target discharge, Q	m^3/s	0.05	0.045
Nominal stone diameter, d_{n50}	m	0.0062	0.0062

The test setup of Jongeling et al. (2003) is provided in Figure 3.7. The main difference with the testing installation of Deltares (2020) is that the gate has its angle at the lowest tip of the gate into the other direction and that stones are included in the flume.

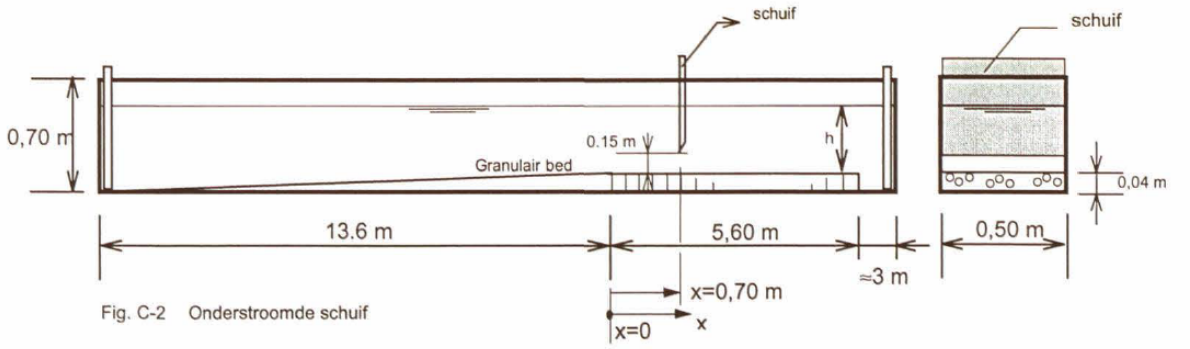

Figure 3.7: Physical testing setup of Jongeling et al. (2003)

Experimental results
The velocity and turbulent kinetic energy profiles of the physical tests for the underflow gate by Jongeling et al. (2003) can be found in Appendix D, Figure D.1 to Figure D.4. The patterns compare to the measurements from Deltares (2020) in jet region and profiles. The comparison of the OpenFOAM models created for this thesis with the data of Jongeling et al. (2003) follows in Section 3.3.

The main difference between the other data set is that in the tests of Jongeling et al. (2003) a bed roughness has been included in the measurements. This allows the comparison to OpenFOAM models with bed roughness incorporated.

3.2. OpenFOAM model with smooth bed

In order to make a validation against the PIV data of Deltares (2020), it is important to create a model with a smooth bed and no bed protection. Bed protection can be added after the model is validated and the computation errors are known. In Section 3.2 the geometry, numerical setting and model output is presented. For the smooth bed validation, only the gate with gate opening b_0 of 0.06 m is investigated.

Deltares (2020) showed the computed depth averaged Froude numbers for the gate opening of 0.06 m (Figure 3.8). The figure shows that when the velocity increases near the gate, the Froude number rises, but the maximum value found is 0.19. This stays below the value of 0.3, which is the threshold for whether or not to apply the rigid lid method. This is the reason that a rigid lid is applied in this research as well.

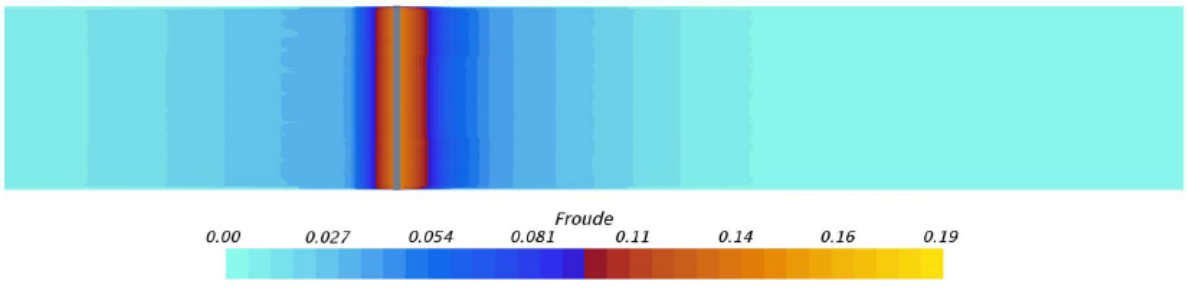

Figure 3.8: Froude number over the depth for gate opening of 0.06m. The gray bar is the location of the gate. Flow is from left to right (Deltares, 2020)

3.2.1. Geometry

The setup for the grid can be found in Table 3.3. An image of the full mesh can not be made, as the mesh is too fine. For that reason the refinement region around the gate is shown, presented in Fig-

ure 3.10. The dimensions of the cells are based on the value that is used as input for the bed roughness.

Even though the flume of Deltares (2020) is mentioned as smooth, a surface is never completely smooth. This is the reason that for the developed model the roughness of smooth concrete is taken, which is assumed as k_s equal to 0.002 m. The application of k_s in the nutkRoughWallFunction gives a minimal cell center height of $0.2k_s$, which leads to a minimal cell height of the bottom cell of 0.0008 m. This lead to the decision of a height of 0.001 m. This is necessary for the wall function to work properly.

An advantage of a numerical model is the fact that the domain can easily be extended downstream of the gate, further than the PIV measurements. If the area with both PIV and OpenFOAM results show good comparison, it can be expected that further downstream the OpenFOAM model will model it correctly. This is the reason that the domain has been extended to 4.5 meter past the gate (see Figure 3.9).

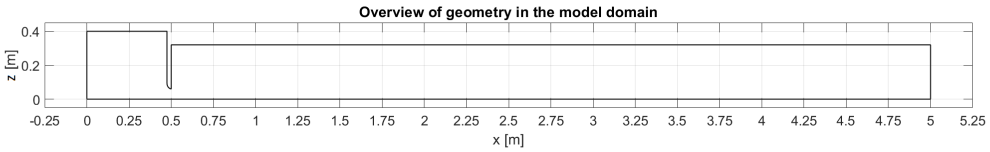

Figure 3.9: Overview of the geometry in the modelled domain. Location of the gate at x = 0.5m

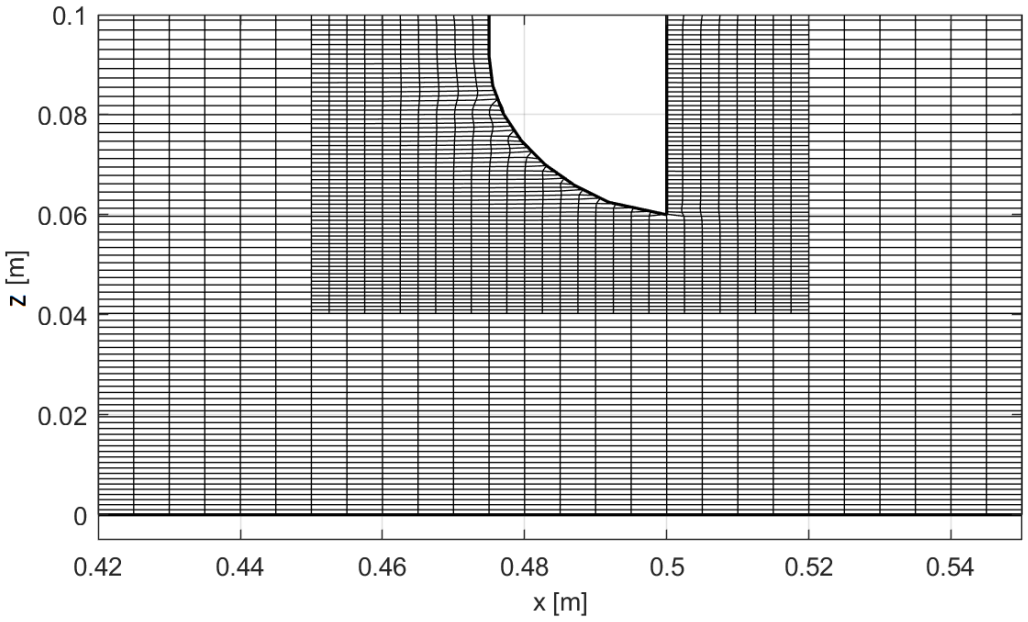

Figure 3.10: Visualisation of mesh near the bed and the refinement around the gate for the OpenFOAM model with a smooth bed

Table 3.3: Mesh characteristics for the smooth bed validation with gate opening b_0 of 0.06 m

Variable	Value
Cell height bottom	0.0001 m
Cell height top	0.0005 m
Cell-to-cell expansion ratio	1.01
Total expansion ratio	5
dx	0.005 m
N_x	1000
N_z	161
k_s	0.002

3.2.2. Numerical settings

The boundary and initial conditions are provided in Table 3.4. At the inlet a fixed velocity of 0.16 m/s in the streamwise direction has been set. Other computed values are the inlet omega, inlet nut and inlet k. These are based on the flow properties of the modelled flow situation. The nutkRoughWallFunction can be found at bottom nut.

Equation 3.1 to Equation 3.5 are applied in the determination for the computed inlet conditions. These are supported by the application of a free stream velocity $\boldsymbol{u}$ of (0.16, 0, 0) m/s, kinematic viscosity ν of 1E-6 m^2/s, turbulence intensity I of 0.05 (5%) and turbulent viscosity ratio μ_t/μ of 10.

$$k = \frac{3}{2}(\boldsymbol{u}I)^2 \tag{3.1}$$

$$\mu_t = \rho C_\mu \frac{k^2}{\epsilon} \tag{3.2}$$

$$\nu = \frac{\mu}{\rho} \tag{3.3}$$

$$\epsilon = \frac{C_\mu k^2}{\nu \frac{\mu_t}{\mu}} \tag{3.4}$$

$$\omega = \frac{\epsilon}{C_\mu k} \tag{3.5}$$

Table 3.4: Numerical settings for the smooth bed OpenFOAM model

Patch	U	p	omega	nut	k
Inlet	fixedValue (0.16 0 0)	zeroGradient	fixedValue uniform 8.139	calculated uniform 0.01	fixedValue uniform $9.26 \cdot 10^{-5}$
Outlet	zeroGradient	fixedvalue uniform 0	zeroGradient	calculated uniform $1 \cdot 10^{-15}$	zeroGradient
bottom	noSlip	zeroGradient	omegaWallFunction uniform 0	nutkRoughWallFunction k_s = 0.002	calculated uniform $1 \cdot 10^{-15}$
watersurface	slip	zeroGradient	zeroGradient	calculated uniform $1 \cdot 10^{-15}$	zeroGradient
weir	noSlip	zeroGradient	omegaWallFunction	calculated uniform $1 \cdot 10^{-15}$	fixedValue uniform $1 \cdot 10^{-15}$

In Figure 3.11 and Figure 3.12 a visualised output of the model is shown. These figures are for visual reference. The model calculations are finished when the model is converged.

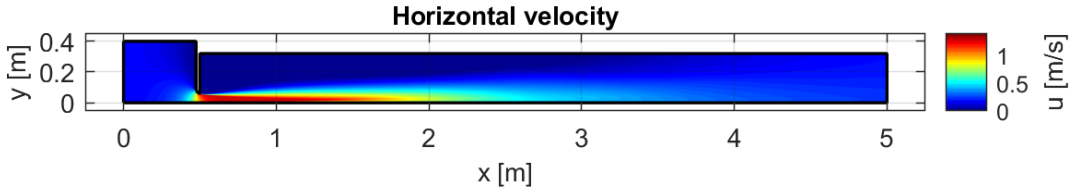

Figure 3.11: Horizontal velocity, u_x, for the smooth bed

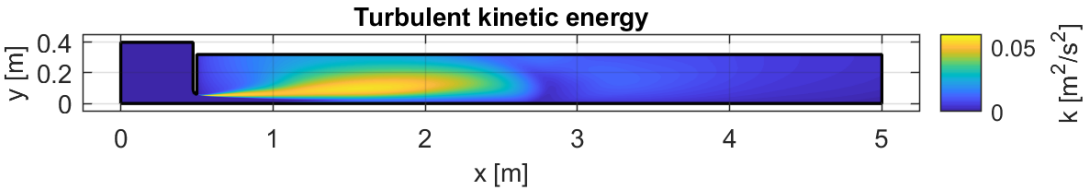

Figure 3.12: Turbulent kinetic energy, k, for the smooth bed

3.2.3. Validation outcome

Validation of the model has been performed on the horizontal velocity and turbulent kinetic energy values over a distance of 1.25m downstream of the gate. These distances are based on PIV measurement length of Deltares (2020). Through conversion of the turbulent kinetic energy, a comparison with the Reynolds stresses is done as well.

First the overview figures for u, k and R are provided for multiple distances downstream of the gate. Next an overview of the same variables at x = 1.00 m in the domain is presented. After the figures, the comparison on the variables is made. The conversion of k towards R is provided in the comparison on Reynolds stress below.

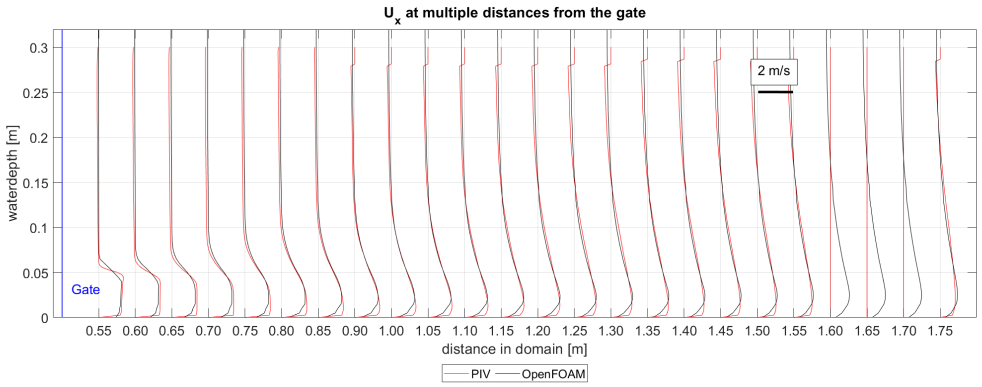

Figure 3.13: Comparison between PIV and OpenFOAM on horizontal velocity u_x [m/s] for gate height b_0 = 0.06m

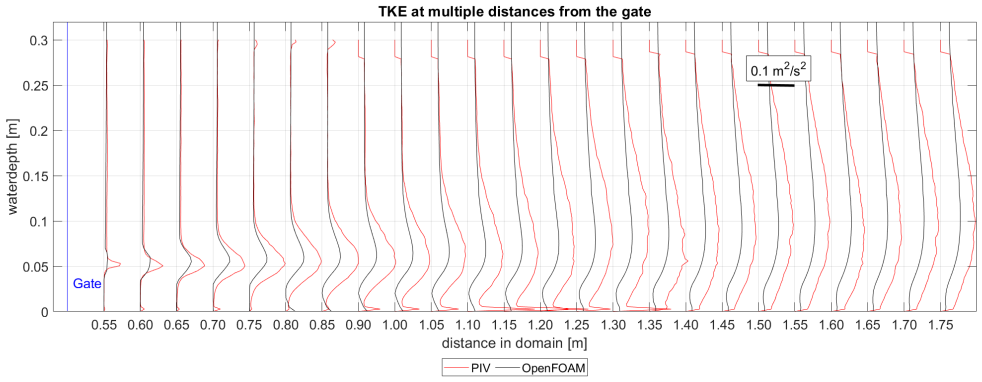

Figure 3.14: Comparison between PIV and OpenFOAM on TKE [m^2/s^2] for gate height b_0 = 0.06m

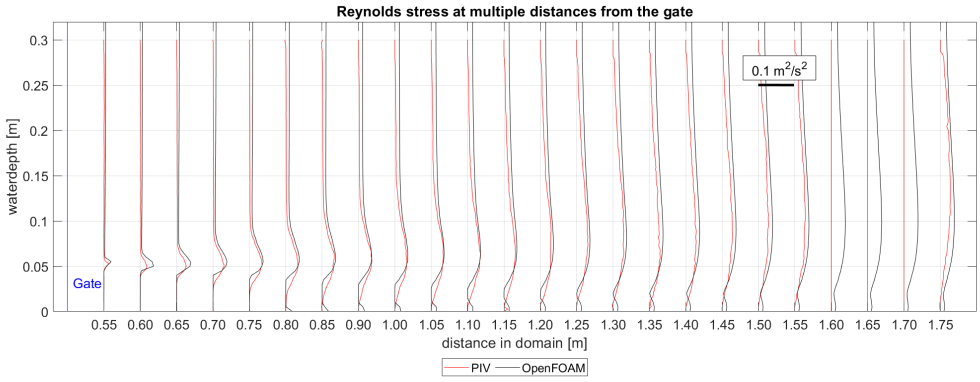

Figure 3.15: Result of conversion of k towards R with Equation 3.12

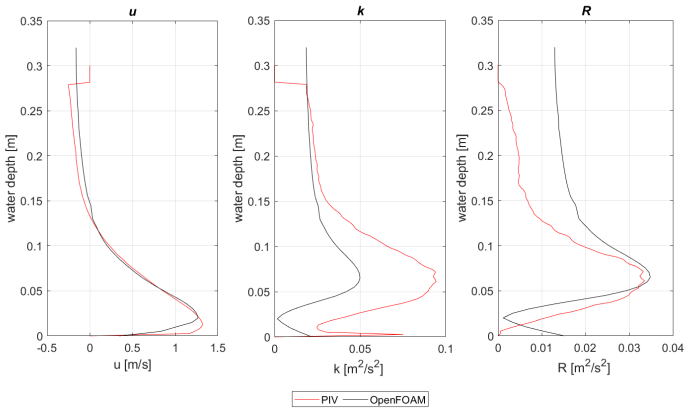

Figure 3.16: Overview of u, k and R at x = 1.00 m in the domain

Comparison on horizontal velocity

Figure 3.13 shows that the numerical model predicts the measured horizontal velocities well. The profiles are similar and only small differences occur within the range of 5 to 10% in the largest part of the water column. Near the bottom a difference can be found in the velocity, as well as higher up in the water column. In both locations the difference has outliers up to 50% difference. Higher up in the water column, the OpenFOAM model underestimates the velocity.

According to the plots, it is expected that further downstream of the gate, the velocity will be modelled correctly as well. The concept of applying a roughness value of k_s equal to 0.002 meter results in the sufficiently accurate values of the velocity and the correct modelling of the near wall field. In Chapter 5 a further evaluation will be made on the application of different roughness values, linked to applicable stone sizes.

Comparison on turbulent kinetic energy

The turbulent kinetic energy (TKE) shows less good comparison than the horizontal velocity. The modelled TKE shows an under-estimation and has a larger, less smooth, gradient. Next to this the TKE is modelled as zero in the jet, while in the PIV data at that region some turbulence occurs.

At the bottom it can be seen that the modelled smooth wall produces some turbulence, which is as expected. This roughness can not be found at every PIV measurement location, because measuring this near the bottom is hard. Another difference is the spreading of the TKE over the depth. It can be seen that the PIV data shows a more rapid spreading of TKE over the depth compared to the numerical model. As the jet region decreases, the spreading of TKE in the model increases as well.

The differences in the turbulent area is in the order of 50%, not often but sometimes reaching up to 90% in the jet region. It is expected that further downstream of the jet region, both TKE profiles will match again, but a definitive error for that region can not be determined.

Comparison on Reynolds stress
The OpenFOAM model does not model the Reynolds stresses explicitly, as the Reynolds Averaged Navier-Stokes approach is applied. With the help of a turbulence closure model the turbulence is modelled as turbulent kinetic energy. With the following equations and approximations, the turbulent kinetic energy is converted into fluctuating velocities. This gives an approximation with an error, as Figure 3.14 shows. Here Equation 3.10 originates from Nezu (2005) and Equation 3.11 from Hoan (2008).

$$k = \frac{3}{2}(\boldsymbol{u}I)^2 \tag{3.6}$$

$$I = \frac{\boldsymbol{u'}}{\boldsymbol{u}} \tag{3.7}$$

$$\boldsymbol{u} = \sqrt{u^2 + v^2 + w^2} \tag{3.8}$$

$$k = \frac{1}{2}((u')^2 + (v')^2 + (w')^2) \tag{3.9}$$

$$w' \approx u'/1.82 \tag{3.10}$$

$$v' \approx u'/1.9 \tag{3.11}$$

In these equations, k is the turbulent kinetic energy, $\boldsymbol{u}$ is the combined velocity vector of u, v and w, of which the velocity fluctuations are indicated with an accent (u' etc.). I is the turbulence intensity and the applied coordinate system can be found in Figure 1.4. The conversion applies the same equations as provided in Section 2.1.3, where only Equation 3.10 and Equation 3.11 have been added.

The combination of the above equations lead to the approximation of the total velocity fluctuations as Equation 3.12 and with this approximation at Equation 3.10 and Equation 3.11, an approximation for the Reynolds stresses is made. Higher up in the water column it can be seen that the Reynolds stresses are overestimated this way, while near the bottom the approach fits well.

$$\boldsymbol{u'} = \sqrt{1.2667k} \tag{3.12}$$

Conclusions on validation on the smooth bed
A conclusion can be drawn after the comparison of both the velocity and TKE profiles for the smooth bed. The numerical model works well with representing the shapes of the velocity, while it lacks some precision in the TKE and Reynolds stresses. The differences found in TKE are in line with the expected difference of approximately 50%.

These differences are less relevant when the computation time is taken into account as well. The computation time for this simulation took 8 hours on 10 computer cores. Compared to a 3D simulation as in Nikolaidou (2019) (30 days for 180 seconds output on 40 computer cores), this is a huge improvement . This short calculation time benefits the amount of simulations one can do, which in the end might increase the accuracy. In the end a balance must be found between calculation time, number of simulations and accuracy.

When larger roughness values are used to model a bed protection instead of a smooth surface, the computation time will decrease. The reason for this is that the center of the first cell has to increase with an increase of roughness. Larger cells mean less computation time.

The overall conclusion is that the model can be used to estimate the velocity, while for the turbulent kinetic energy a multiplication of two is proposed as solution for the 50% error in the determination of k. Despite giving a slightly different pattern for the turbulent kinetic energy, the results are still promising and sufficiently accurate to continue.

3.3. OpenFOAM model with rough bed

Next to the smooth bed, a validation of the rough bed is done by comparing the OpenFOAM output with the output of the physical tests of Jongeling et al. (2003). The measurements near the bottom are missing in the physical test data, but is modelled in the OpenFOAM model. For the OpenFOAM models, the same modelling approach as Steenstra (2014) has been used. The original plots of Jongeling et al. (2003) can be found in Appendix D.

Just as for the smooth bed, an analysis on the depth averaged Froude number is done. It is found that the maximum Froude number for case 6 is 0.2744 and for case 7 is 0.081. This means that the Froude values are below the threshold of 0.30 and this allows the use of the rigid-lid approach.

3.3.1. Geometry

The setup for the blockMesh file of case 6 and 7 can be found in Table 3.5. For both models the domain has been extended up to 5 meters, just as for the smooth bed. The cell size is determined the same way as for the smooth bed validation and is based on the roughness that Jongeling et al. (2003) had applied in his measurements.

Table 3.5: Mesh characteristics case 6 & case 7

Variable	Case 6	Case 7
Cell height bottom	0.0060 m	0.0060 m
Cell height top	0.0066 m	0.0066 m
Cell-to-cell expansion ratio	1.001	1.001
Total expansion ratio	1.1	1.1
dx	0.005 m	0.005 m
N_x	0.01 m	0.01 m
N_z	40	80
k_s	0.0124 m	0.0124 m

3.3.2. Numerical settings

Just as for the smooth bed, Equation 3.1 to Equation 3.5 has been used to compute the initial conditions. The numerical settings and boundary conditions are furthermore the same as in Table 3.4, except for the values provided below in Table 3.6. The water depths are different as well, but are already described in Section 3.1.2.

Table 3.6: Numerical settings for the OpenFOAM model of case 6 and 7

	Inlet U	Inlet Omega	Inlet nut	Inlet k	k_s
Case 6	(0.3172 0 0)	51.671	0.01	0.000516	0.0124
Case 7	(0.1572 0 0)	9.267	0.01	0.000093	0.0124

3.3.3. Validation outcome

Below, Figure 3.17 to Figure 3.22 show the comparison between the modelled situation in OpenFOAM and the measured values in the physical tests of Jongeling et al. (2003). Four figures (Figure 3.17, Figure 3.18, Figure 3.20 and Figure 3.21) provide overview plots of multiple locations downstream of the gate. Figure 3.19 and Figure 3.22 provide plots of u and k at x = 0.95 m in the domain.

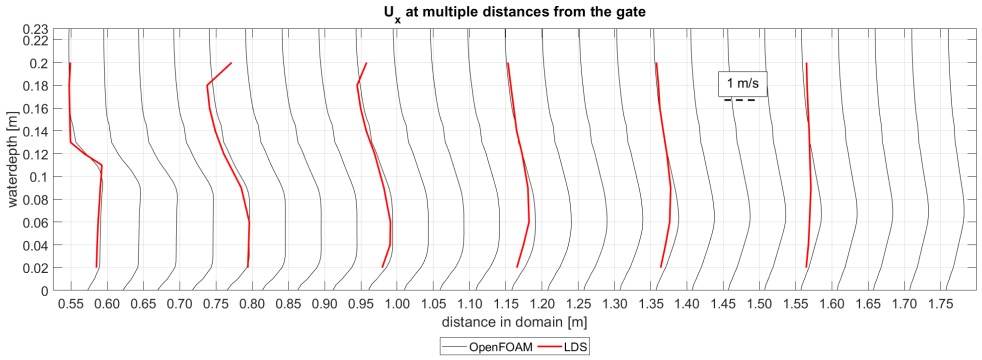

Figure 3.17: Comparison of the horizontal velocity profiles of case 6 of Jongeling et al. (2003) with the OpenFOAM output

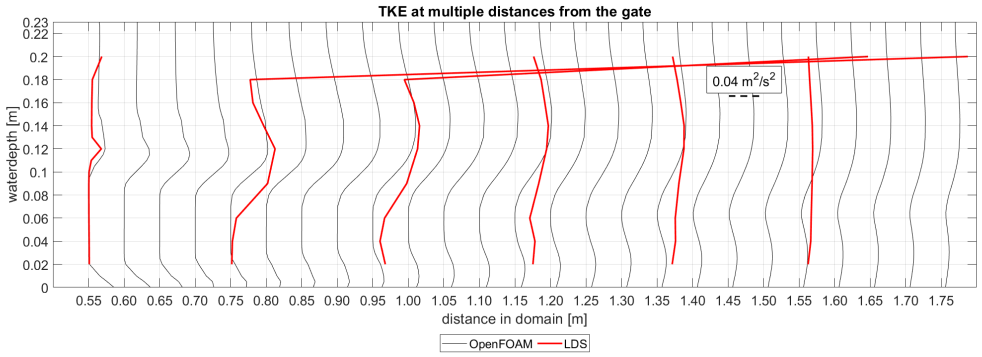

Figure 3.18: Comparison of the turbulent kinetic energy profiles of case 6 of Jongeling et al. (2003) data with the OpenFOAM output

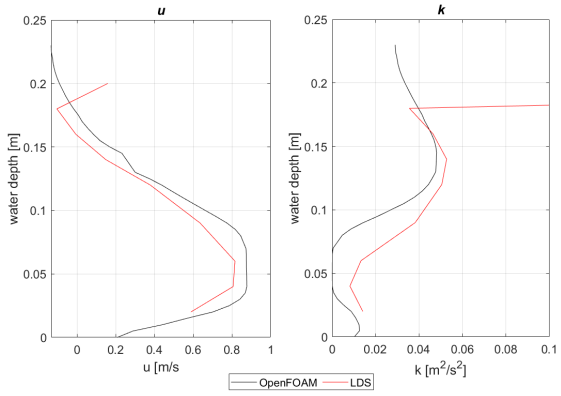

Figure 3.19: Overview of u and k at x = 0.95 m in the domain of case 6 of Jongeling et al. (2003)

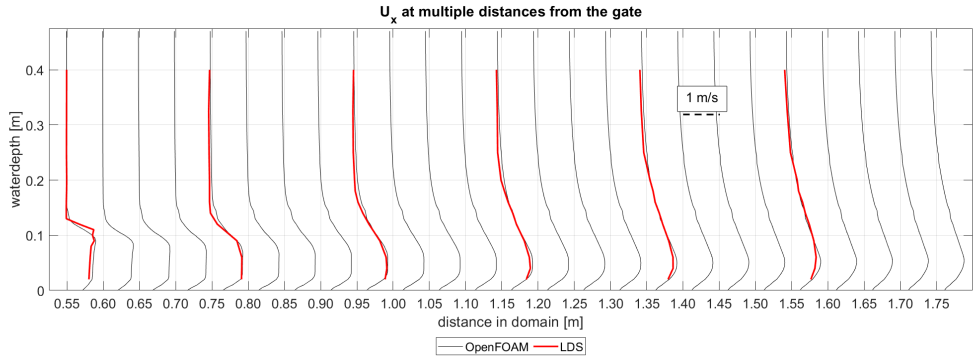

Figure 3.20: Comparison of the horizontal velocity profiles of case 7 of Jongeling et al. (2003) data with the OpenFOAM output

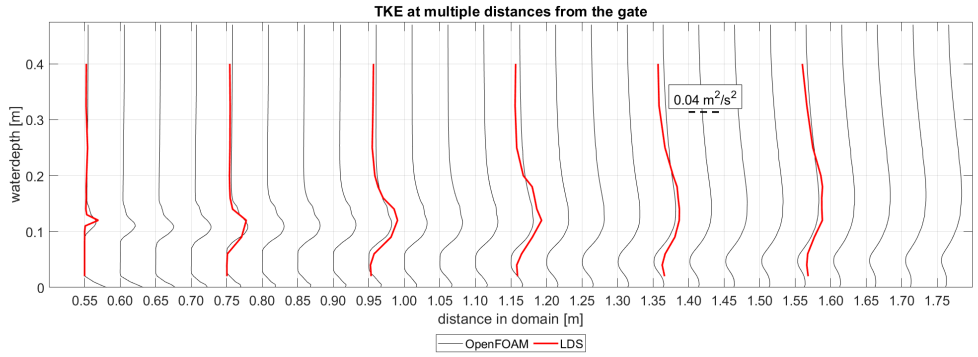

Figure 3.21: Comparison of the turbulent kinetic energy profiles of case 7 of Jongeling et al. (2003) data with the OpenFOAM output

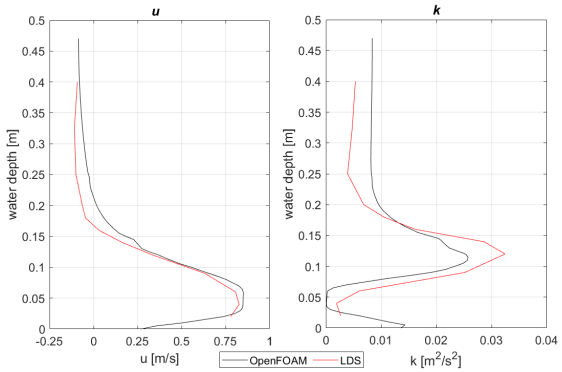

Figure 3.22: Overview of u and k at x = 0.95 m in the domain of case 7 of Jongeling et al. (2003)

The figures show that just as for the smooth bed, the horizontal velocity is modelled well with differences in the range of 5 to 10% as well. This holds for both case 6 and case 7 of Jongeling et al. (2003). An overestimation of the velocity in the lower part of the water column is seen, whereas higher up there is an underestimation. This is the same as for the smooth bed case. The difference is an acceptable difference and no compensation is required for this difference in the design process.

The turbulent kinetic energy shows a large difference between modelled and measured data for case 6 (Figure 3.18) of Jongeling et al. (2003). For case 7 (Figure 3.21) the modelled turbulent kinetic energy

compares better. On average the difference is approximately 30% with outliers up to 50% or even 90%. The fact that a difference would occur is expected, but the decrease in difference compared to the smooth bed is unexpected.

The turbulent kinetic energy plots show that for a larger water depth to gate height ratio, the turbulent kinetic energy seems to be modelled better than with a smaller water depth to gate height ratio. For case 6, this is $0.23/0.15 = 1.53$, while for case 7 this is $0.475/0.15 = 3.17$. This difference and this ratio is interesting for further physical testing.

The near bed response is not monitored by Jongeling et al. (2003), meaning that a comparison on that aspect cannot be made. The same holds for comparison near the water surface. The PIV measurements of Deltares (2020) show that it is possible to measure close to the water surface and the bed. For that reason it is advised to continue working with PIV measurements instead of LDS measurements.

For the smooth bed it is proposed to compensate for the turbulent kinetic energy. If this is applied to the rough models as well, an over estimation of the TKE is created. This would lead to additional instability, but to a more conservative design as well. The advice remains to compensate for the TKE, while knowing that in this way the turbulence is over estimated.

As design of the bed protection has a roughness between very smooth and rough, it is advised to use a compensation of 2. This compensates for the situation when largest compensation is needed and thus is conservative. This benefits the design and the compensation will be applied to the other OpenFOAM models with a rough bed as well.

3.4. Overall conclusion on validation

Three validation cases have been investigated. The first case is the smooth bed model, which is based on measurements from Deltares (2020). The second and third are based on measurements by Jongeling et al. (2003), in which roughness has been taken into account.

The velocity patterns are modelled well for both the smooth and rough bed. The differences between measurements and model are in the range of 5 to 10% and are acceptable.

It was expected that a difference of 50% would be found when comparing the turbulent kinetic energy, just as in the validation study of Steenstra (2014). For the smooth bed case this hold for approximately all measurement locations. For the rough bed, the average difference is smaller, in the range of 30%.

Next to this, as there are two water levels for the rough cases, a difference is noticed between the 0.23 m water depth (case 6) and 0.475 m water depth (case 7). It is found that the comparison between k improved for larger water depths. A potential explanation for this can be in the difference in water depth to gate height ratio and thus less influence of the jet on the water column above the jet. Next to this, the velocity in case 6 is much larger than for case 7. The discharge is approximately the same. This velocity difference can be of influence as well.

All in all it is concluded that the velocity output of an OpenFOAM 2D RANS model can be applied for stability computations, without compensation. The turbulent kinetic energy k needs a compensation, which is advised to be a factor 2. For the smooth bed this is sufficient, while for the rough bed this leads to an over estimation of k. For now it is expected that in the design process this is not an issue, as it leads to a conservative design. The reduced calculation time due to the simplifications is very attractive, but definitely leads to inaccuracies.

4

Turbulence mixing length

The mixing length is an important aspects in the determination of stone stability. In Section 4.1 different mixing length approaches are introduced, whereas in Section 4.2 comparison is made between the different approaches by computing the mixing lengths in multiple water columns downstream of the gate. In Section 4.3 a computation towards stability parameters is done.

4.1. Mixing length approaches

Three different mixing length approaches are presented in this section. These are the Bakhmetev distribution, which is used in both the stability relations of Hofland (2005) and Steenstra (2014), the shear stress relation (SSR), as applied by Ye (2017), and a method based on the turbulence closure model, the closure model approach (CMA).

4.1.1. Bakhmetev distribution

The Bakhmetev distribution is a distribution based on fully developed flow and is coupled to the von Karmann constant. The distribution is based on the largest possible eddy that can occur. Additional information is found in Section 2.3. The mixing length according to the Bakhmetev distribution is indicated as L_m. For convenience, the Bakhmetev distribution equation is repeated below.

$$L_m = \kappa h \gamma \sqrt{1-\gamma} \tag{4.1}$$

As guidance for the Bakhmetev distribution, the case of Deltares (2020) with gate height b_0 = 0.06 m and water depth downstream of the gate of h = 0.32 m is used. The mixing length distribution according to the Bakhmetev distribution for this case is plotted in Figure 4.1. This figure shows a maximum mixing length L_m, at $2/3^{th}$ of the (dimensionless) water depth z/h.

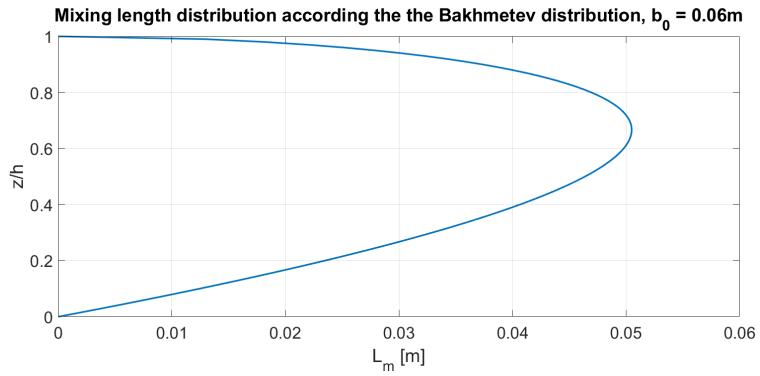

Figure 4.1: Mixing length distribution according to the Bakhmetev distribution for a water depth of 0.32 m and gate opening b_0 of 0.06 m.

This distribution shows a maximum value for the influence of the turbulence and velocity near the bed when scaled with its location in the water column (Figure 4.2), meaning that velocity and turbulence near the bed have a larger influence than higher up in the water column.

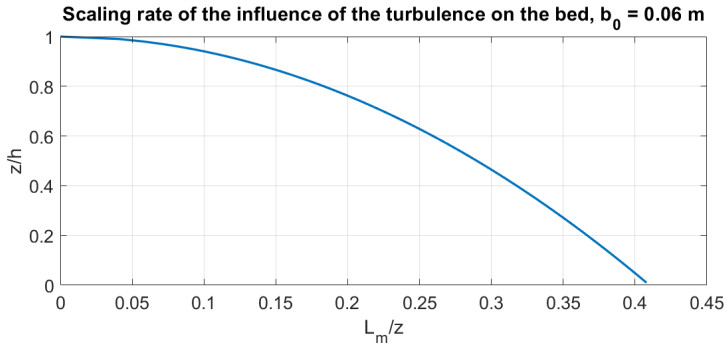

Figure 4.2: Scaling rate of the influence of the turbulence on the bed for a water depth of 0.32 m and gate opening b_0 of 0.06 m.

4.1.2. Shear Stress Relation (SSR)

The approach of Ye (2017) differs from the application of a distribution for the determination of the mixing length. In his approach Equation 4.2 was applied, which is based on the relation for the mixing length concept and eddy viscosity as defined in Equation 2.27.

$$l_{SSR} = \sqrt{\frac{\nu \frac{du}{dz} - \overline{u'w'}}{\left|\frac{du}{dz}\right| \frac{du}{dz}}} \tag{4.2}$$

Where the mixing length l_{SSR} is computed according to the kinematic viscosity ν, velocity gradient du/dz and Reynolds stress $\overline{u'w'}$. The calculations were performed on measurements and not on a numerical model.

Ye (2017) found that for a non-submerged underflow gate the mixing length of turbulence grows towards the Bakhmetev distribution, but close to the gate this distribution does not hold. His measurements did not reach far enough to find exactly at which point the Bakhmetev distribution was found again.

The method of Ye (2017) can be applied to the physical tests dataset of Deltares (2020) as well. As these setups are modelled in OpenFOAM, there can be made a good comparison between physical output and numerical output. Next to this it might show insight in whether a different approach for the mixing length can be used.

4.1.3. Closure Model Approach (CMA)

The applied turbulence closure model is the $k-\omega$ SST model. Based on the units of k and ω, being $[m^2/s^2]$ and $[1/s]$ respectively, the idea came forward to seek for a relation. This relation found its origin in a conversation with Bas Hofland (from Hofland (2005)), is called the closure model approach (CMA) and is defined as follows:

$$l_{CMA} = \frac{\sqrt{k}}{\omega} \tag{4.3}$$

This is a new approach and is taken into account in the upcoming sections as well. No additional research information is given for this and the formulation is only based on units.

4.2. Comparison of methods for the underflow gate

In total four different mixing length calculations are done. These are based on the PIV data and the SSR, OpenFOAM and SSR, OpenFOAM and CMA and lastly the Bakhmetev distribution. An overview of the different mixing length calculations for the case of Deltares (2020) with gate opening b_0 of 0.06 m at x = 0.85 m in the domain is provided in Figure 4.3

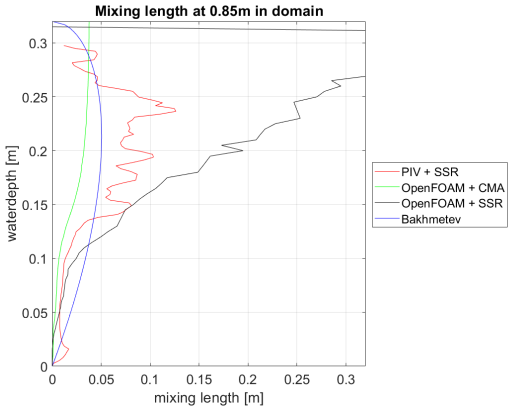

Figure 4.3: Mixing length at x = 0.85 m in the domain

An overview plot of the mixing lengths downstream of the gate is provided in Figure 4.4. This overview shows a gradual decrease of mixing length, further away from the gate.

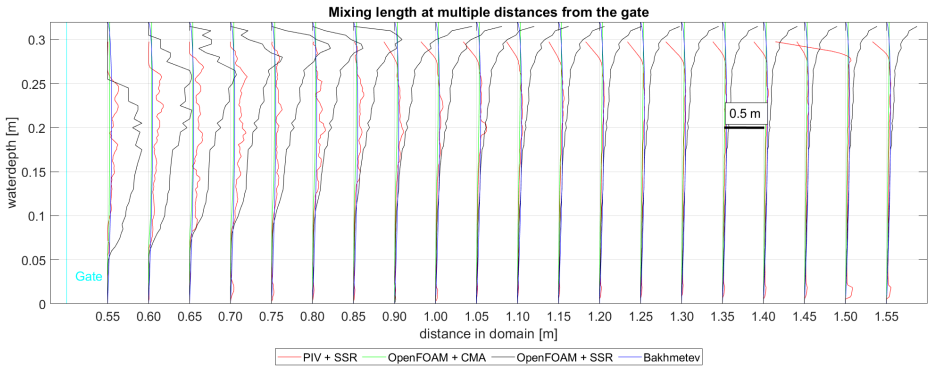

Figure 4.4: Mixing length distribution at different locations downstream of the gate for different approaches

In the jet region near the bottom (0 to 0.06 m), the mixing length is small as velocity fluctuations in the jet region are small. Higher up in the water column, the velocity fluctuations are larger, thus larger mixing lengths occur.

Further downstream from the gate the mixing length approaches have a more comparable outcome. It is expected that eventually downstream of the gate the mixing length from all methods will become the same as the Bakhmetev distribution, as this distribution is based on fully developed flow situations with a logarithmic profile.

Figure 4.3 shows the mixing lengths in more detail with a maximum range in the horizontal axis of 0.32m. This value is chosen this way, as the mixing lengths cannot be larger than the water depth as the eddies are based on moving particles in the water column.

A main difference between the methods is that the CMA and Bakhmetev approach show a smooth curve compared to the SSR. For the Bakhmetev distribution this is expected, as it is a fixed length based on geometry. In the CMA the mixing length higher up in the water column is larger than in the lower area. This is expected as well as this is the region with the submerged hydraulic jump and thus the region with largest eddies.

Both the PIV and OpenFOAM data, combined with the SSR, show an increased mixing length value higher up in the water column as well. The OpenFOAM Reynolds stresses higher up in the water column, that are converted from the turbulent kinetic energy k, show larger values than the PIV data.

Next to this, small values are present in the velocity gradient of the OpenFOAM output, while for the PIV measurements this is larger. This combination leads to the larger values for the mixing length for the OpenFOAM with SSR values.

Their pattern is less gradual, indicating that the computations are based on local values that vary more. As it would be ideal to work with local parameters, the SSR method has a larger interest. In Chapter 5 stability curves are created, showing the differences of the local parameters compared to the geometry based Bakhmetev distribution.

4.2.1. Adaptation for the SSR

An adaptation for the OpenFOAM + SSR output is proposed, as the mixing length tends to result in too large values. This is done by setting a physical limit on the distribution, as done in Figure 4.5. This figure shows as well that this measure is not needed for the PIV + SSR method, as the mixing length stays within bounds. This raises the idea that for high fidelity numerical models this boundary is not needed, but that is out of the scope for this research.

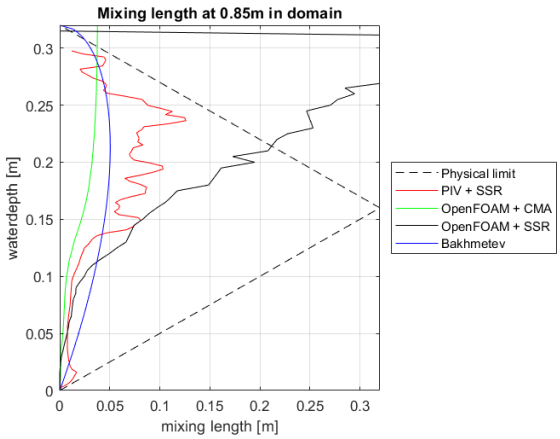

Figure 4.5: Indication of the physical limit of the mixing length

The advantage of physical limit is that still the local parameters can be used as done in the SSR, while also having a physical limit, just as in the Bakhmetev distribution. This also reduces the error of the obtained Reynolds stress values higher up in the water column through OpenFOAM.

Next to this physical limit, the other adaptation is to plot a polynomial through the data points, with fixed points of no mixing length at the bottom (z = 0 m) and at the water surface (z = water depth). This reduces the amount of wiggles and creates a smooth curve, which fits the stability computations well. Mostly a third order polynomial fits the data set.

The benefit of this combined approach is that a workable solution for the SSR mixing length is created. Without the limit, the mixing length higher up in the water column would grow too large, leading to unrealistic values. The polynomial creates a smooth curve, which benefits the outcome and allows to take the mixing lengths near the bottom into account. In this way it allows to work past the imaginary values for the mixing length near the bottom. The adaptation helps in the application of a simplified model in the design of bed protections.

Figure 4.6 shows an example of a polynomial plot through the mixing length computed with SSR and with a physical limit applied. The adaptation of the SSR with physical limit and polynomial is used for further computations with the SSR approach.

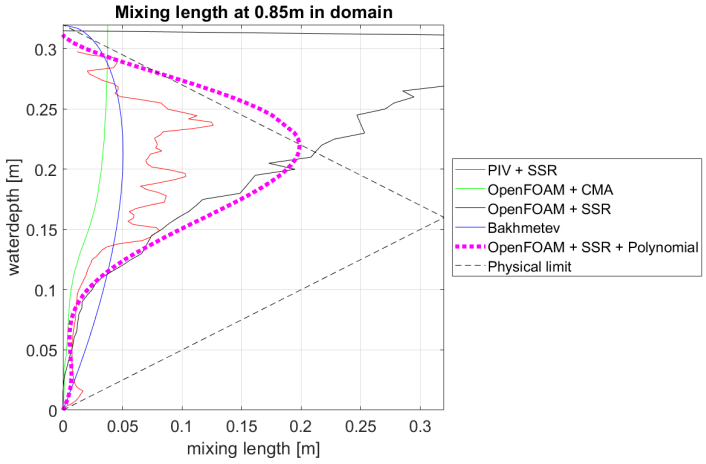

Figure 4.6: Indication of the polynomial plot of the mixing length with SSR at 0.85 m in the domain

Further downstream this physical limit is of less use, as the computed mixing lengths do not cross the physical limit. This is shown in Figure 4.7. It is thus mainly a measure for the mixing lengths nearby the gate.

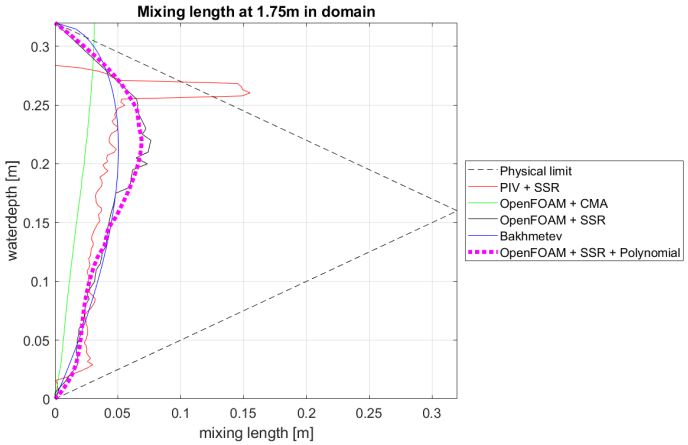

Figure 4.7: Indication of the polynomial plot of the mixing length with SSR at 1.75 m in the domain

4.3. Stability parameter for different mixing length approaches

Concluding the section regarding the mixing length, for all mixing length approaches a stability calculation has been done with the Steenstra stability parameter (Equation 2.22).

The computations are done with an input stone size of d_{n50} = 0.001 m, leading to a value for the Nikuradse roughness of k_s = 0.002 m. This value is not comparable with a stone grading, but represents a smooth bed. This allowed the comparison with the PIV measurements of Deltares (2020), as these measurements are based on a smooth bed. The outcome is presented below in Table 4.1, in which ψ_{RS} is the Steenstra stability parameter and z_{max} is the point in the water column where the maximum drag force is computed.

It is interesting to compute the values with stone gradings applied at the bottom, but the flow situations change when roughness of the bottom changes. This means that the outcome cannot be compared with the smooth bed case of Deltares (2020).

Table 4.1: Computation of stability parameters based on the different mixing length methods

	Location in the domain					
	0.8 m		1.1 m		1.4 m	
Mixing length method	ψ_{RS} [-]	z_{max} [m]	ψ_{RS} [-]	z_{max} [m]	ψ_{RS} [-]	z_{max} [m]
PIV + SSR	30	0.02	20	0.03	29	0.04
OpenFOAM + CMA	0.6	0.01	1.3	0.005	1.8	0.005
OpenFOAM + SSR	145	0.03	35	0.02	23	0.02
Bakhmetev + OpenFOAM	30	0.04	27.6	0.04	27	0.03

As the whole water column is used to compute these values, one thing immediately stands out. The jet at the bottom, and its high velocities, influences the drag velocity that much, that the turbulence in the hydraulic jump is not the largest influence on stone stability. The values of the largest spatial average of velocity and turbulent kinetic energy are all found in the jet region near the bottom, as indicated by z_{max}.

The location of maximum drag term highlights the importance of the polynomial, as because of the polynomial, a mixing length near the bottom is taken into account (see Figure 4.6). This makes the difference between the PIV and OpenFOAM data higher up in the water column of less interest. This difference higher up is the difference in Reynolds Stress output.

Next to this, almost all the computed ψ_{RS} values are out of the range of applicability of the Steenstra equation. This means that it is not correct to use these values to say something definitive about the stone stability for this fictive stone size for a smooth bed. It is expected that this would occur, as a smooth bed is modelled and it is not expected that this smooth bed, with reference nominal diameter of 0.001 meter, could resist such flow velocities. This does not mean that the method is incorrect.

The CMA method has stability values that are in range with the Steenstra equation. This is strange as the modelled stone size is so small, that damage should occur. It is thus not correct that the model outcome is seen as stable. As this happens at all locations in Table 4.1 for the CMA, it is expected that this method is not providing the correct output and will thus be further neglected.

The next step is the application of larger stones, thus a larger values for k_s. This is worked out in Chapter 5.

5

Riprap modelling

Chapter 5 starts with the detailed research approach, which can be understand after reading Chapter 2 to Chapter 4. Next to this, in this section the OpenFOAM output is converted to stability values. Two values for the roughness have been applied, one based on the research of Steenstra (2014), and one based on the application of quarry rock 10-60kg. A conclusion is drawn on the application of the Steenstra equation for both applications, which is based on the link between stone damage curves of Jongeling et al. (2003) and ψ-curves computed with the Steenstra equation.

5.1. Overview of approach

All the information provided up till this part of the report can be added into the simplified approach as provided in Chapter 1 Figure 1.3. This leads to the detailed overview, Figure 5.1, below.

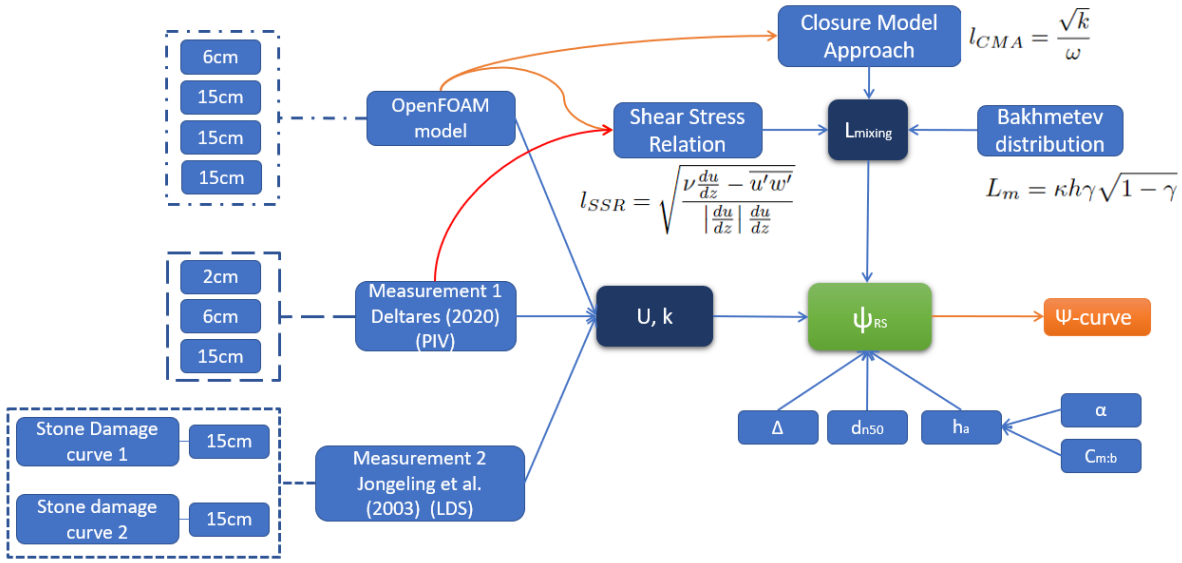

Figure 5.1: Overview of the approach for this thesis

This figure can be read in several steps, which are enumerated below here.

1. Reading Figure 5.1 starts below the green box containing ψ_{RS}. Here the values for the relative density Δ and the stone size d_{n50} have to be determined. Next to this, based on the gate opening, the height in the water column h_a, where the measurement for the acceleration must be taken, must be determined with corresponding amplification factor α and value for combined mass and bulk coefficient $C_{m;b}$.

2. Additional input is required for the stability parameter ψ_{RS}, which consists of the streamwise velocity u and turbulent kinetic energy k. For validation, these values can be obtained from two measurements, which are 1) PIV measurements (Deltares, 2020) and 2) LDS measurements (Jongeling et al., 2003). These measurements combined provide five different gates.
3. The third option for input for u and k is the OpenFOAM output. Four models are created for this, as the gate with gate opening of 0.02m leads to an unstable model. The OpenFOAM models resemble with measurement 1 and 2.
4. The last essential input for ψ_{RS} consists of the mixing length L_{mixing}. For this value, three options are investigated, being the Shear Stress Relation (SSR), Closure Model Approach (CMA) and Bakhmetev distribution.
5. Both the OpenFOAM model and PIV measurements can be used to determine values for the SSR. Only the OpenFOAM model can be used to determine values for the CMA. The reason for this is that the CMA is based on the applied closure model.
6. Now all the input is known for the computations of ψ_{RS}. When this computation is done for multiple distances downstream of the gate, a ψ-curve (see orange box) can be created.
7. The ψ-curves that are created out of the OpenFOAM models that compare with measurement 2 (i.e. measurements of Jongeling et al. (2003)), can be compared to the stone damage curves of measurement 2. These are curves based on measurement stone movement and can be related to the ψ-curves, based on OpenFOAM output.

5.2. Overview of OpenFOAM cases

As mentioned before, the bed protection is parameterized with the nutkRoughWallFunction. This allows for the application of the Nikuradse roughness on the bottom. This roughness can be linked to a nominal diameter, d_{n50}, via $k_s = d_{n50}$ to $3d_{n50}$. In this application a value of $2d_{n50}$ is used.

As different values of k_s lead to different bottom cell heights, it is chosen to apply the roughness value for the whole bed, just as done in the research of Jongeling et al. (2003). This simplifies the approach and makes it possible to bypass the effect transitional areas between grid elements. In addition, a smooth bed contains very small grid sizes near the bed, increasing the computation time. At last, it allows the comparison with the Jongeling et al. (2003) data, as in that research a completely covered bed was investigated.

The modelled stone size 10-60 kg is based on scaling between a river depth and model depth. It is assumed that the model has a depth 20 times smaller than a river, which let to the conversion of d_{n50} of 0.23 m to 0.0115 m for grading 10-60 kg. The stone size of Jongeling et al. (2003) would then compare with rock grading 90/180 mm.

In total five cases are modelled with varying flow situations and stone dimensions. To be extra clear on which curve represent what, Table 5.1 is provided with this essential information. In Table 5.2 an overview on these cases can be found and in blue an important aspect of each case is highlighted, which differs them from eachother. Only for the OpenFOAM models with roughness a ψ-curve has been made, as for the smooth bed no damage could be measured. The actual damage in the stone damage curves of Jongeling et al. (2003) was measured by stone counting, allowing a comparison with the ψ-curves.

Table 5.1: Difference in curves denotation

ψ-curves	Curves based on the Steenstra equation
Stone damage curves	Curves based on stone damage measurements of Jongeling

The ψ-curves are compared to a threshold of motion for ψ_{RS}, equal to 1.2. This is based on the determined entrainment rate that represents start of motion, being 10^{-8}.

Table 5.2: Overview worked out cases for thesis with the main aspect of each case highlighted in orange

Case	Origin	Gate height	Roughness	Elaboration
Case 1	PIV Deltares	0.06m	0.0124m	The 0.06m gate is the model used for almost all examples in this thesis. The smooth version is used for validation and for the ψ-curves in this section a model is created with roughness value equal to the research of Jongeling et al. (2003).
Case 2	PIV Deltares	0.06m	0.023m	This is the model with increased roughness. It is used to see whether increased roughness has effect on the stability.
Case 3	PIV Deltares	0.15m	0.0124m	This is another option from the PIV data set, allowing the comparison for a 0.15m gate opening as well. Modelled with the same roughness as for the Jongeling et al. (2003) cases.
Case 4	Jongeling	0.15m	0.0124m	This case refers to case 6 of Jongeling et al. (2003). As it is a replica of scale tests, it allows for the comparison of stone damage curves and ψ-curves. Here h = 0.23m.
Case 5	Jongeling	0.15m	0.0124m	This is the replica of case 7 of Jongeling et al. (2003) and can also be used for comparison of the ψ-curve with the stone damage curve of the Jongeling et al. (2003) report. Here h = 0.475m.

5.3. Curve comparison case 4 and 5

The first comparison is made for case 4 and 5, as these cases can be compared with stone damage data of Jongeling et al. (2003). The comparison with these cases allows the comparison between actual measured stone damage and modelled stone damage. This is done through stone damage curves, measured in Jongeling et al. (2003) and ψ-curves, computed with the Steenstra stability equation (Equation 2.22).

In Table 5.3 an overview of the case characteristics, including cell dimensions, is given. It can be seen that the main difference is in water level, velocity and number of cells in vertical direction. The mesh characteristics have already been introduced in Section 3.3.

Table 5.3: Characteristics Case 4 and 5

Variable	Unit	Case 4	Case 5
Velocity	m/s	0.40	0.18
Gate opening, b_0	m	0.15	0.15
Upstream water depth, h_1	m	0.25	0.50
Downstream water depth, h_2	m	0.23	0.475
Cell height bottom	m	0.006	0.006
Cell height top	m	0.0066	0.0066
Cell-to-cell expansion ratio	-	1.001	1.001
Total expansion ratio	-	1.1	1.1
dx	m	0.01	0.01
N_x	-	500	500
N_z	-	40	80
k_s	m	0.0124	0.0124

5.3.1. Case 4

A stability calculation has been performed with the Steenstra equation. This is done for multiple distances downstream of the gate. The ψ-curve for the Bakhmetev distribution can be found in Figure 5.2 and for the SSR method in Figure 5.3. The curves can be compared to the actual damage curve, which can be found in Figure 2.11.

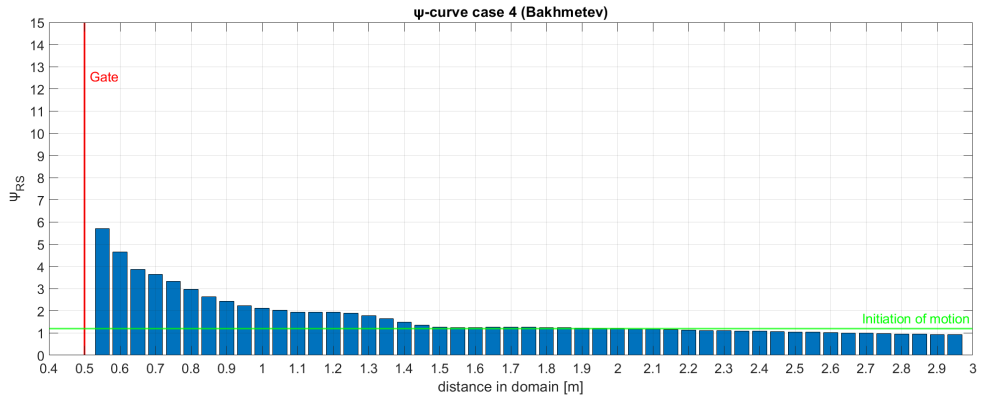

Figure 5.2: ψ-curve of case 4 based on OpenFOAM output with the Bakhmetev distribution

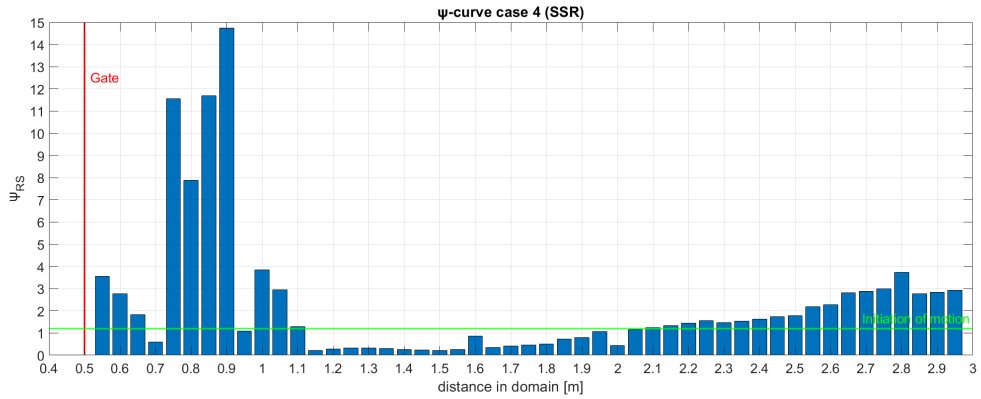

Figure 5.3: ψ-curve of case 4 based on OpenFOAM output with the SSR method

The Bakhmetev distribution ψ-curve shows a smooth pattern that decreases in stability number ψ_{RS} at location further downstream of the gate. At 2.1 meter in the domain, ψ_{RS} passes the threshold and the bed is computed as stable. In the stone damage curve (Figure 2.11) the stones do not move anymore past 1.7 meter, which differs from the Bakhmetev results.

Next to this, Figure 5.2 shows a very gradual pattern with a small bump between 1.1m and 1.5 meter. This bump compares with the bump of Figure 2.11, but is much smaller and not of the same level as the ψ_{RS} value near the gate. This might indicate an underestimation of the stability number in this area.

The SSR shows a less gradual pattern which compares more to Figure 2.11 than the Bakhmetev distribution of Figure 5.2. Especially the two peaks near the gate are represented well, with a decrease in stability number (thus a more stable bed) between the peaks. Only the length of the peak area does not compare, as in the ψ-curve the bed is computed stable at 1.1m, while in the Jongeling et al. (2003) tests this was after 1.7m.

Further downstream, after 2.0 meter, the threshold of motion is exceeded again. A possible explanation for this can lay in the changed velocity pattern and thus velocity gradient. Previously it was already mentioned that small values of du/dz have a large influence on the outcome of the mixing

length. Further downstream of the gate, the influence of the jet on the velocity pattern has decreased. Here the velocity grows towards a logarithmic velocity profile, where the velocity gradient higher up in the water columns are close to zero.

This allows for much larger mixing lengths than closer to the gate, leading to larger eddies and apparently to a larger stability number and thus instability. As this instability was not measured by Jongeling et al. (2003), the current approach for the region further away from the gate does not seem to hold and the Bakhmetev approach is a more reasonable approach. This idea of larger SSR mixing lengths, l_{SSR}, is supported by Table 5.4, where the values for L_m, l_{SSR} and their locations in the water column z_{max} is presented.

Table 5.4: Comparison of mixing length (L_m and L_{SSR}) and location of the mixing length in the water column (z_{max}) that leads to the maximum drag force on the bed at 2.85m in the domain

	x = 2.85m
Bakhmetev	z_{max} = 0.03 m L_m = 0.012 m
SSR	z_{max} = 0.057 m L_{SSR} = 0.09 m

5.3.2. Case 5

The ψ-curve for the Bakhmetev distribution can be found in Figure 5.4 and for the SSR method in Figure 5.5. The curves can be compared to the actual damage curve, which can be found in Figure 2.12.

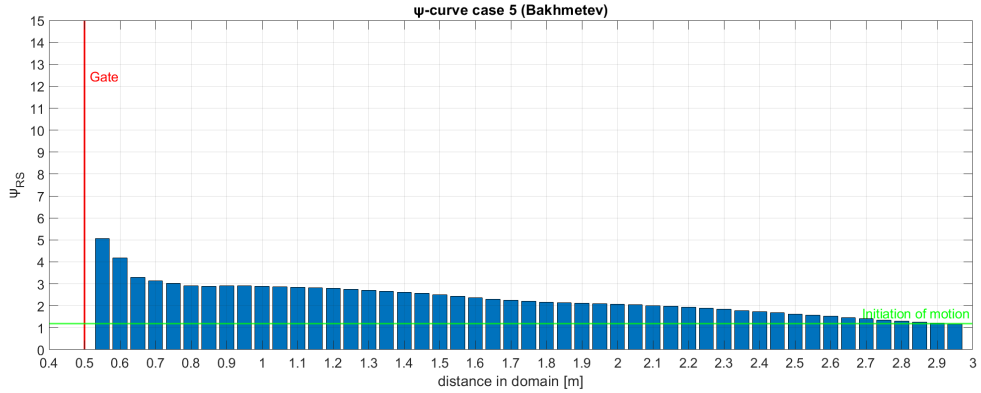

Figure 5.4: ψ-curve of case 5 based on OpenFOAM output with the Bakhmetev distribution

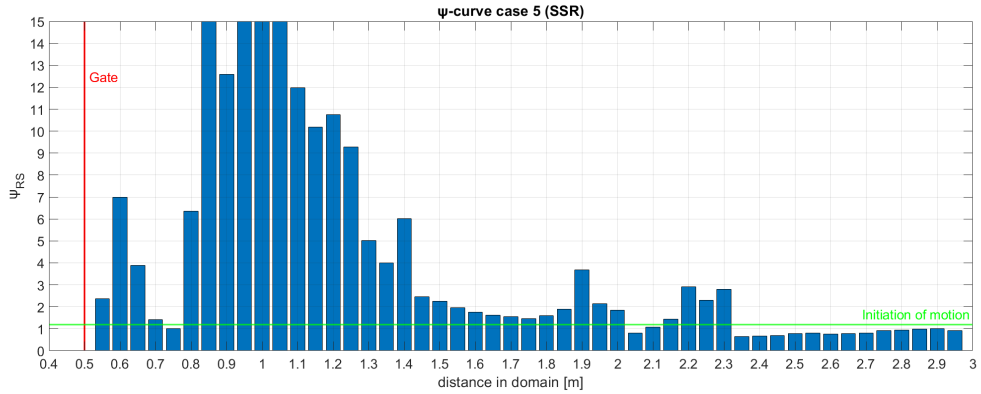

Figure 5.5: ψ-curve of case 5 based on OpenFOAM output with the SSR method

Just as for case 4, the Bakhmetev curve shows a gradual decrease. Again the further away from the

gate, the lower the stability number. The location where the value of ψ_{RS} crosses the initiation of motion line, 3m, does also not compare to the measured location in the stone damage curve, which is 2.5m.

The SSR ψ-curve shows very interesting comparison to the damage curve of Figure 2.12. Both the pattern and location of damage have a similarity and in the end no movement in measured. This is in contrary with what was found in case 4, where the stability number increased again towards the end of measurements. All in all is case 5 very interesting, as it shows good comparison. The shape of this curve leads to the expectation that damage can be assessed with numerical modelling.

Drag and acceleration term
For the ψ-curves of case 5, additional curves are made to show the effect of the different terms in the Steenstra equation. Figure 5.6 shows this for the Bakhmetev distribution and Figure 5.7 for the SSR method. What can be seen is the clear distinction between accelerating en decelerating flow and its influence on the stability parameter.

In the accelerating part, the acceleration has a negative influence on the stone stability and in the beginning governs the stone movement. After approximately 0.4m the velocity is approximately constant and shows no acceleration. In this area, the influence of the drag term is governing. At 1.3m the flow start to decelerate, leading to a stabilising force on the bed and a decrease in stability number. Despite that, the drag term due to velocity u and turbulent kinetic energy k is still large enough to pass the stability threshold.

The acceleration term contributes to a more efficient design, as it increases the stability of the stones. Without this force taken into account, the bed would be modelled as unstable for a larger length downstream of the gate. It thus contributes to an improved approach towards the actual measured damage and instability.

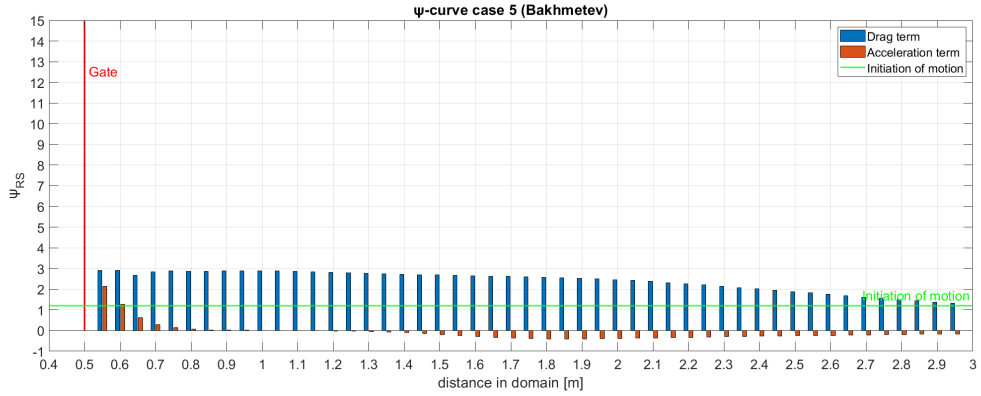

Figure 5.6: ψ-curve of case 5 based on OpenFOAM output with the Bakhmetev distribution with drag and acceleration term splitted

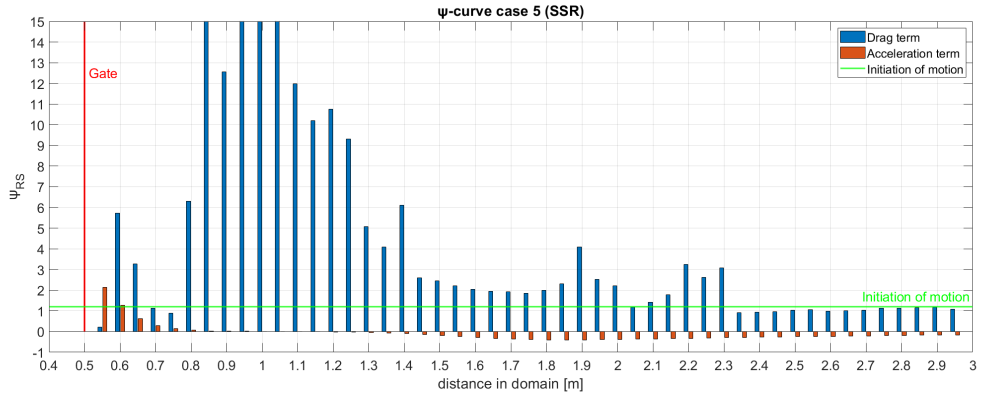

Figure 5.7: ψ-curve of case 5 based on OpenFOAM output with the SSR method with drag and acceleration term splitted

5.3.3. Final remarks case 4 and 5

What comes forward from the Bakhmetev and SSR approach is that the SSR shows the best comparison to the peak pattern as measured by Jongeling et al. (2003). It clearly shows a peak due to acceleration in the beginning, after which turbulence induces the second peak. Especially case 5 shows really good comparison to the actual measured damage.

The application of the Bakhmetev distribution can be interesting when an estimation needs to be made until where a bed protection is stable. It does not show local patterns but gives an indication of stability. For case 4 the absolute error is 0.4 meter and for case 5 this is 0.5 meter.

The Bakhmetev distribution is more practical than the SSR, so it can be understandable to in the end choose for this method compared to the SSR. The SSR shows more promising results in a more precise determination of the damage and eventually a more adapted design. For that reason the advice for future research is to dive deeper into the SSR approach and the effect further downstream, based on PIV measurements and numerical output.

5.4. Curve comparison case 1 and 2

The second comparison is between case 1 and 2. These ψ-curves have been made without a reference case, but still can provide input for comparison. Here the stone diameter has been changed, resulting in k_s equal to 0.0124m for case 1 and equal to 0.023m for case 2.

In Table 5.5 an overview of the case characteristics, including cell dimensions, is given. It can be seen that the main difference is the bed roughness, leading to a different grid size.

Table 5.5: Characteristics Case 1 and 2

Variable	Unit	Case 1	Case 2
Velocity	m/s	0.16	0.16
Gate opening, b_0	m	0.06	0.06
Upstream water depth, h_1	m	0.40	0.40
Downstream water depth, h_2	m	0.32	0.32
Cell height bottom	m	0.006	0.0089
Cell height top	m	0.0066	0.0098
Cell-to-cell expansion ratio	-	1.002	1.002
Total expansion ratio	-	1.1	1.1
dx	m	0.01	0.01
N_x	-	500	500
N_z	-	64	43
k_s	m	0.0124	0.023

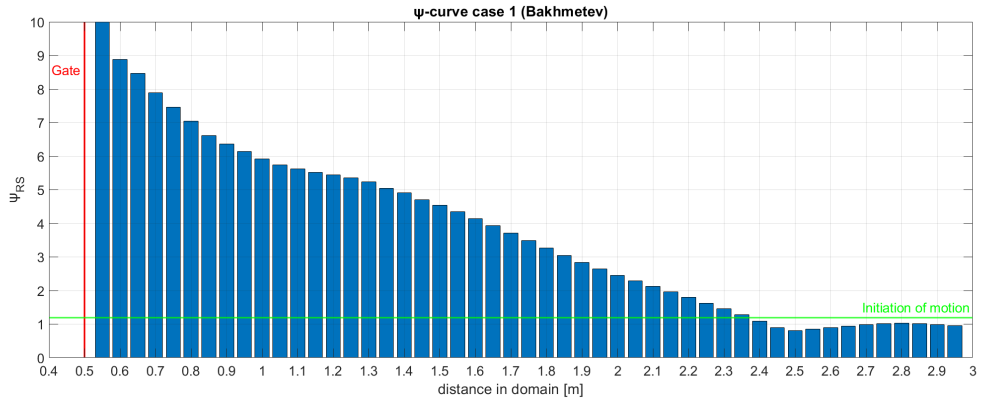

Figure 5.8: ψ-curve of case 1 based on OpenFOAM output with the Bakhmetev distribution

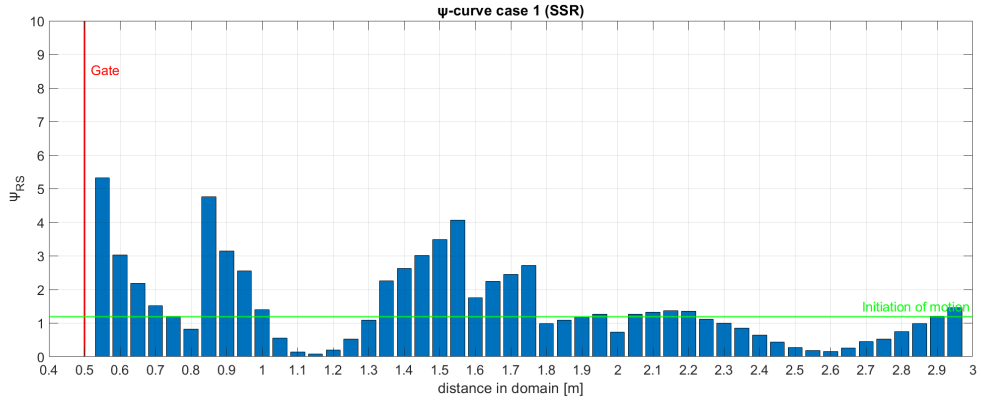

Figure 5.9: ψ-curve of case 1 based on OpenFOAM output with the SSR method

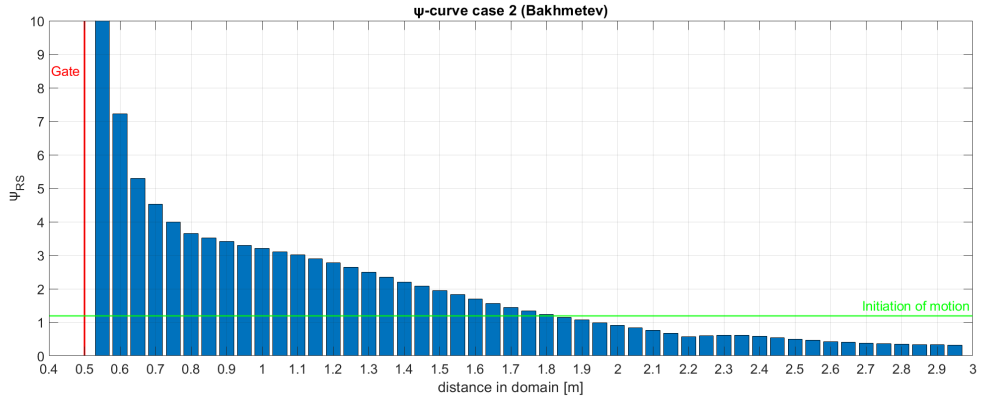

Figure 5.10: ψ-curve of case 2 based on OpenFOAM output with the Bakhmetev distribution and increased roughness compared to case 1

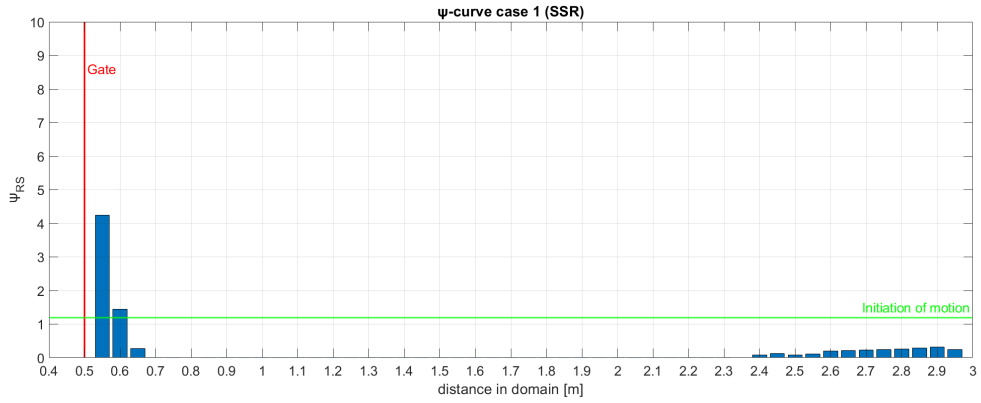

Figure 5.11: ψ-curve of case 2 based on OpenFOAM output with the SSR method with increased roughness

The main thing that is shown with the figures Figure 5.8 to Figure 5.11 is the influence of an increased roughness on the ψ-curve outcome.

Just a previous curves, the Bakhmetev distribution shows a gradual decrease. After increasing the roughness to k_s equal to 0.023m, it is still estimated that the bed is unstable up to 1.8 meter in the domain. With k_s equal to 0.0124 the bed is determined unstable up to 2.4m in the domain. Thus the increased roughness does have an influence on the bed stability further downstream of the gate, but the complete bed is not found stable.

For the SSR approach, the change in bed roughness leads to an almost completely stable bed protection. As can be seen in Figure 5.11, only near the gate, in the area with the largest flow velocities, the bed is determined as unstable.

As additional comparison, the mixing lengths and location of the mixing length in the water column (z_{max}) that leads to the maximum drag force on the bed at 0.85m in the domain are provided in Table 5.6. At this location the bed is determined as unstable for both mixing lengths for k_s equal to 0.0124, while for k_s equal to 0.023 the Bakhmetev approach determines the bed as unstable. The SSR approach determines the bed as stable for this roughness.

Table 5.6: Comparison of mixing length (L_m and L_{SSR}) and location of the mixing length in the water column (z_{max}) that leads to the maximum drag force on the bed at 0.85m in the domain

x = 0.85m	**Case 1**	**Case 2**
Bakhmetev	z_{max} = 0.045 m L_m = 0.0181 m	z_{max} = 0.02 m L_m = 0.00845 m
SSR	z_{max} = 0.01 m L_{SSR} = 0.00367 m	z_{max} = 0.01 m L_{SSR} = 0.00176 m

When the roughness is increased, the Reynolds stresses near the bottom increases, as well as the turbulent kinetic energy. This leads to the situation where the forces near the bed have a larger influence than higher up, indicating the difference between z_{max} of case 1 and 2 of the Bakhmetev approach. This reduced height also leads to a smaller applied mixing length, as it is based on the Bakhmetev distribution with a fixed shape based on geometry.

As the Reynolds stress increases, the mixing length computed with the SSR method decreases. For this reason the calculated mixing length L_{SSR} decreases between case 1 and 2. For case 2, the decrease in mixing length still means that the largest influence of the drag forces remains at the same location z_{max}.

The decrease in mixing length for the SSR approach lead to the increased stability (or reduced stability parameter ψ_{RS}). This shows that local parameters are of large influence to the final outcome of a

stability calculation. Apparently for the Bakhmetev approach the increased turbulent kinetic energy and Reynolds stress did not lead to a large reduction in stability parameter, as it is not taken into account in its mixing length.

The difference between the outcomes of the Bakhmetev and SSR approach are very interesting, as this gives a large second difference between the approaches. First of all the pattern is different, while now it is shown that the Bakhmetev approach handles an increased rough bed differently compared to the SSR approach.

An additional research with an underflow gate in a flume with two different stone sizes, for example comparable to the stones used for this models, is advised. This can give essential output on which mixing length approach results in the correct estimation of the damage.

5.5. Case 3

The final presented curve is of case 3. This case has a gate height of 0.15m and a bit different flow situation than the gates of Jongeling et al. (2003). Just as previously shown, the Bakhmetev distribution shows a gradual decrease. The SSR approach shows the same patterns as previously seen, but here the turbulent region is more spread. As no comparable material is available, these figures only extra underline the difference between the Bakhmetev approach and SSR.

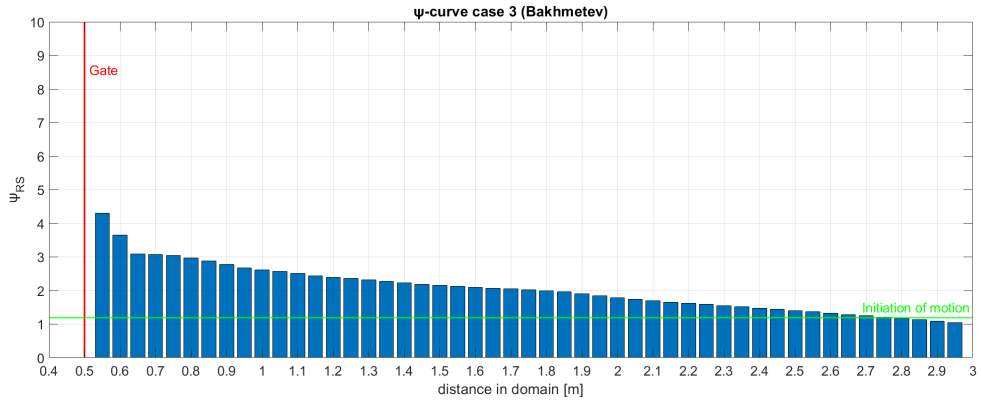

Figure 5.12: ψ-curve of case 3 based on OpenFOAM output with the Bakhmetev distribution

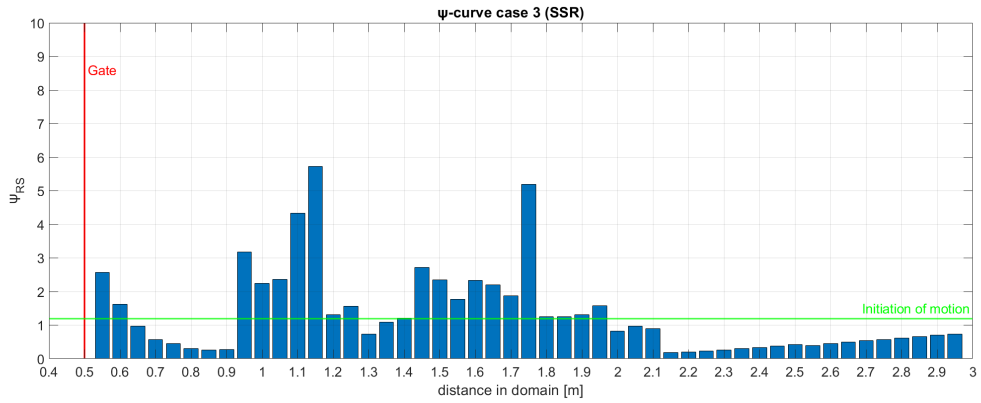

Figure 5.13: ψ-curve of case 3 based on OpenFOAM output with the SSR method

5.6. Tipping point

Both approaches indicate a location in the domain after which the stones are determined to be stable, called a tipping point. This location is based on the threshold of motion criteria, being $\psi = 1.2$. A

comparison between the Bakhmetev and SSR approach is interesting for design purposes and tipping point values are provided in Table 5.7. For case 4 and 5 the actual measured tipping point is provided as well.

Table 5.7: Tipping point location in the domain

	Case 1	Case 2	Case 3	Case 4	Case 5
Physical measurement	-	-	-	1.7 m	2.5 m
Bakhmetev	2.4 m	1.85 m	2.8 m	2.1 m	3 m
SSR	2.2 m	0.65 m	2.0 m	1.1 m	2.35 m

The outcome of this analysis shows that the Bakhmetev approach is more conservative than the SSR approach. In all cases the location of the tipping point is further downstream for the Bakhmetev approach. The best comparison for this can be made with Case 5, as this case has the best reference to actual damage measured by Jongeling et al. (2003). Case 1 to 3 has no comparison to damage but shows that still the Bakhmetev approach is more conservative.

5.7. Conclusions on the curves

The Bakhmetev distribution creates a gradual decrease in stability number the further away from the gate, without showing local peaks in the ψ-curves. Because of this, it is not clear at which area there is more damage compared to other areas. The distribution shows a point downstream of the gate where the initiation of motion threshold is passed, but this does not compare with the measured damage of Jongeling et al. (2003). Despite that it can still be used to give an indication up to where the stones are not stable, leading to a more conservative design than with the SSR method.

The SSR produces ψ-curves that have similarities with actual measured damage. Especially case 5 shows very good similarities on both the peaks and the distance from the gate up to where stones displace. More research is needed with the SSR near the underflow gates, before a definitive conclusion can be given on the application of this method for all (underflow) weir situations. Especially the difference between increased roughness for the SSR and Bakhmetev is interesting to investigate.

Concluding, the best outcome so far is the similarity between Figure 2.12 and Figure 5.5. This similarity gives good hope for further research. To show their agreement, the figures have been combined into one figure (Figure 5.14), in which the vertical axis has been shifted towards the initiation of motion line. The left vertical axis present the calculated stability number ψ_{RS} based on the OpenFOAM output, and the right vertical axis present the number of moved stones, which are directly copied from Figure 5.5.

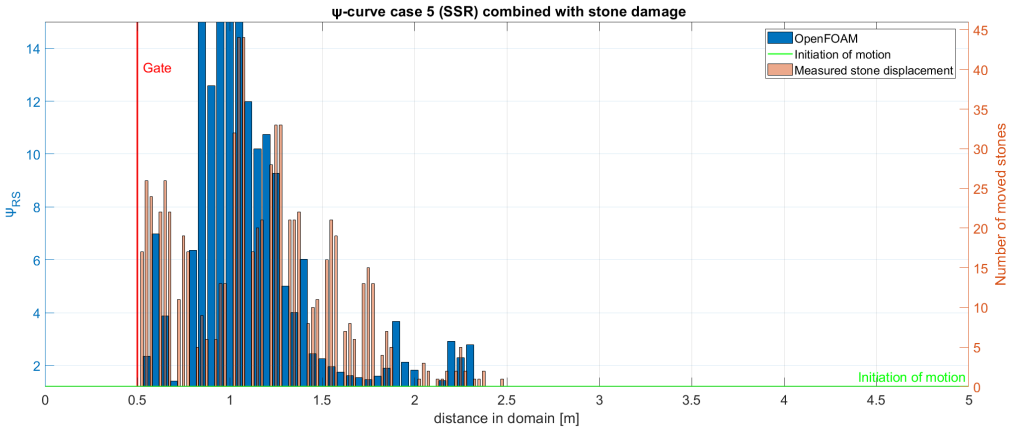

Figure 5.14: ψ-curve case 5 based on OpenFOAM combined with the number of moved stones from Jongeling et al. (2003) case 7.

6 Discussion

The main finding in this thesis is that the adapted approach for the mixing length (l_{SSR}) in the Steenstra (2014) equation improves the computed stability number for stone stability downstream of underflow weirs. This leads to an improved comparison between stone damage curves and ψ-curves. This combination results in a design approach for riprap bed protection downstream of underflow weirs.

This design approach contributes to the further development of the application of CFD modelling in OpenFOAM in the design process of bed protections downstream of underflow weirs. It is an addition to previously performed physical model tests and determined stability relations, while maintaining acceptable computation times for engineering applications.

6.1. Main discussion topics

Two main points are of special interest in this discussion, being the SSR mixing length (l_{SSR}) and the physical testing data. These two points are the basis for the next step in the development of CFD modelling for bed protections downstream of weirs and other river structures.

6.1.1. SSR mixing length

The SSR mixing length computations are very sensitive to input from the numerical model. At locations where du/dz is small, the mixing length tends to go to very large numbers. Near the bottom, imaginary numbers are computed due to positive Reynolds stresses $\overline{u'w'}$ and positive velocity gradients du/dz. To create a workable solution for these two, the decision was made to set geometrical limits on the equation and by fitting a polynomial through the acquired data points. This leads to a workable mixing length distribution near the gate, based on the maximum possible mixing length.

In relation to the meaning of the mixing length, it is physically not possible to have values that are larger than the water depth. With that in mind, and the computed values, a polynomial can be plotted through the data points. This polynomial is user sensitive and not generally applicable. The user can investigate the best fit, using expert judgement on the expected curves and computed data points.

It is advised to work on a general approach for these polynomials. With only the currently available data this general approach could not be developed. Physical testing in a structured manner can improve the understanding and should be performed as described in Section 6.1.2.

High fidelity numerical simulations can as well be used to improve the mixing length concept. This is only advised for the mixing length and not for the bed damage, as the design method cannot be improved by only high fidelity simulations. The outcome of the simulations must be linked to a damage profile in order to gain progress in the design of riprap bed protections downstream of underflow weirs through CFD modelling. Figure 4.5 already shows that the physical limit and polynomial are not needed for the PIV measurements. When high fidelity measurements results in more accurate results, this limit probably would not be needed.

6.1.2. Physical testing

The damage curves of Jongeling et al. (2003) only show the total amount of stones moved, without in detail information regarding stone sizes. Next to this, only one gate height has been investigated, with two water level combinations for up- and downstream. The validation data of Deltares (2020) consists of detailed measurement, without the application of a stone grading on the bed and thus no measured damage. With this PIV data only the smooth model could be validated.

A combination of both data sets lead to the result of this thesis, while a structured approach on physical testing could result in improved outcomes. Throughout this thesis a clear idea arose on what measurements to perform and why. Below this is summarised.

The first aspect is on how the stone damage is measured. In Jongeling et al. (2003) two types of damage curves are provided, which are a damage curve based on the number of stones moved per stripe and the net moved stones (Out - In) per stripe. These curves lack the information of which stone sizes actually moved. The actually moved stone sizes are important for getting an improved feeling for which value of stone diameter moves and which does not.

In the current assessment of this thesis, d_{n50} is taken as input for ψ_{RS}. If detailed information was given, for example a sieve curve of the damage or a stone diameter indication of the moved stones, an improved approach could be developed. Currently a mismatch can occur where stone stability is computed with d_{n50}, while only d_{10} could have moved. The current stone damage curves are too generic to dive into this.

Next to this, the current findings are very case specific. It is essential to have a systematic approach for the setup of the physical model tests. This approach must be based on three options, being 1) the application of different stone gradings for the same gate height, 2) the application of different gate heights for the same stone size, and 3) the application of multiple water levels and discharges for both option 1) and 2).

This systematic approach will result in a data set containing detailed stone damage curves for multiple flow situations and gate heights. If this is systematically performed it is expected that a relation will come forward between water level, gate height, flow velocity and stone diameter. This leads to less case specific result and increases the potential application in engineering applications.

The described approach of three steps can as well be applied to overflow weirs. The described steps fit for this as well, while for this the gate height should be changed towards wall height. When the research for overflow weirs is included, the combination of over- and underflow adds on to the design challenge as described in Appendix A, where the future renovation plans for the Meuse river is described.

Lastly, it is advised to determine up to which distance measurements are needed in advance of physical model tests. It is proven that roughness can be modelled in OpenFOAM and a first expectation of the stability can be determined through a ψ-curve. The computation time is in the range of hours and when that output is converted, initial areas of interest can be found. For a more rapid approach, a first estimation of length downstream of the underflow weir with an unstable bed protection can be done with the Bakhmetev approach, requiring even less numerical input from the model.

6.2. Additional discussion

Besides the SSR approach and physical testing, other topics of discussion are provided below.

Simplifications are used in order to create a numerical model with small computation time. This is a benefit, but it also reduces accuracy. The main practical decision is a 2D RANS model with rigid lid for the water surface. It is known that more extensive numerical methods with 3D computations and a two-phase approach lead to more accurate results, while having a very large computation time. A good example is the thesis of Nikolaidou (2019), in which a detailed LES computation took 30 days to simulate 180 seconds, working with 40 computer cores on a cluster of Deltares. This research is

conducted on 10 computer cores on a computer of approximately €5000 and takes approximately 2 to 8 hours to simulate a converged solution.

Due to the simplification towards a 2D RANS model, the turbulent kinetic energy and thus Reynolds stresses have lower computed values than the measured values with an average difference of 50% and outliers between 30% to 90%. In this thesis the turbulent kinetic energy is compensated for by the multiplication of k by 2. This multiplication seems to be a reasonable assumption for the region of the hydraulic jump, but is not necessarily valid for the region further downstream. The PIV measurements were available for a range up to 1.25 meter downstream of the gate, not including the whole hydraulic jump. A comparison further downstream could not be made but is essential for correct compensation of k.

Next to the numerical simplifications, model simplifications are made as well. The computation was done for a bed that contains the same stone size throughout the whole domain. Changing stone sizes means changing grid sizes, as the grid is dependent on the applied roughness value k_s. This leads to transitional areas between the grids. The influence of this grid transition is undefined and limits the application of a bed with multiple stone sizes. After every change in stone size, the flow situation changes and for a complete assessment of a bed this step is important.

In addition to the application of the same stone size over the whole bed, it is noted that in a prototype weir design, the area nearby the gate has a concrete bottom protection. If this bottom layer should be taken into account, the grid cell dimensions near that area need to be very small, in the order of 0.0001m, just as for the smooth bed validation. This creates another transition, highlighting the importance for a good understanding of these transitions.

6.3. Relevance

The proposed design method for the application of numerical output in the design of riprap bed protection downstream of underflow weirs contributes to the extended applications of CFD models. Physical testing currently is the basis for all designs, while there is a transition happening towards using only CFD models. This goal is far from being reached without solid and reliable physical data.

This thesis contributes to this transition as it shows that with a simplified model, outcomes comparable to physical measured damage come forward. With the ψ-curves it is shown that physically measured damage patterns are comparable to the stability patterns based on numerical output. This thesis provides a basis for which physical testing data is needed for further development of CFD for design of riprap bed protections downstream of underflow weirs. The structured testing approach of Section 6.1.2 is a description of this basis. The relevance is thus found in the definition of the next steps for CFD modelling, bed protections and the validation on the damage patterns. Eventually after enough physical modelling, numerical modelling can take over.

Certainly with the upcoming replacement task for weirs in the Meuse river (Appendix A), the need for CFD modelling raises. When the CFD methods continue to grow while maintaining agreement with physical measurements, it will eventually be applied for this renovation task. Performing physical tests for all weir types still remains expensive thus the interest in these numerical modelling researches will remain large.

In addition the relevance is found in the limited computation time. This makes this method interesting for companies to use, while extensive numerical methods are not. Eventually an approach can only be used when it is an addition to the user, instead of a limitation. With respect to the extensive numerical methods, the method of this thesis certainly is an addition for the user in the design process of underflow weirs.

A disclaimer must be added, as this model was validated for certain flow conditions. This means that it is questionable if the applicability outside of the configurations is correct. The proposed structured physical modelling procedure contributes to the applicability, showing the importance of reliable

physical models as well.

6.4. Application in design

Interesting to discuss is at which moment in the design phase the proposed design method can be applied and what the best approach for the mixing length is. This contributes to the understanding of when to apply the numerical output, as used in this thesis.

In Section 5.6 the tipping point is introduced. This is the location downstream of the gate where the bed changes from unstable to stable. A comparison on this point is made for both approaches, with reference to the measured damage of Jongeling et al. (2003) for case 4 and 5. This shows that the Bakhmetev approach is a conservative approach, as it estimates the unstable region downstream of the gate to be larger than actually measured.

The SSR has the potential to provide a detailed vision on the bed stability, but it is not developed enough to apply it in that way yet. The structured testing approach as described in Section 6.1.2 must be performed first. Eventually this approach can lead to a more sustainable and tailored design, but for now the Bakhmetev approach is advised.

The Bakhmetev approach for the mixing length can be used after the initial design. With this method the first design is conservative and defines the area of tipping point of stability. Here an iteration step with different roughness values can be applied. After the tipping point, the area of interest can be defined. This is the basis for physical testing and measuring afterwards. After the physical tests, the measured bed damage can be compared to the expected damage from the numerical model. This outcome can be compared to a SSR computation to contribute to the further development of that approach.

Applying the Bakhmetev approach without physical measurements afterwards is not advised yet, as the influence of an increased or reduced bed roughness is not compared with physical measurements yet. The difference as provided in case 2 between the Bakhmetev and SSR approach for an increased roughness provides a first possible outcome for this (Figure 5.10 and Figure 5.11).

An overview of the location in the design process and when to apply the Bakhmetev approach is provided in Figure 6.1.

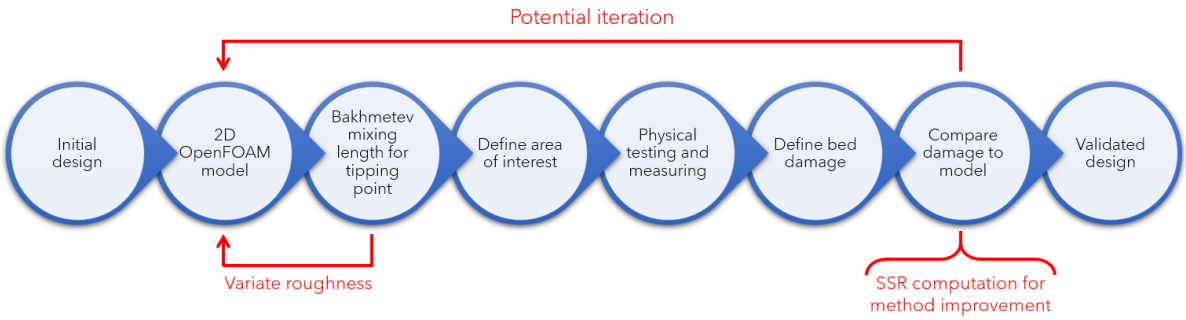

Figure 6.1: Advised application of the Bakhmetev distribution in the design process

7

Conclusion

In this chapter an answer is given on the research question and the most important conclusions based on the sub research questions are provided. First the research objectives and questions are repeated. Then, the conclusions are presented.

This thesis started with the following research objectives:

- Proposing a numerical modelling strategy to create a design method for riprap bed protections for underflow weirs.
- Creating a practical model with reduced computation time compared to full scale 3D models.

and supporting main research question:

How can CFD modelling in OpenFOAM be applied to determine stone stability for a riprap bed protection downstream of submerged underflow weirs?

The research question is answered with the help of sub research questions, which are answered before the main research question is elaborated and conclusions are provided. The sub research questions are:

1. What are the current methods and insights on the assessment of bed protection through numerical modelling?
2. What is the effect of different mixing length approaches on the stability calculations outcome?
3. What is the influence of the drag term and advective acceleration term in the stability parameter of Steenstra (2014) on the computed stability?

7.1. Answer to the sub research questions

In this part of the conclusion, the sub research questions are answered. The answers are presented with referencing to the report.

1. What are the current methods and insights on the assessment of bed protection through numerical modelling?

Multiple research on the application of numerical output for the determination of stone stability has been performed, as described in Section 2.2.1. The last research that introduced a well calibrated stability formula was Steenstra (2014), which is introduced extensively in Section 2.2.2. A stability parameter, ψ_{RS}, has been developed for multiple flow situations, while omitting the underflow gate. Steenstra (2014) shows that with ψ_{RS} a bed protection can be assessed, even with a simplified model as a 2D RANS model.

2. What is the effect of different mixing length approaches on the stability calculations outcome?

The mixing length is widely discussed in Chapter 4. Three different mixing length approaches are investigated, being the Bakhmetev distribution as applied in ψ_{RS} originally, the shear stress relation (SSR) and closure model approach (CMA). It is found that the Bakhmetev and SSR approach lead to interesting outcomes.

The ψ-curves in Chapter 5, for example Figure 5.4 and Figure 5.5, show the difference between the outcome of the Bakhmetev and SSR approach. The Bakhmetev approach leads to a gradually decreasing stability number further downstream from the gate. This approach can be used to define a tipping point of stability. It is found to be conservative in the determination of the distance downstream of the gate where this point is located, as presented in Table 5.7.

The SSR approach shows a pattern that compares to measured stone damage from the physical tests of Jongeling et al. (2003). Figure 5.5 compares well to Figure 2.12, shown well in Section 5.7. This leads to the conclusion that the SSR approach has the possibility of defining a stability pattern that resembles with the actual damage. Further testing is advised, as described in Section 6.1.2.

Increasing the roughness leads to different outcomes between the Bakhmetev and SSR approach. It is found that for the Bakhmetev approach the length downstream of the gate, where stones are computed as unstable, becomes smaller for increased roughness (Figure 5.8 and Figure 5.10). When the SSR approach is applied, the increased roughness leads to a stable bed for almost the whole domain (Figure 5.9 and Figure 5.11). The correct outcome cannot be validated, as there were no measurements available, but the difference in outcome is still interesting and a topic for further research.

3. What is the influence of the drag term and advective acceleration term in the stability parameter of Steenstra (2014) on the computed stability?

Two ψ-curves are made that show the influence of the drag and advective acceleration term on the stability number ψ_{RS}. Figure 5.6 shows this for the Bakhmetev approach and Figure 5.7 for the SSR approach. Positive values for ψ_{RS} mean a decrease in stability and negative values mean an increase in stability.

The advective acceleration term shows an decrease in stability close to the gate, induced by accelerating flow. Further downstream of the gate, the flow decelerates, leading to a stabilizing force on the bed. The influence of the advective acceleration is thus mostly important close to the gate. Further downstream the advective acceleration term contributes to a more efficient design, as the stability number decreases due to the influence of this term.

The influence of the drag term on the stability of the bed is much larger compared to the advective acceleration term. This term mainly governs the stability pattern that is found in Figure 5.5, which compares to the stone damage curves of Jongeling et al. (2003) (Figure 2.12). The large influence of the drag term underlines the need for taking the velocity and turbulent kinetic energy into account.

7.2. Main conclusions and answer to the research question

This thesis focuses on flow through an underflow weir, leading to a jet and hydraulic jump downstream of the gate. A method is formulated in which numerical output is used to compute stone stability. The stability relation derived by Steenstra (2014), ψ_{RS} (Equation 2.22), is applied and an inspection on the suitable mixing length L_{mixing} is performed. This results in a ψ-curve which contains a link with bed stability, specifically for the underflow gate.

The validation of the smooth bed demonstrates the possibility to model the flow velocities u sufficiently accurate, despite only modelling in a 2D environment. The modelled turbulent kinetic energy k reveals a mismatch of approximately 50%, which can be compensated for by the application of a factor 2 on the computed values of k. The conversion of k towards Reynolds stresses results in good comparison in the lower region of the water column, but higher up in the water column there is an overestimation of

the Reynolds stresses. The inaccuracies in outcome are compensated by the small computation time, making the 2D approach a valid method for modelling the flow properties during a preliminary design.

The rough bed validation shows a same order of magnitude difference for the computed velocity u as for the smooth bed, while the turbulent kinetic energy k has an reduced error in the region of 30% to 50%. This is less than the smooth bed, but still it is advised to compensate for k by a factor 2. This leads to a conservative design and allows the application of all types of roughness between a rough and a smooth bed. In this way it benefits the use for designers of bed protections.

The investigation on the mixing length leads to an adapted approach for the Steenstra (2014) parameter (Equation 2.22). This leads to a comparison between physically measured stone damage curves and numerical computation based ψ-curves.

The damage curves are compared with ψ-curves of the original Bakhmetev approach (L_m) for the mixing length, as well as the new SSR approach (l_{SSR}). It is found that the Bakhmetev approach does not reproduce the damage pattern accurate and can only be applied as indication for the tipping point between stable and unstable stones downstream of the gate. The SSR shows agreement on the damage pattern, as well as on the length downstream of the gate until where instability occurs. The agreement is shown in Figure 5.14.

Increasing the roughness in the model shows another difference between the Bakhmetev (L_m) and SSR (l_{SSR}) approaches. Roughness is investigated by diving into two cases with two different roughness values. Case 2 has an increased roughness compared to case 1. The Bakhmetev approach (Figure 5.10) shows that the tipping location downstream of the gate, where instability changes to stability, is closer to the gate for case 2 than for case 1 (Figure 5.8). The SSR ψ-curve (Figure 5.11) for case 2 shows a clear decrease in stability number over the whole bed downstream of the gate compared to case 1, indicating that the bed is stable at almost all locations in the domain. This difference is interesting and can be compared when two physical test with two stone sizes has been performed, including stone damage curves.

This leads to the answer to the main research questions. It is shown that the bed protection downstream of underflow gates can be assessed through CFD modelling in OpenFOAM with a simplified numerical model. The equation of Steenstra (2014), ψ_{RS} can be used in two ways. With the Bakhmetev approach, L_m, a stability tipping point can be determined, as with the SSR approach, l_{SSR}, a better representation of the instability regions is found. The numerical output of a 2D RANS model is accurate enough to perform a stability calculation. With ψ_{RS} an assessment on the bed protection can be performed through ψ-curves, indicating stability of stones downstream of the weir. Currently, the approach can be applied in the design process as indicated in Figure 6.1. After further development with the proposed physical testing approach (Section 6.1.2), numerical modelling could replace physical testing. A large benefit of the numerical method in this thesis is that the calculation time of the OpenFOAM models in the range of hours, making the method ideal for engineering applications and a good competitor to high fidelity models.

References

Andersson, A. G., Andreasson, P., & Lundström, T. S. (2013). CFD-modelling and validation of free surface flow during spilling of reservoir in down-scale model. *Engineering Applications of Computational Fluid Mechanics*, *7*(1). https://doi.org/10.1080/19942060.2013.11015461

Battjes, A. (2002). *Vloeistofmechanica*. http://repository.tudelft.nl/

Castillo Luis, G., Carrillo, J. M., & Bombardelli, F. A. (2017). Distribution of mean flow and turbulence statistics in plunge pools. *Journal of Hydroinformatics*, *19*(2). https://doi.org/10.2166/hydro.2016.044

Deltares. (2020). *CFD Validation of flow downstream of an underflow gate* (tech. rep.).

de Vries, J. W., Egelie, C. F., & Jansen, P. P. (1935). *XVIde Internationaal Scheepvaartcongres*.

El-Behery, S. M., & Hamed, M. H. (2011). A comparative study of turbulence models performance for separating flow in a planar asymmetric diffuser. *Computers and Fluids*, *44*(1). https://doi.org/10.1016/j.compfluid.2011.01.009

Ferziger, J. H., & Perić, M. (2002). *Computational Methods for Fluid Dynamics*. https://doi.org/10.1007/978-3-642-56026-2

Garcia-Alcaide, V. M., Palleja-Cabre, S., Castilla, R., Gamez-Montero, P. J., Romeu, J., Pamies, T., Amate, J., & Milan, N. (2017). Numerical study of the aerodynamics of sound sources in a bass-reflex port. *Engineering Applications of Computational Fluid Mechanics*, *11*(1). https://doi.org/10.1080/19942060.2016.1277166

Hart, J. (2016). Comparison of Turbulence Modeling Approaches to the Simulation of a Dimpled Sphere. *Procedia Engineering*, *147*. https://doi.org/10.1016/j.proeng.2016.06.191

Hoan, N. T. (2008). *Stone Stability Under Non-uniform Flow* (tech. rep.). Delft University of Technology. http://repository.tudelft.nl/.

Hofland, B. (2005). *Rock & roll: Turbulence-induced damage to granular bed protections* (tech. rep. No. 4). Delft University of Technology. Delft University of Technology. http://repository.tudelft.nl/.

Jones, W. P., & Launder, B. E. (1972). The prediction of laminarization with a two-equation model of turbulence. *International Journal of Heat and Mass Transfer*, *15*(2). https://doi.org/10.1016/0017-9310(72)90076-2

Jongeling, T. H. G., Blom, A., Jagers, H. R. A., Stolker, C., & Verheij, H. J. (2003). *Ontwerpmethodiek Granulaire Verdedigingen* (tech. rep.). WL | Delft Hydraulics.

Macián-Pérez, J. F., Bayón, A., García-Bartual, R., Amparo López-Jiménez, P., & Vallés-Morán, F. J. (2020). Characterization of Structural Properties in High Reynolds Hydraulic Jump Based on CFD and Physical Modeling Approaches. *Journal of Hydraulic Engineering*, *146*(12). https://doi.org/10.1061/(asce)hy.1943-7900.0001820

Martinez, B. (2011). Wind resource in complex terrain with OpenFOAM. *Risø DTU, National Laboratory for Sustainable Energy*, (June).

Menter, F. R. (1994). Two-equation eddy-viscosity turbulence models for engineering applications. *AIAA Journal*, *32*(8). https://doi.org/10.2514/3.12149

Nezu, I. (2005). Open-Channel Flow Turbulence and Its Research Prospect in the 21st Century. *Journal of Hydraulic Engineering*, *131*(4). https://doi.org/10.1061/(asce)0733-9429(2005)131:4(229)

Nikolaidou, L. (2019). *Wall-Modelled Large Eddy Simulation of fully rough non-uniform flow for the purpose of predicting stone stability* (tech. rep.). Delft University of Technology. http://repository.tudelft.nl/.

Nikuradse, J. (1933). Laws of flow in rough pipes [English translation of Stromungsgesetze in rauhen Rohren]. *VDI-Forschungsheft 361. Beilage zu "Forschung auf dem Gebiete des Ingenieurwesens" [Translation from NACA Technical Memorandum 1292]*, *4*(B).

OpenCFD. (2019). OpenFOAM: User Guide v2112. https://www.openfoam.com/documentation/guides/latest/doc/index.html

Rijkswaterstaat. (2020). Uitdagend complex Stuwensemble Nederrijn en Lek gerenoveerd voor de toekomst.

Rijkswaterstaat. (2021). Onderhoud Maas en kanalen in Noord-Brabant en Limburg. https://www.rijkswaterstaat.nl/water/projectenoverzicht/onderhoud-maas-en-kanalen-in-noord-brabant-en-limburg/projecten

Schiereck, G. J. (2017). *Introduction to Bed, Bank and Shore Protection*. CRC Press. https://doi.org/10.1201/9781315274935

Shekari, Y., Javan, M., & Eghbalzadeh, A. (2014). Three-dimensional Numerical Study of Submerged Hydraulic Jumps. *Arabian Journal for Science and Engineering*, *39*(10). https://doi.org/10.1007/s13369-014-1295-0

Steenstra, R. S. (2014). *Incorporation of the effects of accelerating flow in the design of granular bed protections* (tech. rep.). Delft University of Technology. http://repository.tudelft.nl/.

Stevens, T. (2018). *The prediction of stone stability by a three-dimensional eddy resolving simulation technique* (tech. rep.). Delft University of Technology. http://repository.tudelft.nl/.

Team Expertise Maas. (2021). *Hoogwaterbericht H11 Maas Rood - 2021-07-17 2000* (tech. rep.). Watermanagementcentrum Nederland.

Tulapurkara, E. G. (2005). Hundred years of the boundary layer - Some aspects. *Sadhana - Academy Proceedings in Engineering Sciences*, *30*(4). https://doi.org/10.1007/BF02703275

Uijtewaal, W. (2003). *Turbulence in Hydraulics* (tech. rep.). Delft University of Technology. http://repository.tudelft.nl/.

Viti, N., Valero, D., & Gualtieri, C. (2018). Numerical simulation of hydraulic jumps. part 2: Recent results and future outlook. https://doi.org/10.3390/w11010028

von Kármán, T. (1931). Mechanical Similitude and Turbulence. *NACA TM 611*.

Waterloopkunding Laboratorium. (1955). *Stuw Hagestein - Verslag Modelonderzoek* (tech. rep.). Waterloopkunding Laboratorium.

Wilcox, D. C. (1988). Reassessment of the scale-determining equation for advanced turbulence models. *AIAA Journal*, *26*(11), 1299–1310. https://doi.org/10.2514/3.10041

Yakhot, V., Orszag, S. A., Thangam, S., Gatski, T. B., & Speziale, C. G. (1992). Development of turbulence models for shear flows by a double expansion technique. *Physics of Fluids A*, *4*(7). https://doi.org/10.1063/1.858424

Ye, T. (2017). *Stability of block mattress under non-uniform flow downstream of sluice gate* (tech. rep.). Delft University of Technology. http://repository.tudelft.nl/.

Zijlema, M. (2015). *Course CIE4340 Computational Modelling of Flow and Transport* (tech. rep.). Delft University of Technology. http://fluidmechanics.tudelft.nl

A

Major maintenance weirs Meuse

The river system in the Netherlands consists of two main rivers, the Rhine and Meuse, with their origins in Switzerland and France respectively. The Rhine consist mainly of melt water, while the Meuse is a rain river. These rivers provide a navigation route for inland vessels, helping on the transportation of cargo to the hinterland. In order to maintain shipping in these rivers, several weirs and sluices have been created. The Meuse is the most important Dutch river in which these hydraulic structures were build, because of its rain river discharge character with large varying discharges.

From 1925 on seven weirs were made in the Meuse in order to maintain the possibility of the transport by vessels, as the discharge and thus water depth fluctuates throughout the year. The first four of seven weirs were created between 1925 and 1935 at the locations Sambeek, Grave, Borgharen and Lith. An evaluation of these can be found in the report of the Sixteenth International Shipping Congress in Brussels in 1935 (de Vries et al., 1935). The age of these weirs reveals the fact that an inspection has to be done whether these structures need to be replaced or renovated.

In July 2021 an abnormal amount of rain has fallen in the river system of the Meuse, leading to extreme discharge values. The rain increased the discharge to values of 3260 m^3/s (Team Expertise Maas, 2021). In the evaluation of the Sixteenth International Shipping Congress of 1935 it is mentioned that the design discharge for the weirs in the river Meuse was 3200 m^3/s, which is less than the discharge of July 2021 (de Vries et al., 1935).

This mismatch in actual loading and design loading substantiates the replacement task because of the age of the weirs. The combination of mismatch and age is already known to the authorities (Rijkswaterstaat, 2021). In 2028 the replacement or renovation works are scheduled and until then they will receive a large-scale refurbishment.

In order to renovate and recreate these weirs, an assessment on the state of these weirs has to be made. This can be done by either physical or numerical modelling. With these models an assessment of individual parts of the weir can be made, supporting the choice for renovation or replacement. Both methods have their advantages and disadvantages, whereas now often is chosen for physical testing.

Numerical modelling can contribute to further understanding of the system, for determining local forces and because of the possibility of rapidly changing the design geometry. In order to make an assessment in the design phase, it is essential to have a practical model with reduced computation times, still allowing an assessment on the hydraulic structure.

B

Standard gradings

The construction of a bed protection is based on standard gradings. Table B.1 provides an overview of these gradings including their range and nominal stone diameter d_{n50}.

A constructor does not want to sort out every stone diameter as computed for the ideal stability. Thus these gradings determine the construction accuracy. In this way it seems reasonable to work with stone diameters from this curve and define the stability, instead of defining the ideal stability number per location.

In case 2 the standard grading 10-60kg is applied and in the reference case of Jongeling et al. (2003) the stone size compares to 90/180mm. This is based on the fact that the modelled water depth is 20 times smaller than the actual water depth in for example a river.

Table B.1: Standard gradings for quarry rock (Schiereck, 2017)

Class name	Range	d_{n50} (m)
CP45/125	45/125 mm	0.064
CP63/180	63/180 mm	0.09
CP90/250	90/250 mm	0.128
CP45/180	45/200 mm	0.064
CP90/190	90/180 mm	0.097
LMA 5-40	5-40 kg	0.17
LMA 10-60	10-60 kg	0.23
LMA40-200	40-200 kg	0.34
LMA 60-300	60-300 kg	0.38
LMA 15-300	15-200 kg	0.31
HMA 300-1000	300-1000 kg	0.59
HMA 1000-3000	1-3 ton	0.90
HMA 3000-6000	3-6 ton	1.18
HMA 6000-10000	6-10 ton	1.44

C

OpenFOAM

The model created for this thesis is built in OpenFOAM (OpenCFD, 2019). The full name is Open Source Field Operation and Manipulation. As in the name, this CFD software package is open source, making it very interesting. If OpenFOAM proves to work as well as licensed CFD software as ANSYS, it could mean a serious reduction in modelling costs. The used versions are 17.06 and Foam-Extend 3.1. The calculation are performed on a single computer of approximately €5000, containing 10 cores.

OpenFOAM works with a folder structure and runs on Linux. A basic version of this folder structure is explained, as well as essential parts for the creation of the model. The smooth model, which is used for validation, can be found in Chapter 3.

In order to start an OpenFOAM computation, several steps have to be done. First the model mesh has to be created, next the mesh has to be divided into different parts, allowing simultaneous calculations on multiple computer cores. At last the model should be reconstructed.

Folder structure
As mentioned, OpenFOAM works with a folder structure. Within the case folder, where everything is stored, three main directories are present. These are the *0*, *constant* and *system* directory.

The *0* directory contains the initial and boundary conditions for each variable that is modelled. For this thesis, these are *k*, *nut*, *omega*, *p* and *u*. Within the file for these variables, for each boundary the boundary condition is given based on the type of patch. Examples are fixedValue, zeroGradient, slip and omegaWallFunction.

In the *constant* directory the information regarding the mesh, model constants and turbulence model is saved. For the mesh, information as points, faces and neighbours is saved. Model constants and turbulence model for a RANS model are saved in *Rasproperties* and *transportproperties*.

The *system* directory controls the simulation, including files on the solution procedure, additional meshing procedures, time step definitions and parallel computations. Essential files are *controlDict*, *fvSchemes* and *fvSolutions*. Specific info regarding this can be found at the OpenFOAM user guide (OpenCFD, 2019).

Applied OpenFOAM commands
In this subsection the applied commands for the model runs are summarised. The commands are provided in chronological order and contain a short explanation to understand what the command does.

- *blockMesh* - Through blockMesh the basis geometry and mesh is created. In the *blockMeshDict* file all the necessary info is provided to run this command.
- *faceSetToSTL* - This command makes it possible to create various shapes, which can later on be cut out of your blockMesh. This command converts input from a *stlDefinitions* file in the *constant* directory towards stl-files.

- *snappyHexMesh (SHM)* - Through SHM it is possible to make local refinements, cut out STL surfaces and refine around these STL surfaces. It reduces the work needed in setting up blockMesh.
- *extrudeMesh* - extrudeMesh prepares your grid for a 2D simulation by redefining the SHM surfaces towards workable 2D surfaces.
- *checkMesh* - as the name says, this command checks your mesh on skewness and other mesh parameters. This command allows the user to see whether the mesh is well defined.
- *decomposePar* - decomposes the mesh into multiple pieces, allowing parallel running on different processors.
- *mpirun* - run command for the decomposed mesh. After this command, the simulation is actually calculating and not preparing the calculation anymore.
- *reconstructPar* - reconstructs the decomposed files into one file in the main directory, making it possible to have a look at the results.

pimpleFoam solver
For this thesis the pimpleFoam solver is used, just as Steenstra (2014) did for his research. This algorithm is based on the PIMPLE method, which combines the SIMPLE (Semi-Implicit Method for Pressure-Linked Equations) and PISO (Pressure Implicit with Splitting of Operator) algorithms.

The SIMPLE algorithm solve steady-state problems, while the PISO algorithm is suitable for transient simulations. Steady-state simulation computes the fully developed solution that does not change in time. Transient simulations compute the instantaneous values in each time step for each quantity.

The stability of the PIMPLE algorithm is better compared to PISO, especially when the nature of the solution is inherently unstable. Garcia-Alcaide et al. (2017) made a simplified overview of how the PIMPLE algorithm works (Figure C.1). As this thesis is not about in depth information on algorithms, this information is considered sufficient.

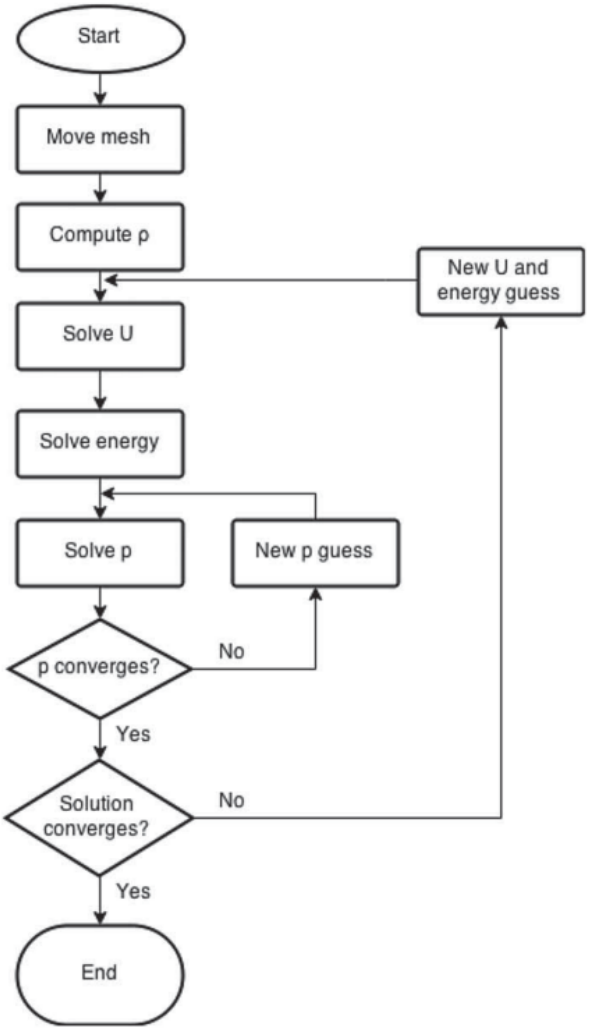

Figure C.1: PIMPLE algorithm flowchart (Garcia-Alcaide et al., 2017)

D

Test results Jongeling et al. (2003)

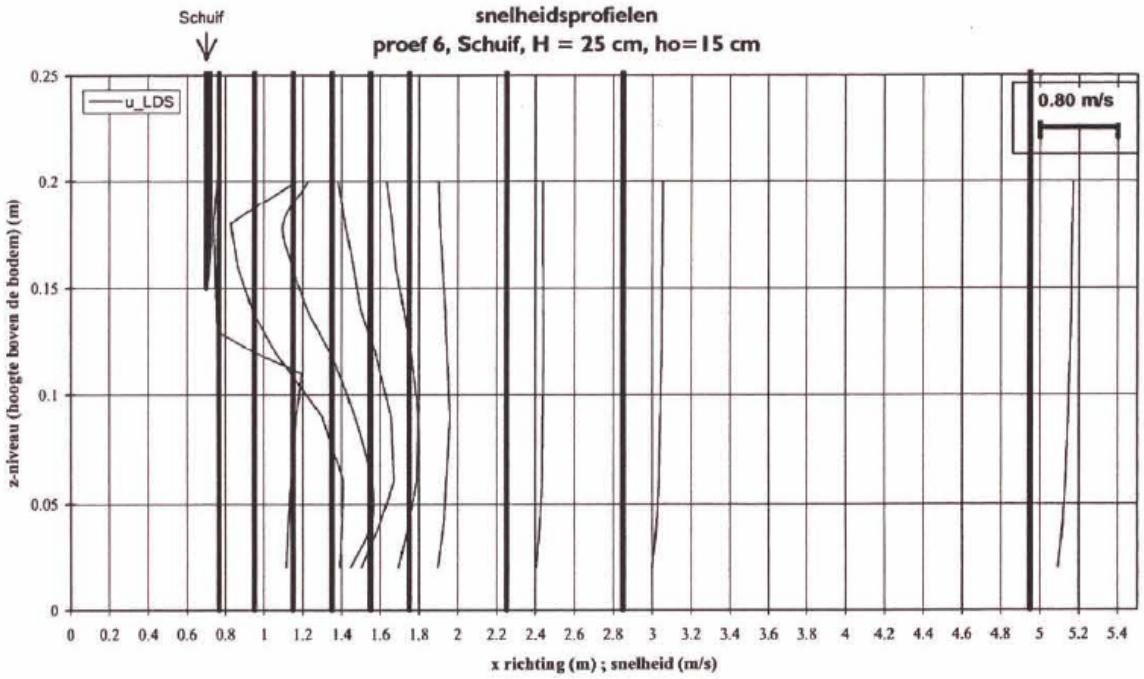

Figure D.1: Velocity profile of test 6 of Jongeling et al. (2003)

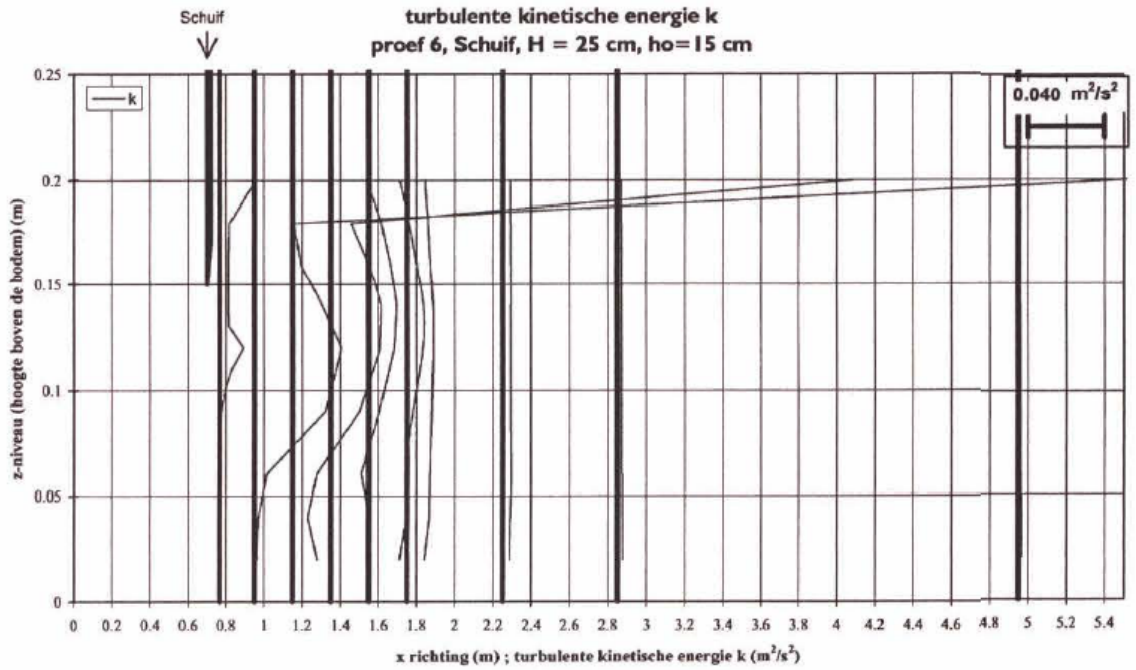

Figure D.2: Turbulent kinetic energy profile of test 6 of Jongeling et al. (2003)

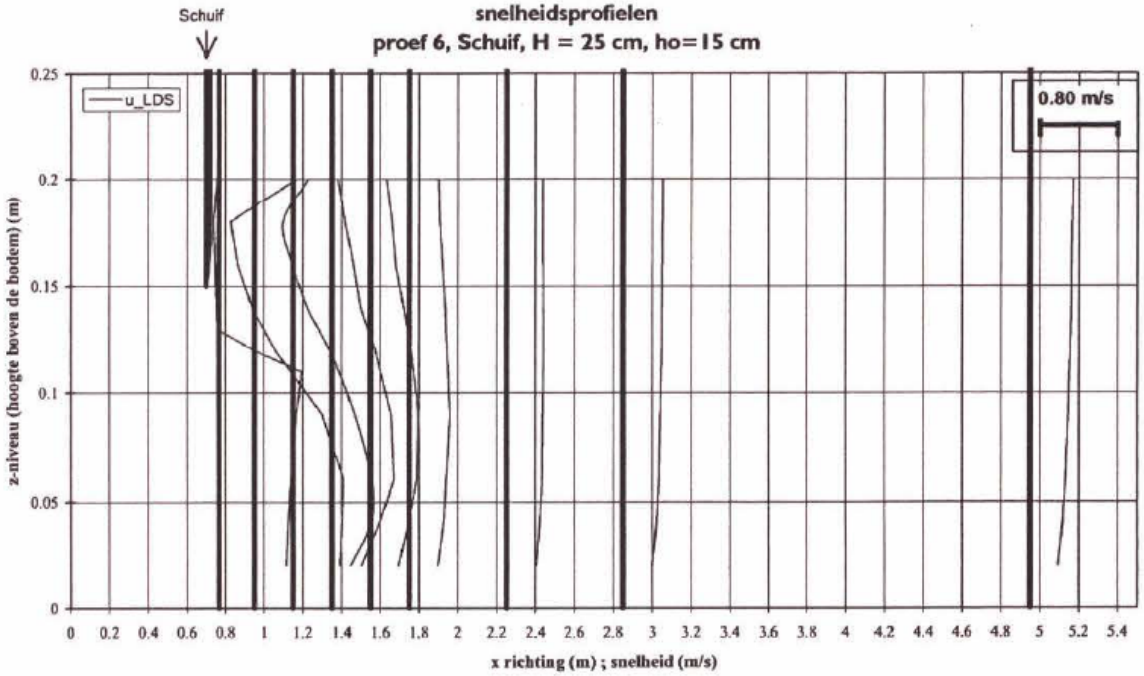

Figure D.3: Velocity profile of test 6 of Jongeling et al. (2003)

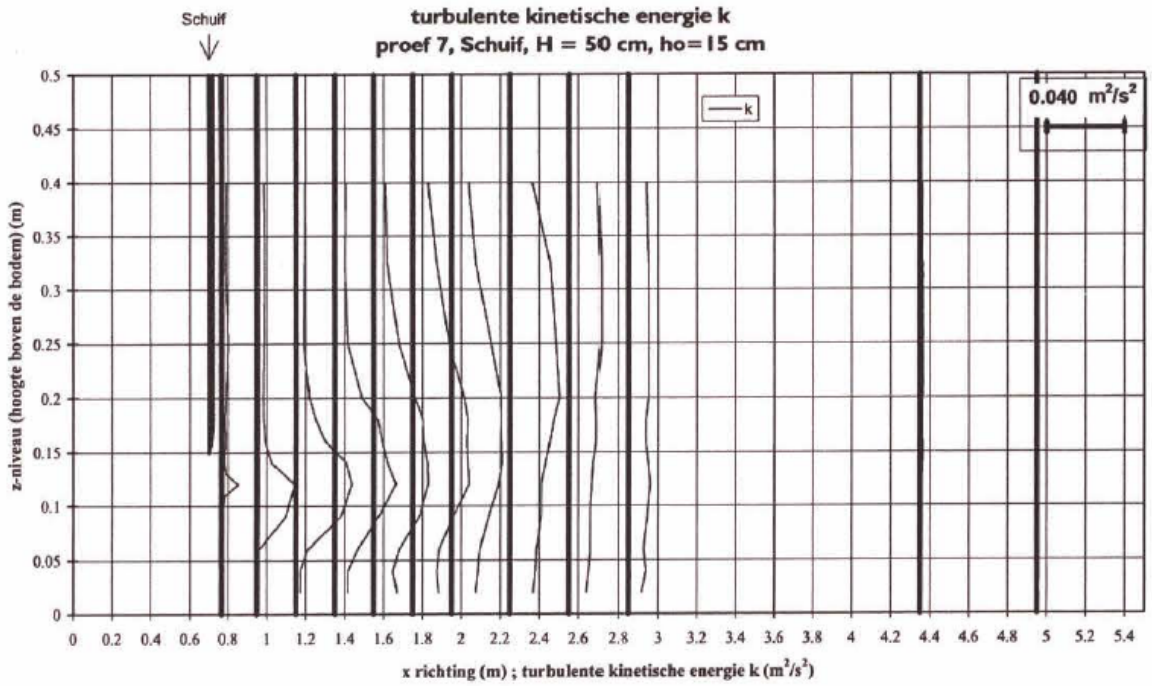

Figure D.4: Turbulent kinetic energy profile of test 7 of Jongeling et al. (2003)

E

Advice on numerical choices

In this appendix an advice is given on the design of numerical models for other flow situations. This can help a future researcher to speed up in the knowledge on CFD modelling.

Flow situation	Advice
Underflow weir with submerged hydraulic jump	The underflow weir with submerged hydraulic jump is investigated in this research. As mentioned, the $k-\omega$ SST turbulence closure model for the RANS approach fits the best for separating flows, which are present at an underflow gate (El-Behery and Hamed, 2011). A 2D model approaches the flow phenomena well, while a 3D method would improve this. For an even further improved method, two-phases should be modelled instead of the one-phase approach used in this research. All these additional steps have influence on the final computation time, thus it should be considered what is preferred to implement and what is not.
Underflow weir with non-submerged/classic hydraulic jump	Viti et al. (2018) provides a table where RANS models and three types of turbulence models, being the $k-\omega$ SST, $k-\epsilon$ and RNG $k-\epsilon$, are compared to three types of classic hydraulic jump. They showed that the RNG $k-\epsilon$ model shows the best agreement for modelling a non-submerged hydraulic jump. High-fidelity models as DES and LES can properly reproduce turbulence quantities, but those methods are very numerically expensive. A consideration must be made in advance of the modelling on what the application of the model will be. For 3D flows, Shekari et al. (2014) states that the RSM approach shows good agreement. This approach is more computationally demanding than the two-equation closure models.
Overflow weir	The overflow weir cannot be modelled with a rigid lid approach. This means that a two-phase OpenFOAM solver should be used, such as InterFOAM. Andersson et al. (2013) provides a research in which the VoF (and rigid-lid approach) is tested. In this research it is found that the RSM, RNG $k-\epsilon$, Realizable $k-\epsilon$ and $k-\omega$ SST turbulence closure models have a better agreement with experimental data than using the standard $k-\epsilon$ and $k-\omega$ models. For plunge pools, downstream of the overflow weir, Castillo Luis et al. (2017) recommends to apply the $k-\omega$ SST model as well.

Flow situation	Advice
Wall roughness	Two modelling options can be chosen for implementing roughness into a model, as described in Chapter 2. The first one is low Reynolds modelling, which means that every individual stone has to be modelled and the flow has to be solved with a very small grid size near the stones. The other option is the application of a wall function, as applied through the *nutkRoughWallFunction* in this research. It is advised to apply the wall function approach as it reduces the computation time, compared to the low-Reynolds modelling. This is certainly the best option when modelling large flow situations, like a real size weir. Another wall function option in OpenFOAM is the *nutURoughWallFunction*.